Chapter One

Introduction

1.1 Geographic location

1.1.1 Description of the project area

The project area is located in the Bulilimangwe district of Matebeleland South on a grid roughly 3 km by 2 km with the Kupa river flowing in the central part in a roughly S–N direction. The study area is about 79 km north west of Plumtree and about 120 km west of Bulawayo (see Fig. 1.1). This is a sparsely populated rural area under Chief Madhlambudzi with the main economic activity being subsistence farming and livestock rearing. Cattle, goats, some sheep and donkeys are the main animals kept. The area is in a hot, dry region with Plumtree having an annual rainfall of just 545 mm and a mean temperature in the hottest month of 24° C (Sayce, 1987).

The main crops grown are sorghum, maize, pumpkins (*amadjodo/mashamba*) and watermelons in large enclosed gardens (Fig. 1.3). Water supplies are obtained from boreholes, deep wells (although some have salty water) and aquifers beneath dry river beds. The major dam in the area is located at Madhlambudzi business centre about 5 km south west of the exploration camp and supplies tapped water to the secondary school, clinic and police camp.

The topography is generally flat with a gentle slope north towards the Tegwani river (Fig. 1.2) which is fed by numerous streams that dry up after the wet season. Medium to dense mopane forest covers the area with thick wood on clay soils near streams and more open thorn bush on sandy soils (Fig. 1.4). Regionally, granite kopjes are common in areas to the east, west and south of the project area.

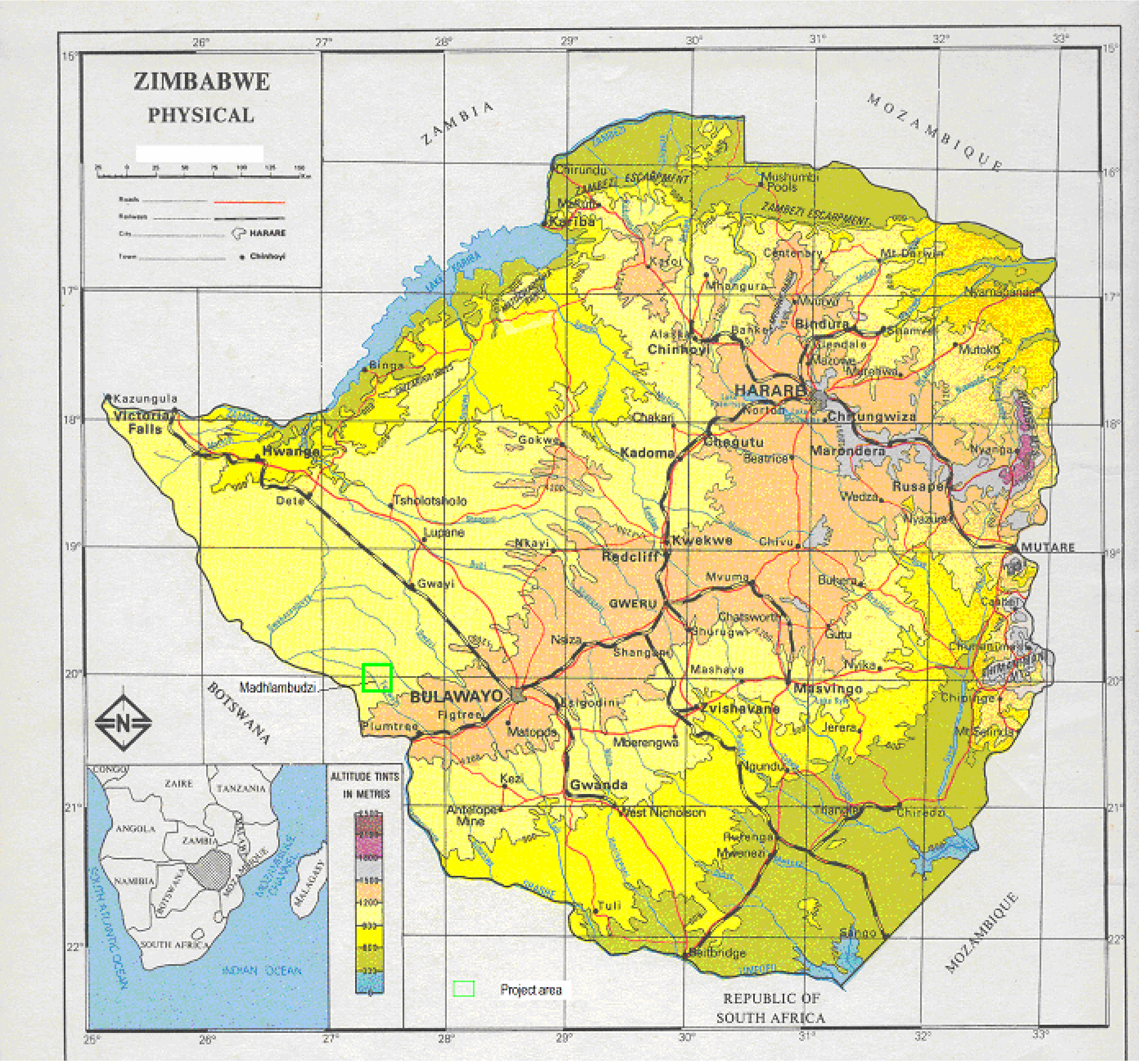

Fig. 1.1 Location map of Bulawayo, Plumtree and Madhlambudzi (within green box).

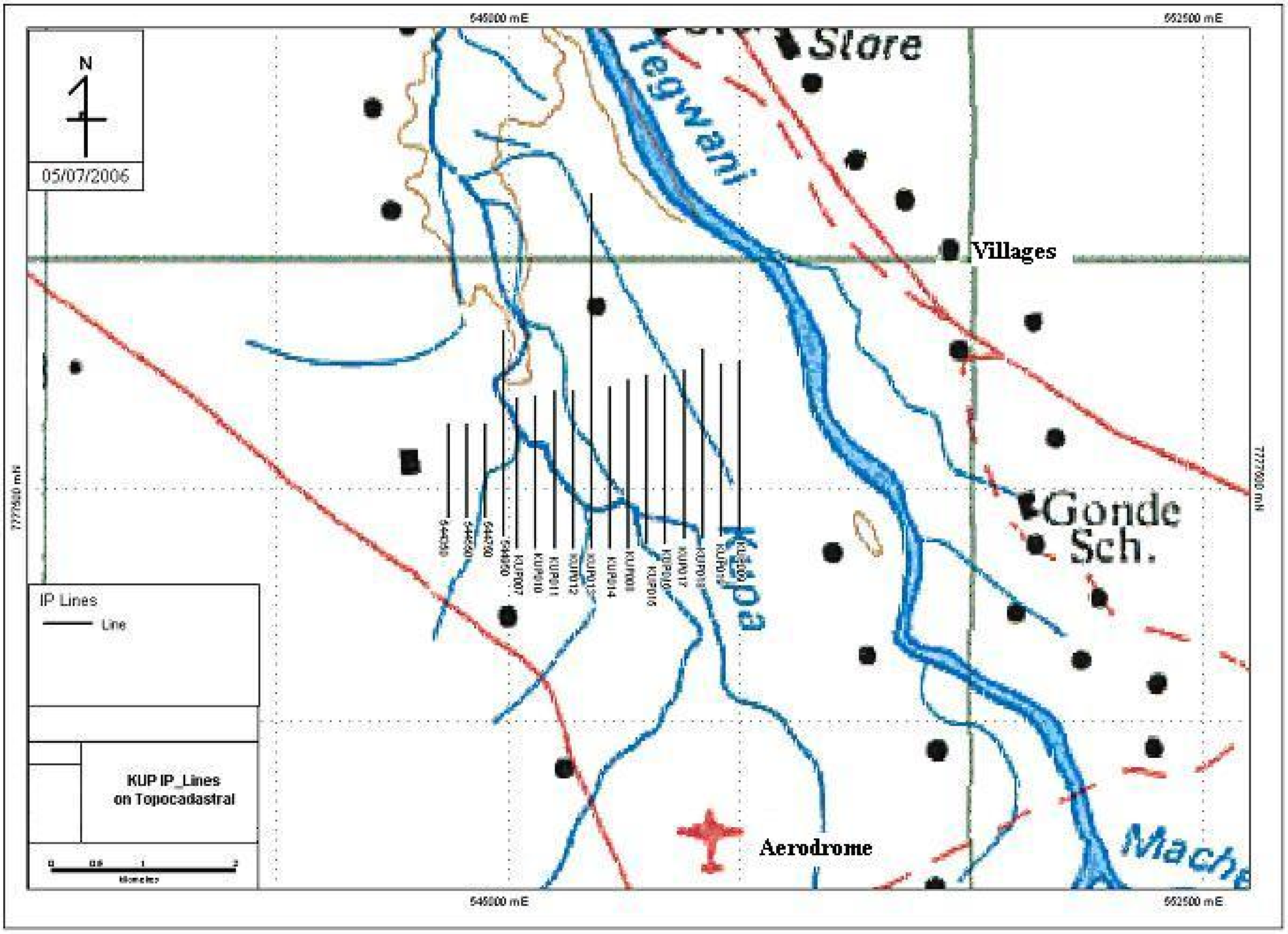

Fig. 1.2 Map of the Kupa project area showing the exploration grid.

Fig. 1.3 A typical garden with its thorny hedge. It is commonly larger than a hectare.

Fig. 1.4 A footpath exposing the Kalahari cover in a mopane forest.

1.1.2 Current exploration

The Kupa grid is located in the exclusive prospecting order (E.P.O.) 1503, (Fig. 1.5) measuring 64 660 ha and whose tenure is held by Canister Resources. Canister, operating as Rockover Resources, is a mineral exploration company prospecting for gold, base metals and diamonds in the Tsholotsho, Nyamandhlovu and Plumtree areas.

The grid was designed by Canister to cover an area with aeromagnetic and geochemical anomalies (Figures 1.17 - 1.25). It was positioned on the ground using a Garmin Geko 201 GPS (Global Positioning Satellite receiver) by Canister's fieldcrew. The pegs were sited to within a 5 - 8 m accuracy and lines approximately 2 m wide were cut through the vegetation using axes and machetes (see Fig. 1.6). A total of 17 lines were established on the grid, with 13 lines cut before the author joined the fieldcrew (see also Appendix A1.2).

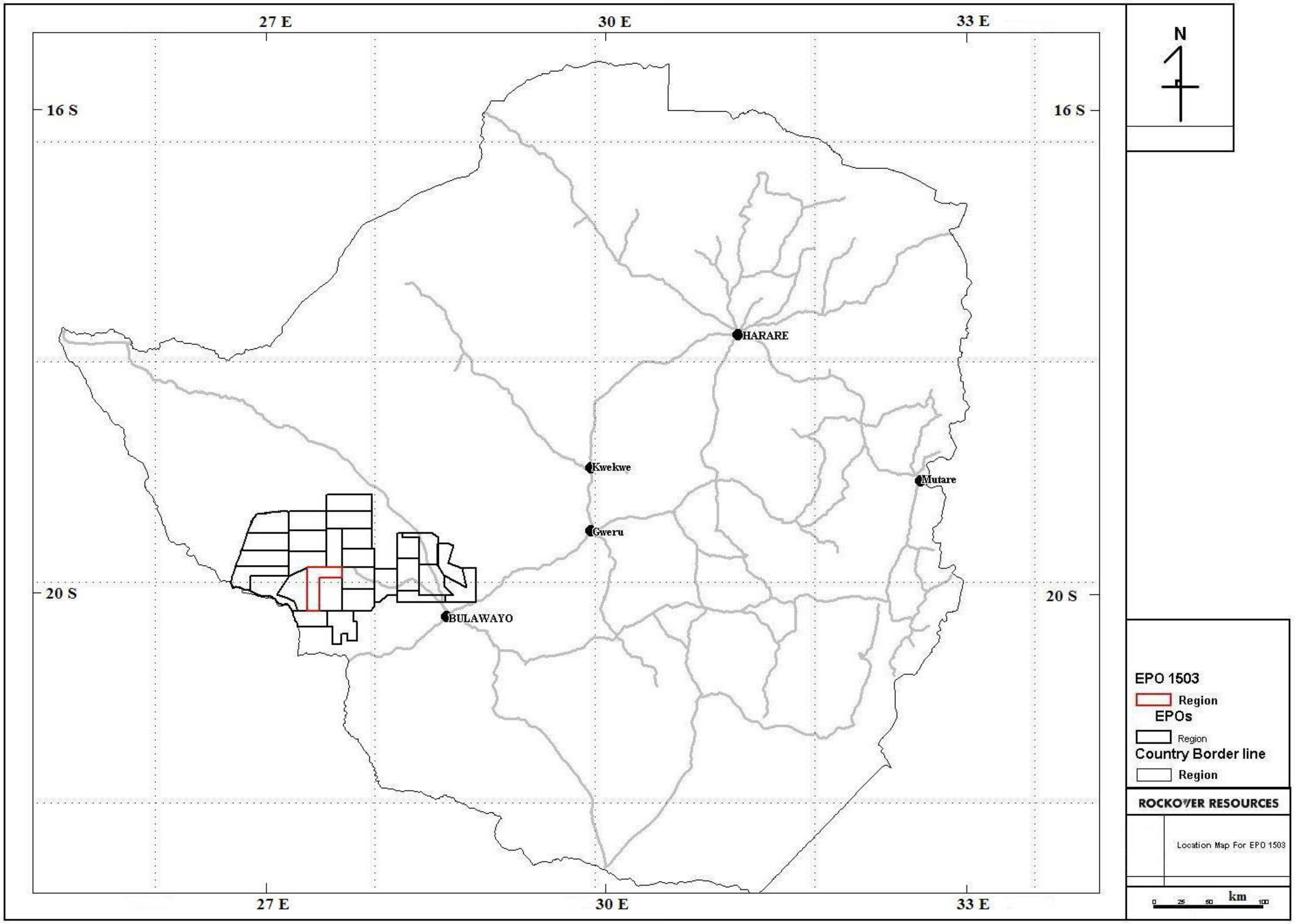

Fig. 1.5 Location map of E.P.O. 1503 (highlighted in red).

Fig. 1.6 A survey line cut through vegetation.

1.2 Geology

1.2.1 Regional geology

The region in and around E.P.O. 1503 is under sand cover and there is no published detailed geological mapping to date. Fig. 1.7 shows the regional geology of parts of south western Zimbabwe. The study area lies between two exposed greenstone belts to the east and west namely, the Maitengwe Greenstone Belt in eastern Botswana and the Bulawayo Greenstone Belt respectively. It can be inferred that an extension of one of the limbs of these greenstone belts may lie beneath the exploration grid and reference is made to studies done by Litherland (1975) around the Maitengwe area and by Amm (1940) for the country around Bulawayo.

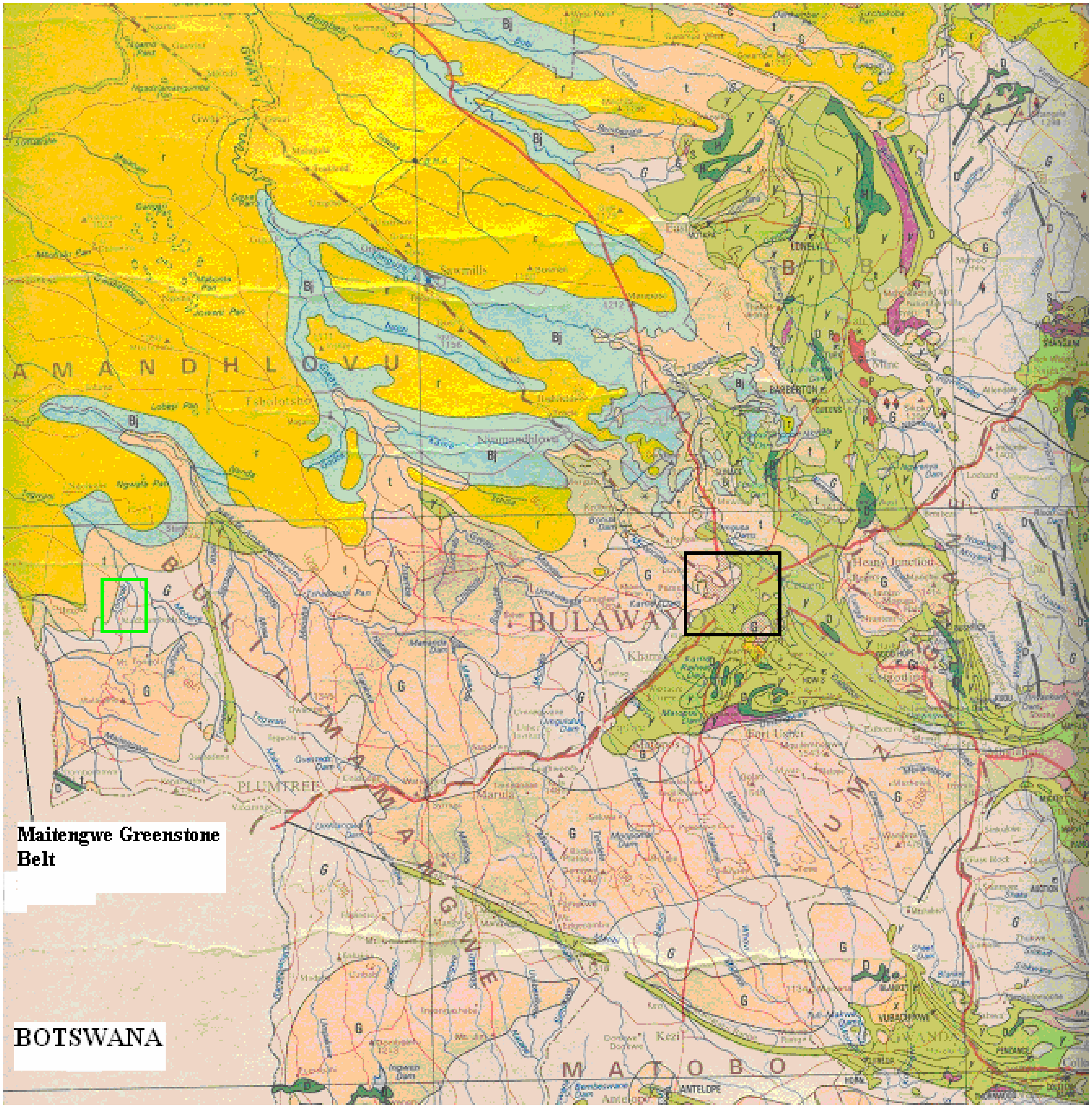

Fig. 1.7 The regional geology of some districts of south western Zimbabwe showing the area around Madhlambudzi, the Bulawayo Greenstone Belt and the location of the Maitengwe Greenstone Belt in Botswana (from 1:1000 000 geological map of Zimbabwe, seventh edition, Zimbabwe Geological Survey, 1999). The study area is within the green box and the area of Fig. 1.9 is in the black box.

1.2.1.1 Maitengwe Greenstone Belt

Litherland (1975) describes a typical greenstone belt of Archaean metasedimentary and metavolcanic rocks (schist relics) intruded by younger granitoids. The rocks in the area are initially subdivided as:

Age	Geological Units
Cenozoic	Kalahari Beds
---------------------------------- unconformity -------------------------	
Archaean	Basement Complex

Within the Basement Complex, two large schist relics are mapped known locally as the Maitengwe and Vumba Volcanic Groups. The ages of the Archaean rocks are c. 3 500 – 2 500 Ma and are underlain by the western portion of the Zimbabwe Craton which has been stable since c. 2 600 Ma. The unconformity represents a time gap of ~2 500 Ma (Litherland, 1975).

Structurally and perhaps stratigraphically in between these volcanic groups lies the Tutume Meta-arkose Group. This is a layered granitoid unit in which belts of amphibolite, granitic gneiss and meta-arkose are interstratified. These layers are concordant with those of the schist relics (Fig. 1.8).

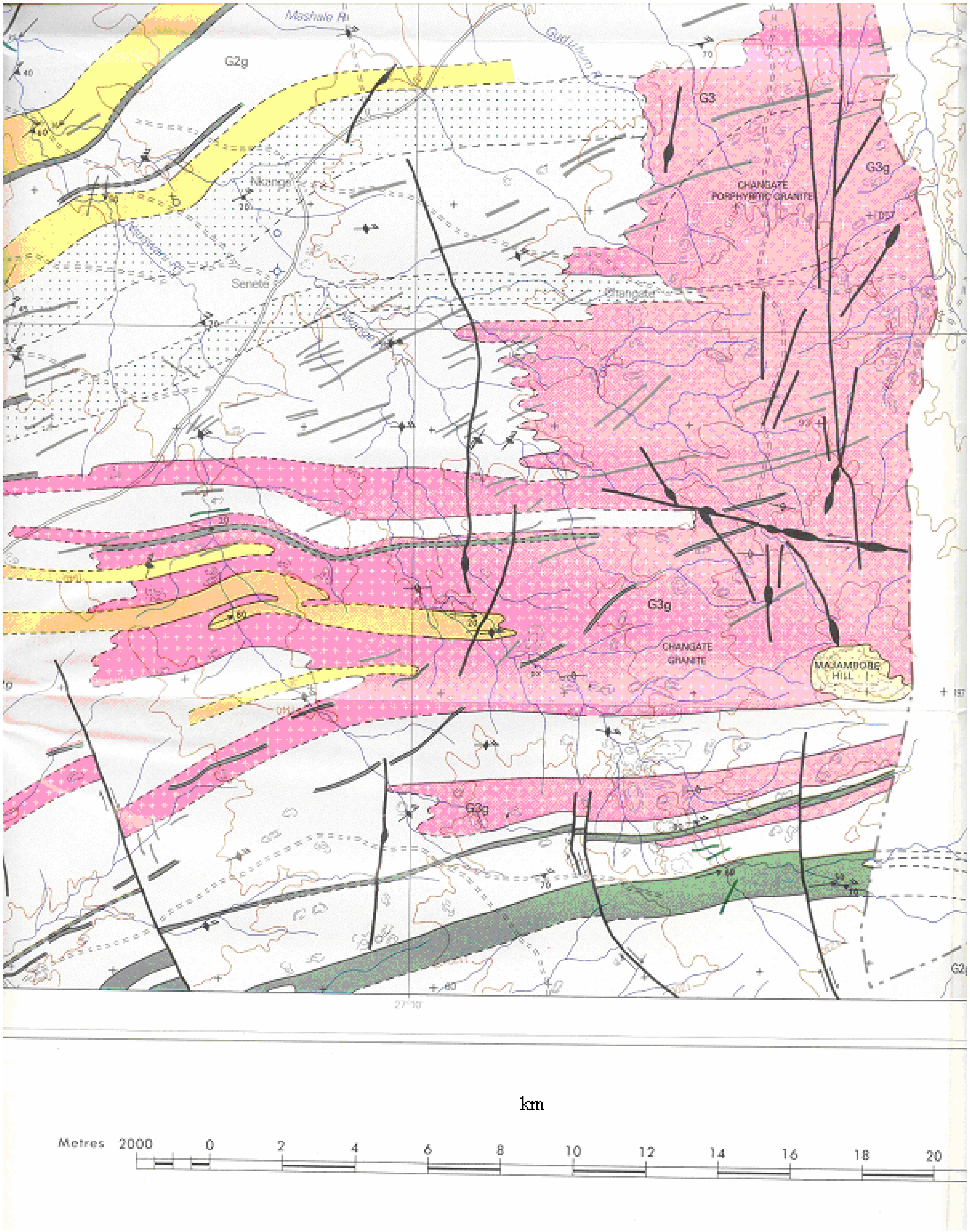

Fig. 1.8 A portion of the Maitengwe Greenstone Belt, Botswana (after Litherland, 1975).

Episodes of deformation have been recognised in chronological order, abbreviated as F_1, F_2 etc. Interspersed between these regional events are granitic phases also in chronological order, two of which (G_1 and G_4) are essentially plutonic and the remainder, (G_2 and G_3) are migmatitic or anatectic. The granitic and deformational events are generally accompanied by a metamorphic phase. Post-Archaean events are confined to the major phase of faulting of the area which is essentially synchronous with the intrusion of late/post-Karoo dyke swarms and, latterly, the deposition of the Kalahari Beds.

A layered, heterogeneous assemblage of metasedimentary and metavolcanic rocks characterises the Maitengwe and Vumba Schist Relics. The metamorphic rocks fall into 3 categories: ultramafic, mafic and felsic. Metasediments are subordinate to metavolcanic rocks and include banded ironstones, marbles, calc-silicates and various aluminous schists and quartzites. They provide extremely useful marker horizons as well as metamorphic indicators. Table 1.1 gives the subdivisions of the Maitengwe and Vumba Schist Relics.

Table 1.1 Maitengwe and Vumba Schist Relic Formations (Litherland, 1975).

Subdivision	Formation	Rock Types
Top	Maitengwe Ultramafic Formation	Serpentinite, ultramafic schist, amphibolite with minor banded ironstones, marble and calc-silicate.
Bottom	Maitengwe Banded Ironstone Formation	Banded ironstone with minor serpentinites, ultramafic schist and marble.

The Vumba Schist Relic which is a remnant of the Vumba Volcanic Group is sub-divided as follows:

Subdivision	Formation	Rock Types
Top	Upper Vumba Mafic Formation	Amphibolite
	Upper Vumba Felsic Formation	Felsic metavolcanics with amphibolite passing laterally into aluminous schists. Calc-silicate at base
	Lower Vumba Mafic Formation	Amphibolites with felsic metavolcanic lenses and pyroclastics.
	Lower Vumba Felsic Formation	Felsic metavolcanic rocks passing laterally into aluminous schists and tuffs. Minor amphibolite, quartzite, marble and calc-silicate.
	Vumba Mixed Volcanic Formation	Amphibolite with serpentinite and metapyroxenite sills. Lenses of felsic metavolcanics and kopje pyroclastics. Occasional meta-arkose horizons at base.
Bottom	Sebina Ultramafic Formation	Ultramafic schist and amphibolite. Minor meta-arkose.

The granite rocks which make up the greater portion of the region are classified according to their field relationships and chemical composition. This resulted in the recognition of successive stages of granitic events (the granite series $G_1 - G_4$).

Harpum's (1963) classification (Litherland, 1975) was used to distinguish the granitoids chemically as follows:

	K_2O / Na_2O
Granite	> 1,5
Adamellite	1,0 – 1,5
Granodiorite	0,6 – 1,0
Tonalite	< 0,6

Intruding these Archaean rocks are a host of minor basic and acid dykes which were emplaced at different episodes ($B_1 - B_4, A_1 - A_7$). The basic dykes are typically dolerites and some pyroxenites with the acid veins consisting of pegmatites, granophyres, granites, quartzo-feldspathic, mygmatites and sulphide-bearing quartz veins.

The Post-Archaean deposits are the Kalahari Beds which consist of sandstones, silcretes (bedded and fault) and sands.

1.2.1.2 Bulawayo Greenstone Belt

The oldest rocks in the area (Fig. 1.9) are the Basement Schists which have been subdivided into the Lower and Upper Greenstones (Table 1.2).

The volcanic rocks of the Lower Greenstones consist of:

- tremolite-actinolite-talc-schists;
- basalts–epidiorites of different grain size; and
- andesites interbedded with agglomerates and tuff .

These metavolcanics exhibit the following different forms and textures depending on the amount of metamorphism and proximity to the younger acid intrusives (granites):

- pillow lavas;
- amygdaloidal lavas;
- massive epidiorites;
- hornblende-schists representing sheared basalts; and
- coarse-grained and porphyritic basalts near granite contacts or above shallow plutons representing recrystallization.

The Lower Greenstones are indistinguishable from the Upper Greenstones petrographically. Field relationships show that the older greenstones had an enormous thickness of lavas and shorter periods of quiescence where thin interbedded sediments accumulated. The younger andesites are interbedded with agglomerates and tuffs. Thin beds of banded ironstones, sheared grit/greywacke and inconsistent limestones. Dacites have also been reported.

The general metamorphism is low-medium grade with indicator minerals such as chlorites and hornblendes.
The metamorphic minerals series is:

- lowest grade:- oligoclase, andesine, chlorite and abundant carbonates;
- with increasing grade:- carbonates replaced by zoisite and epidotes;
- highest grade:- hornblende replaces chlorite and soda-lime feldspars form albite and epidote; sericite developed in highly sheared rocks.

The Upper Greenstones are characterised by more frequent lava flows i.e. thicker units and more frequent alternating bands of intermediate and basic lavas. Periods of quiescence seemed to have been longer resulting in more developed bands of ironstones.

The overlying Sedimentary Series is made up of the Conglomerate Group and the Phyllite Group. These groups represent the different depositional environments of a deep basin from high energy, deeply laid conglomerates to the shallow water bodies that accumulated ironstones and limestones. The phyllites were formed from the metamorphism of the argillaceous sediments.

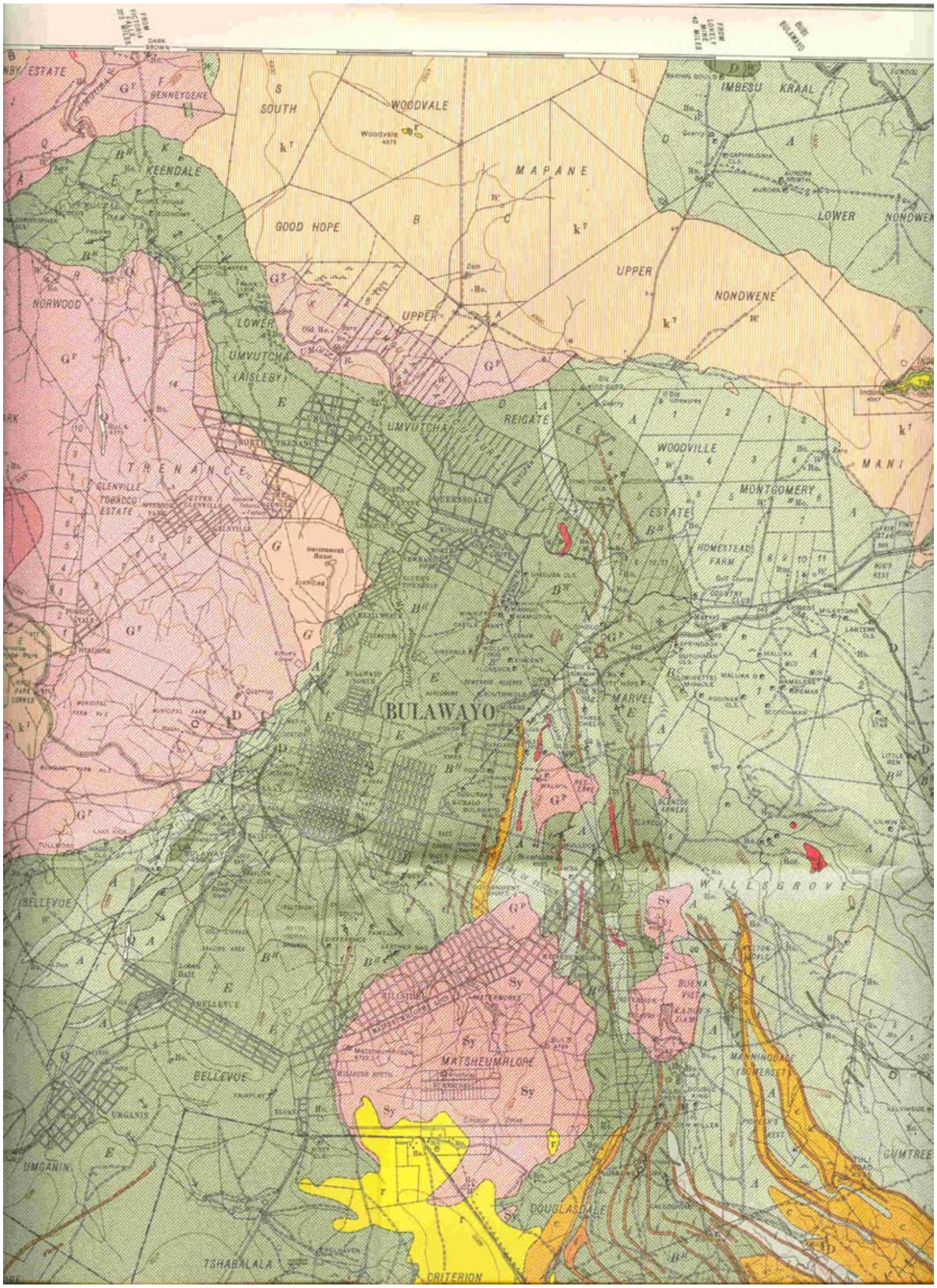

Fig. 1.9 The geology of the area around Bulawayo (Amm, 1940).

Table 1.2 Formations of the Bulawayo Greenstone Belt (Amm, 1940).

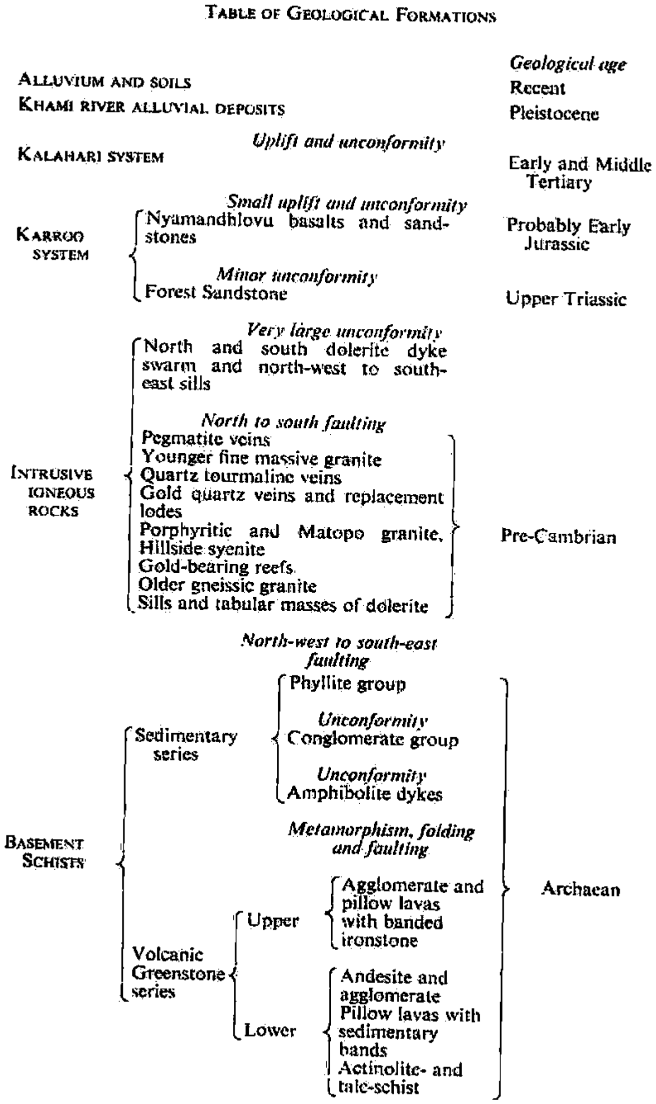

TABLE OF GEOLOGICAL FORMATIONS

				Geological age
ALLUVIUM AND SOILS				Recent
KHAMI RIVER ALLUVIAL DEPOSITS				Pleistocene
			Uplift and unconformity	
KALAHARI SYSTEM				Early and Middle Tertiary
			Small uplift and unconformity	
KARROO SYSTEM			Nyamandhlovu basalts and sandstones	Probably Early Jurassic
			Minor unconformity	
			Forest Sandstone	Upper Triassic
			Very large unconformity	
INTRUSIVE IGNEOUS ROCKS			North and south dolerite dyke swarm and north-west to south-east sills	Pre-Cambrian
			North to south faulting	
			Pegmatite veins Younger fine massive granite Quartz tourmaline veins Gold quartz veins and replacement lodes Porphyritic and Matopo granite, Hillside syenite Gold-bearing reefs Older gneissic granite Sills and tabular masses of dolerite	
			North-west to south-east faulting	
BASEMENT SCHISTS	Sedimentary series		Phyllite group	Archaean
			Unconformity	
			Conglomerate group	
			Unconformity	
			Amphibolite dykes	
			Metamorphism, folding and faulting	
	Volcanic Greenstone series	Upper	Agglomerate and pillow lavas with banded ironstone	
		Lower	Andesite and agglomerate Pillow lavas with sedimentary bands Actinolite- and talc-schist	

The granites are typical of the granite-greenstone terraines as briefly described above (section 1.2.1.1). They are medium- to coarse-grained soda-rich intrusives with an average composition of granodiorite. Amm (1940) classifies them by mainly textural and structural features. Associated with the granites are the felsite and quartz porphyry later intrusives. The emplacement of the dolerite dyke swarms followed a period of regional faulting.

The Karoo Supergroup contains the Forest Sandstone group, in which beds of reptilian fossils have been found, and the Nyamandlovu group of alternating sandstone and basalt units stratigraphically similar to the Karoo of South Africa (Table 1.3).

Table 1.3 The Karoo Supergroup (Amm, 1940).

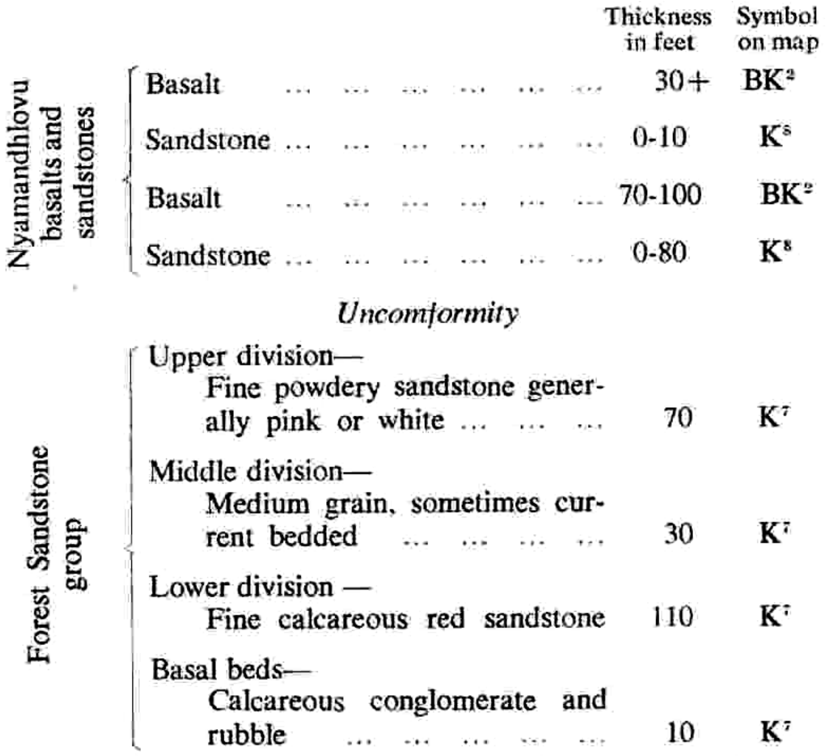

		Thickness in feet	Symbol on map
Nyamandhlovu basalts and sandstones	Basalt	30+	BK^2
	Sandstone	0-10	K^8
	Basalt	70-100	BK^2
	Sandstone	0-80	K^8
	Uncomformity		
Forest Sandstone group	Upper division— Fine powdery sandstone generally pink or white	70	K^7
	Middle division— Medium grain, sometimes current bedded	30	K^7
	Lower division — Fine calcareous red sandstone	110	K^7
	Basal beds— Calcareous conglomerate and rubble	10	K^7

Remnants of the Kalahari Beds with its base of concretionary ironstone and unconsolidated sands are preserved on the high ground to the NW of the main watershed.

The most recent cover is the alluvium unit of thin deposits of muds, clays and fine sandy loams. Overlying these muds is a discontinuous layer of red sands derived from the Karoo and small ferruginous pebbles presumably from the Kalahari ironstone. Sometimes calcareous tufa is developed varying in form from a few nodules to continuous layers. The most common variety of tufa being travertine in the courses of perennial streams overlying carbonated andesite greenstones.

1.2.2 Local geology

Owing to the Kalahari sand cover, no local geology mapping had been done before this study. During the course of the surveys, the author noted rock outcrops and soil changes which were used to make a preliminary geological map (see Fig. 1.16).

1.2.2.1 Outcrops

Most of the rock exposures were seen along the major river courses with a few outcrops in the bush. Figures 1.10 to 1.15 depict some of the discoveries made.

Fig. 1.10 Metabasaltic rocks in the Chamata river striking roughly E-W. Located at UTM 0545451E, 7777681N and 1100 m above sea-level.

Fig. 1.11 Sheared porphyritic granites in a streambed. Location 0546966E, 7776273N and at elevation 1113 m.

Figure 1.12 Steeply dipping quartzo-feldspathic gneisses in a shear zone striking E-W. Location 0547043E, 7776521N and elevation 1110 m.

Fig. 1.13 Mylonitic gneiss in a streambed striking E-W. location 0546922E, 7776505N and elevation 1108 m.

Fig. 1.14 Massive quartz vein on the bank of the Chamata river. Location 0545293E, 7777859N and elevation 1109 m.

Fig. 1.15 Sandstone exhibiting iron oxidation and manganese coating(?) in a small excavation in the bush. Location 0545544E, 7776628N and at elevation 1109 m.

1.2.2.2 Mapping

The location of the rock outcrops within the survey area were recorded with a Garmin GPS to an accuracy of up to 5 m and these were used to map the lithologies. However, no contacts were physically seen so the boundaries are inferred. Fig. 1.16 shows the local geology and soils and Appendix A1.1 illustrates the hand specimens brought from the field and their descriptions.

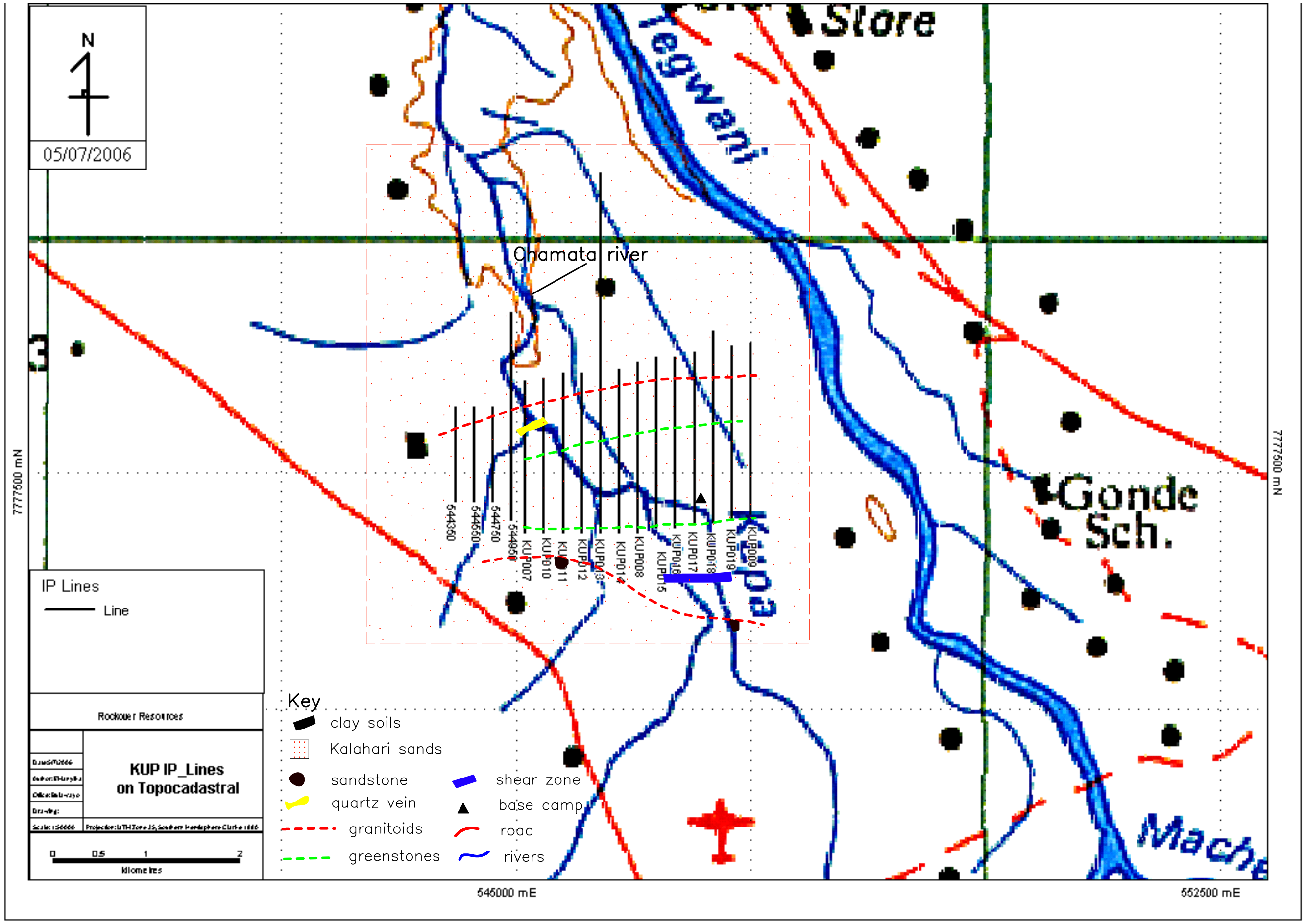

Fig. 1.16 Local geology of the Kupa grid showing outcrop locations, soils and inferred lithological contacts beneath the Kalahari cover (mapped by S. Gumbie, 2006).

1.3 Previous Work

1.3.1 Geochemistry

The initial exploration targets were generated from results of regional hydrogeochemical sampling of boreholes in the area held by Canister's E.P.O.s. The borehole waters were analysed for 17 different elements which included zinc, cadmium, cobalt, nickel and gold. Several localities were identified for further exploration eg. Dokwe, Juju, Bubude, Shiloh and Kupa.

Follow-up regional soil sampling on an initial 1 km x 2 km grid was done and was progressively narrowed down to a 200 m x 50 m grid over anomalous zones (Marova, pers. comm., 2006). Geochemistry maps (Figs. 1.17 – 1.22) were supplied to the author in digital form by Canister to illustrate the trend of the geochemical anomalies with the blue ("cold") colour representing lows and the red and purple ("hot") colours representing high element concentrations in parts per million (ppm). Although the maps came without colour scale bars and coordinates, they are still useful in illustrating trends. A dominant NE-SW trend can be seen on these maps.

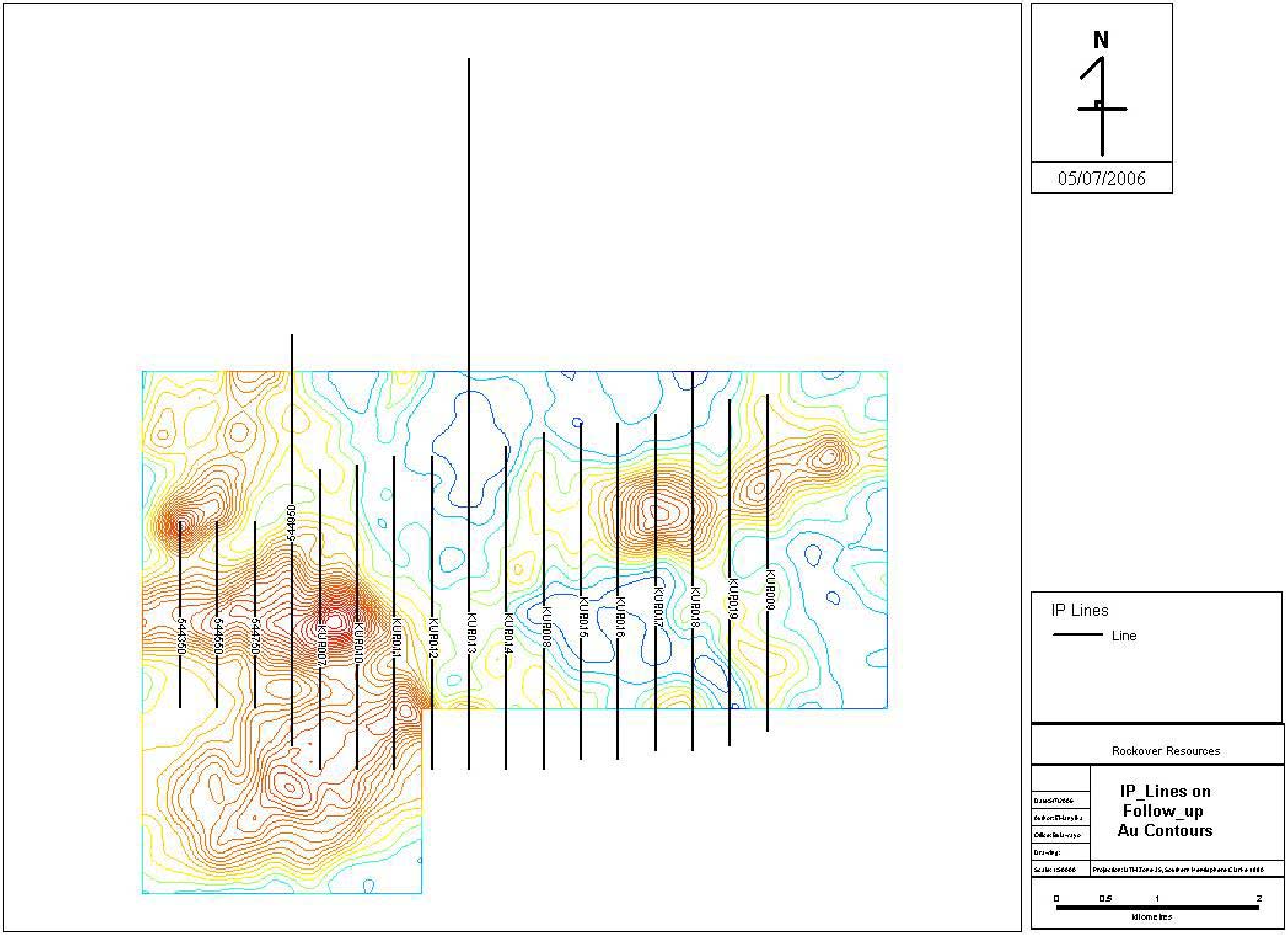

Fig. 1.17 Gold concentration contour map.

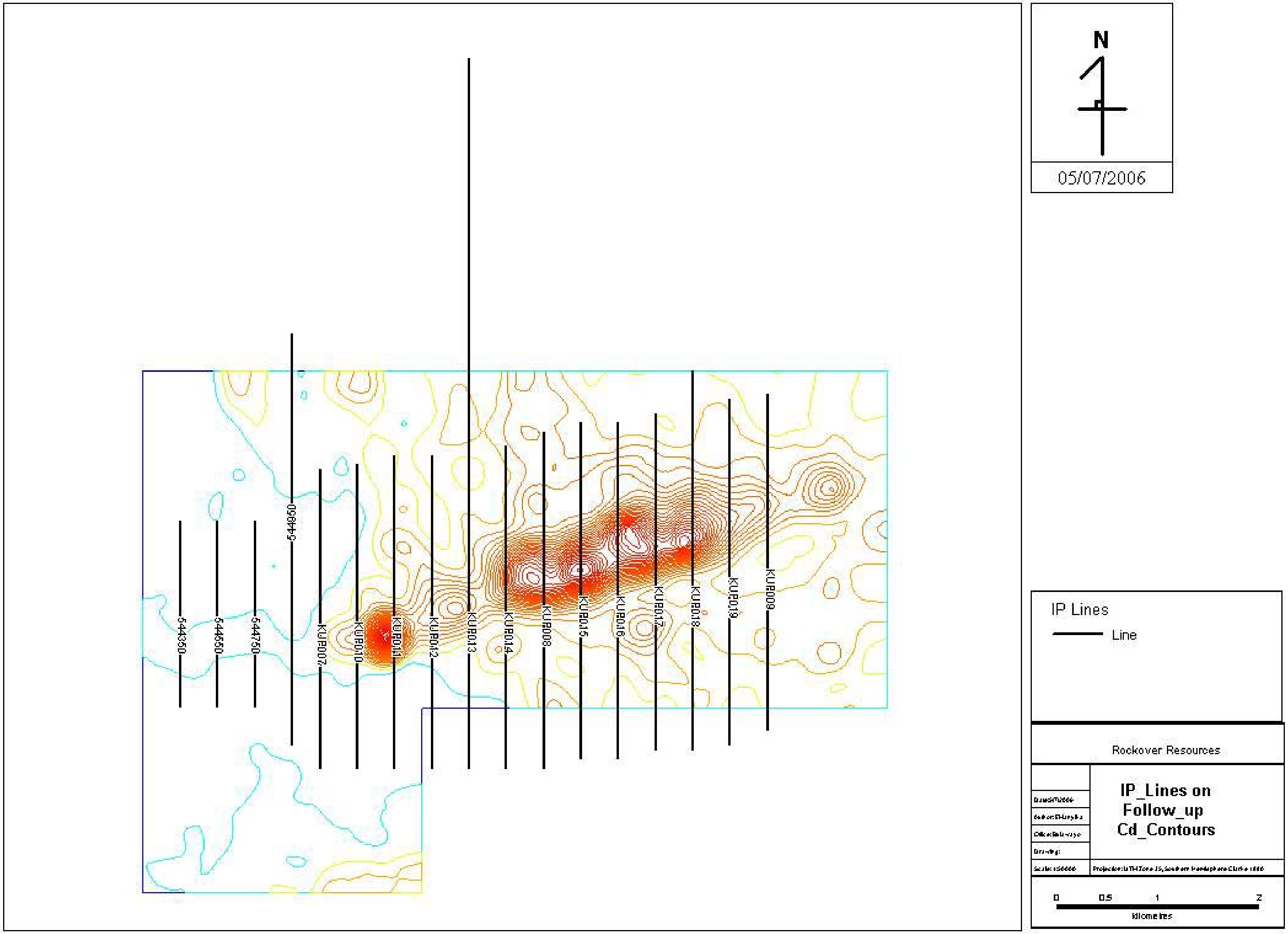

Fig. 1.18 Cadmium concentration contour map.

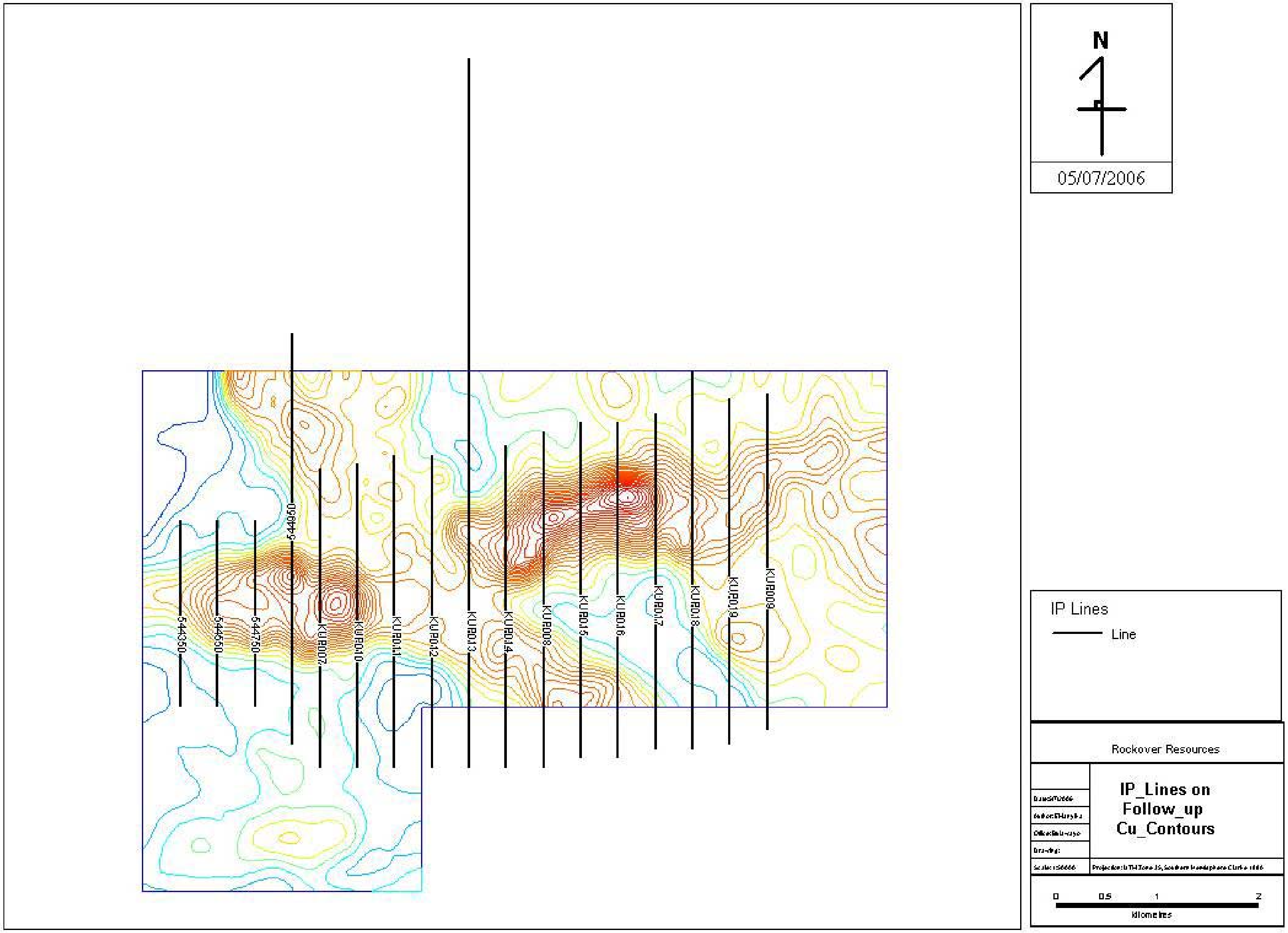

Fig. 1.19 Copper concentration contour map.

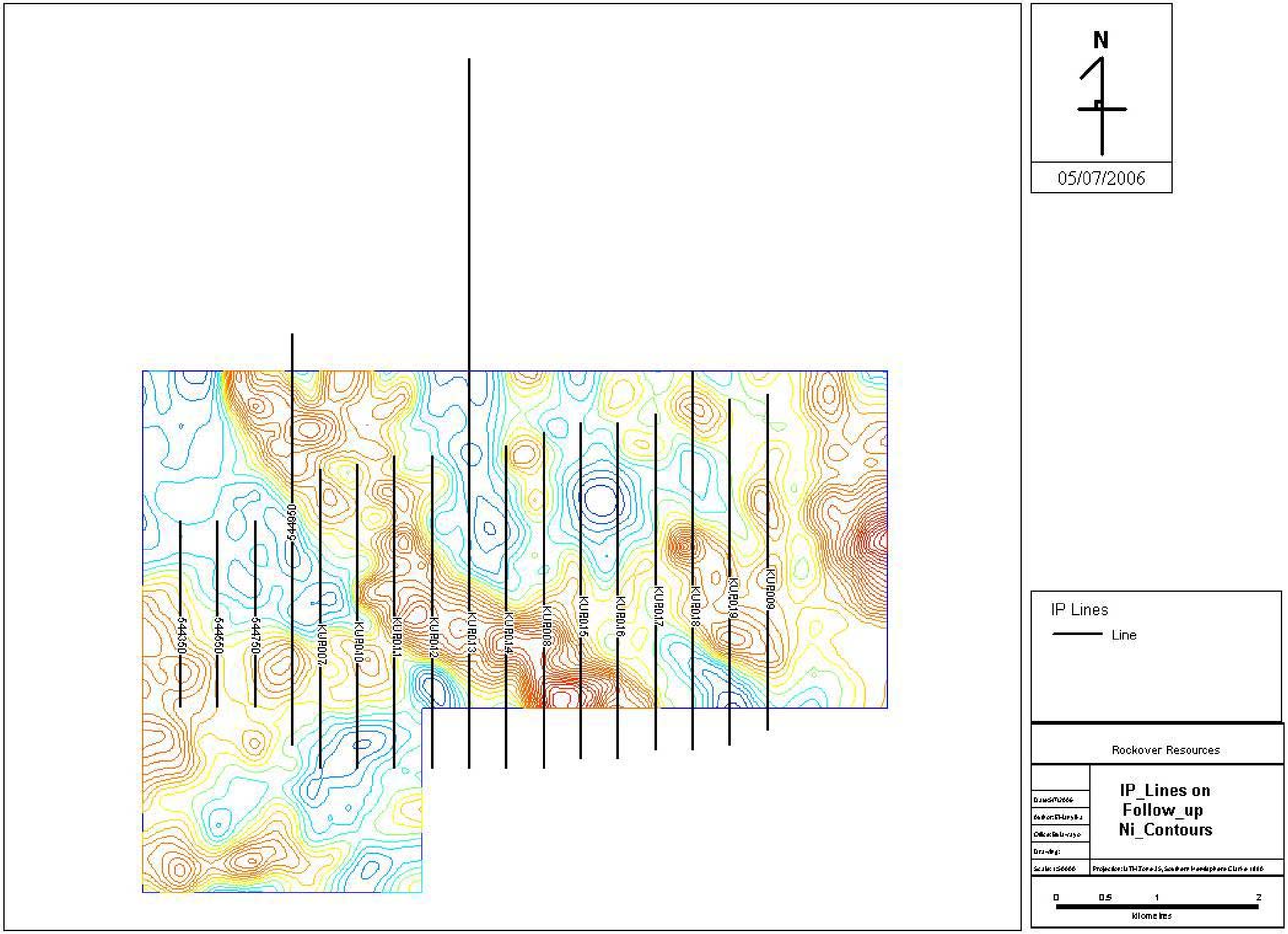

Fig. 1.20 Nickel concentration contour map.

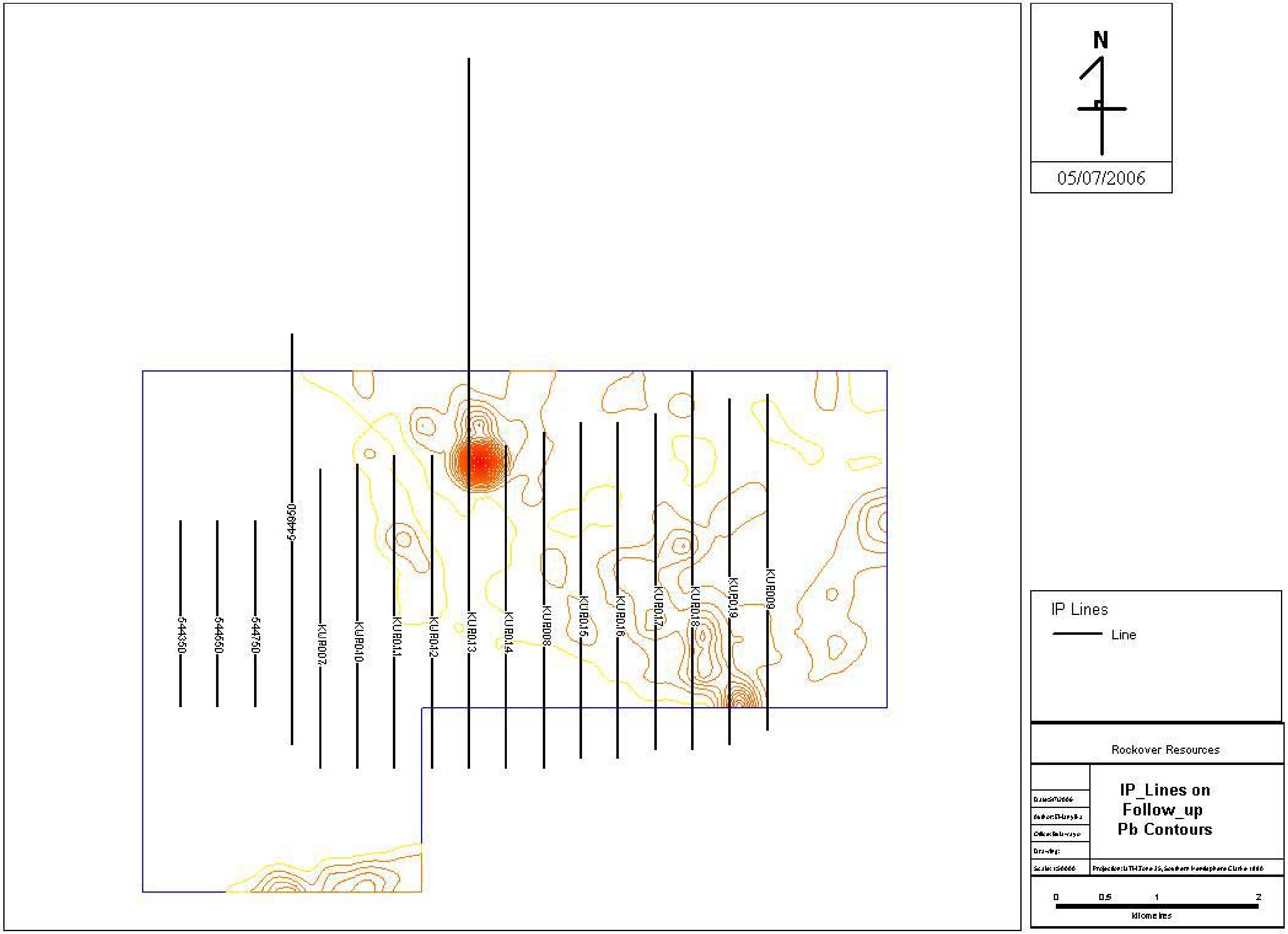

Fig. 1.21 Lead concentration contour map.

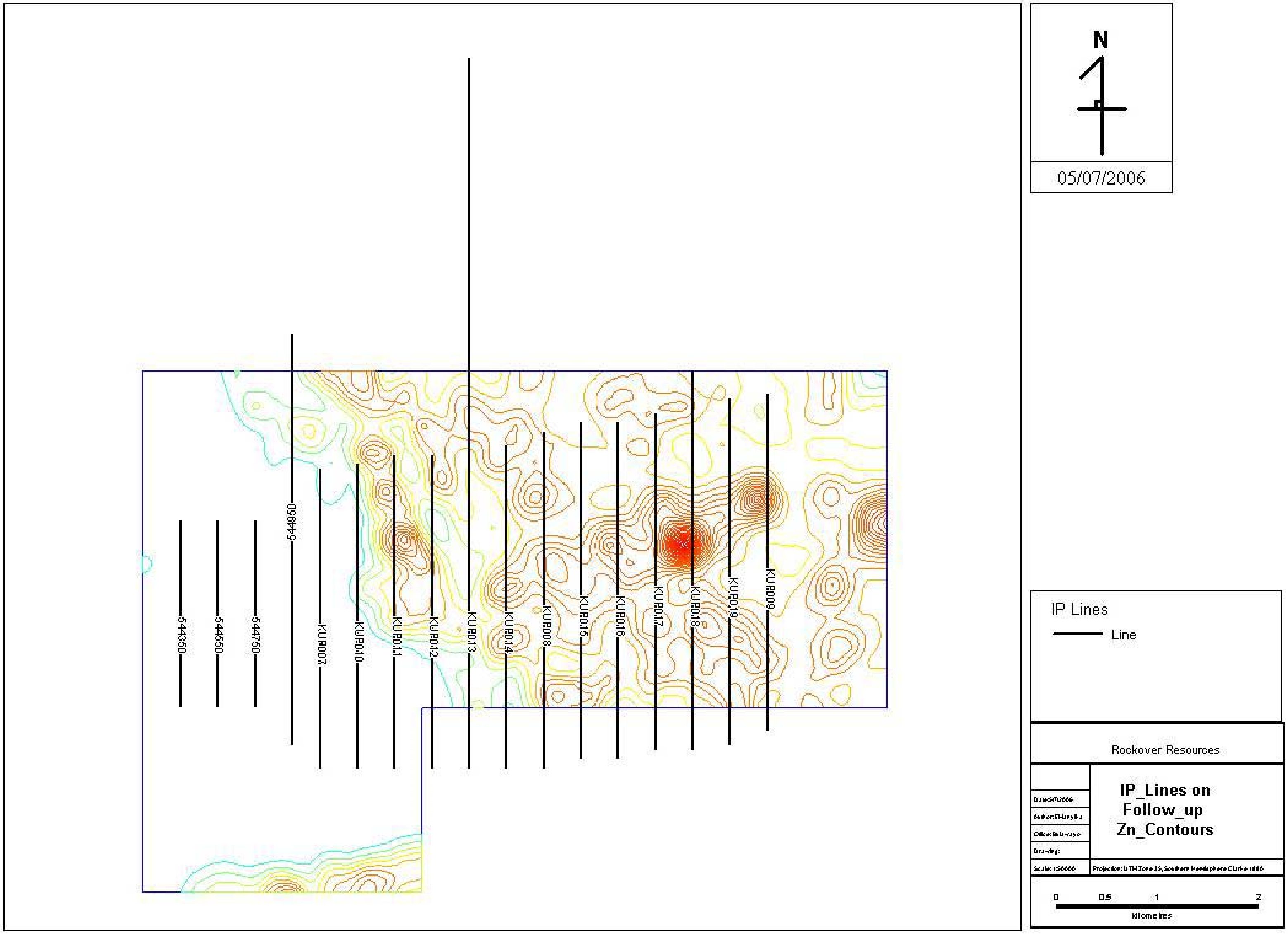

Fig. 1.22 Zinc concentration contour map.

At the time of writing, the first diamond drillhole of the Kupa grid was sunk at an inclination of $-45°$S. It attained a depth of 295,20 m and went through a downhole depth of 28,20 m in the Kalahari cover. Below this was a deeply weathered granitoid and a sheared weathered metabasalt. Sulphides in greenstones and quartz-calcite veins were also intersected. More boreholes were planned in a grid pattern; unfortunately, this information was not available to the author.

1.3.2 Geophysics

The study area had been covered by several geophysical surveys which included aeromagnetic, horizontal loop electromagnetic (HLEM), induced polarisation (IP) and gravity which are discussed below.

The Canadian International Development Agency (CIDA) sponsored a national aeromagnetic survey done in three phases: phase 1 from May to July 1983, covering most of the greenstone belts on the craton; phase 2 from August 1988 to February 1989; phase 3 in 1990. The nominal flight line spacing was 1 km at a mean terrain clearance of 305 m. Fig. 1.23 shows a map of the first derivative of the total field over the area of the E.P.O. A centrally located NE-SW trending magnetic ‘trough’ is clearly visible with the areas of high magnetic ‘relief’ forming exploration targets. The Kupa study area is marked on the map with a box and is in such a prospective locality.

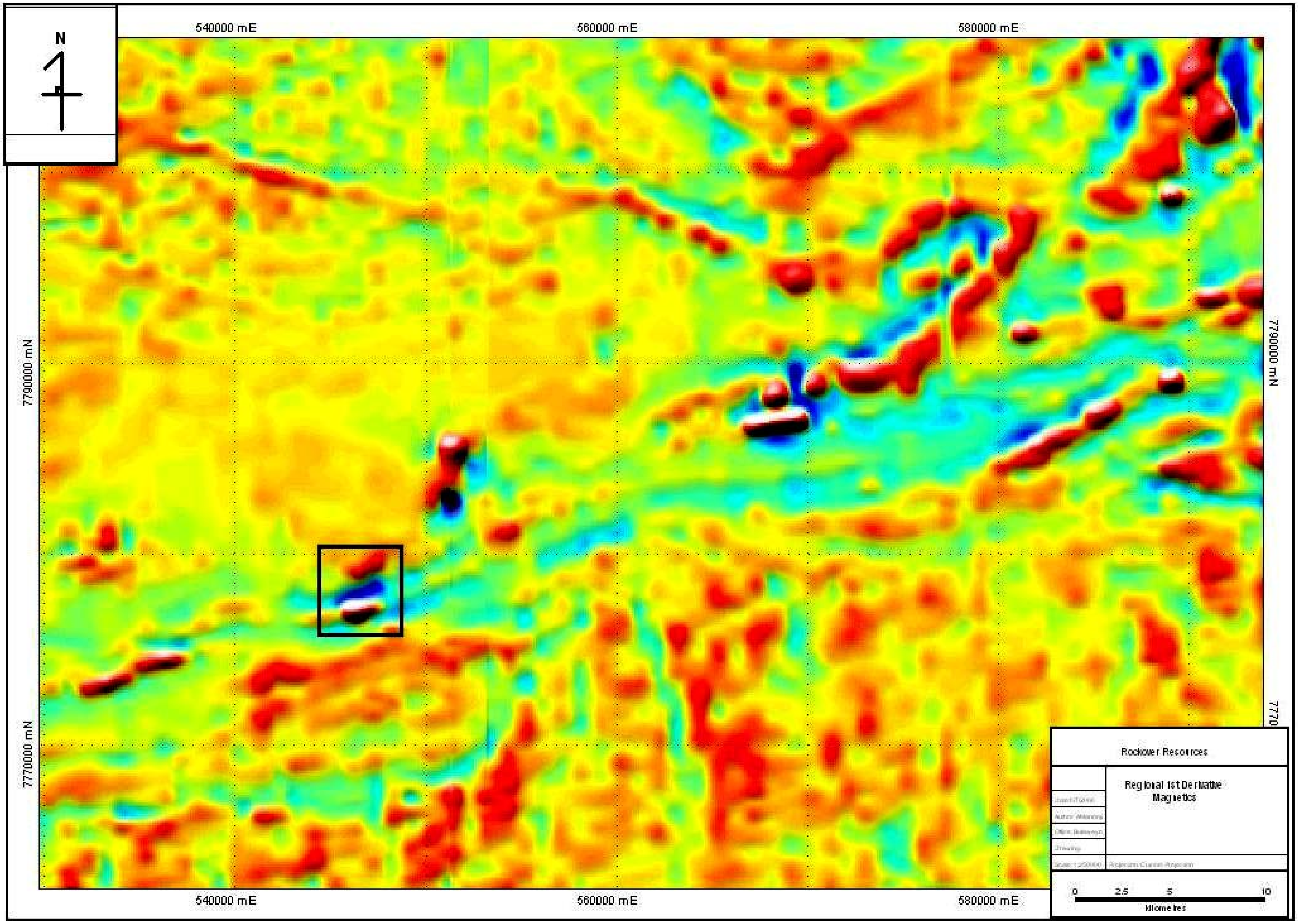

Fig. 1.23 Regional first derivative magnetic map with the box showing the Kupa exploration area.

Canister contracted Fugro Airborne Surveys c. 2003 to do airborne horizontal magnetic gradient surveys over some of their E.P.O. acreage. A fixed wing aircraft was used with a sensor mean terrain clearance of 60 m. The flight line spacing was 75 m with a tie line spacing of 750 m and a flight line trend of 090º i.e. E-W. Three Scintrex CS2 caesium vapour magnetometers were employed using a recording interval of 0,1 s translating to approximately a 9 m station interval. The map produced (Fig. 1.24) is a total magnetic intensity, horizontal gradient enhanced, first vertical derivative with a sunshaded azimuth of 090º and an elevation of 045º.

A Volcanogenic Massive Sulphide deposit (VMS) model has been proposed (Manda, pers. comm., 2006) from the magnetic signature of Fig. 1.24. The large circular feature in to the north of the grid has been suggested as the igneous heat driver (magma chamber) which mobilised mineral rich fluids along a submarine fault line. These fluids were derived from percolating sea water which leached out the surrounding volcanic country rocks and deposited sulphides into the sea floor sediments. This resulted in the zonation of the sulphides due to the different temperatures of precipitation (Groves, 1999). This is supported by the soil geochemistry (Figs. 1.17 – 1.22) which also coincides with the horizontal loop electromagnetic method (HLEM) data (Manda, pers. comm., 2006).

The HLEM survey was done from 2005 to 2006 by GPR Zimbabwe. Frequencies employed were 222, 444, 888 and 1 777 Hz. The HLEM results, however, were not supplied to the author.

A number of lines of induced polarisation had also been done by GPR and more lines were being covered during this project. This fieldwork involved the surveying of the infill lines Kup 21, 22 and 23 and the data was used in combination with some of the archived GPR IP data. The latest data collected in the western part of the grid for the 4 lines 544950 to 544350 was not available for analysis.

A reconnaissance gravity survey on a large station spacing was also previously undertaken, however, the results were not available for comparison and interpretation.

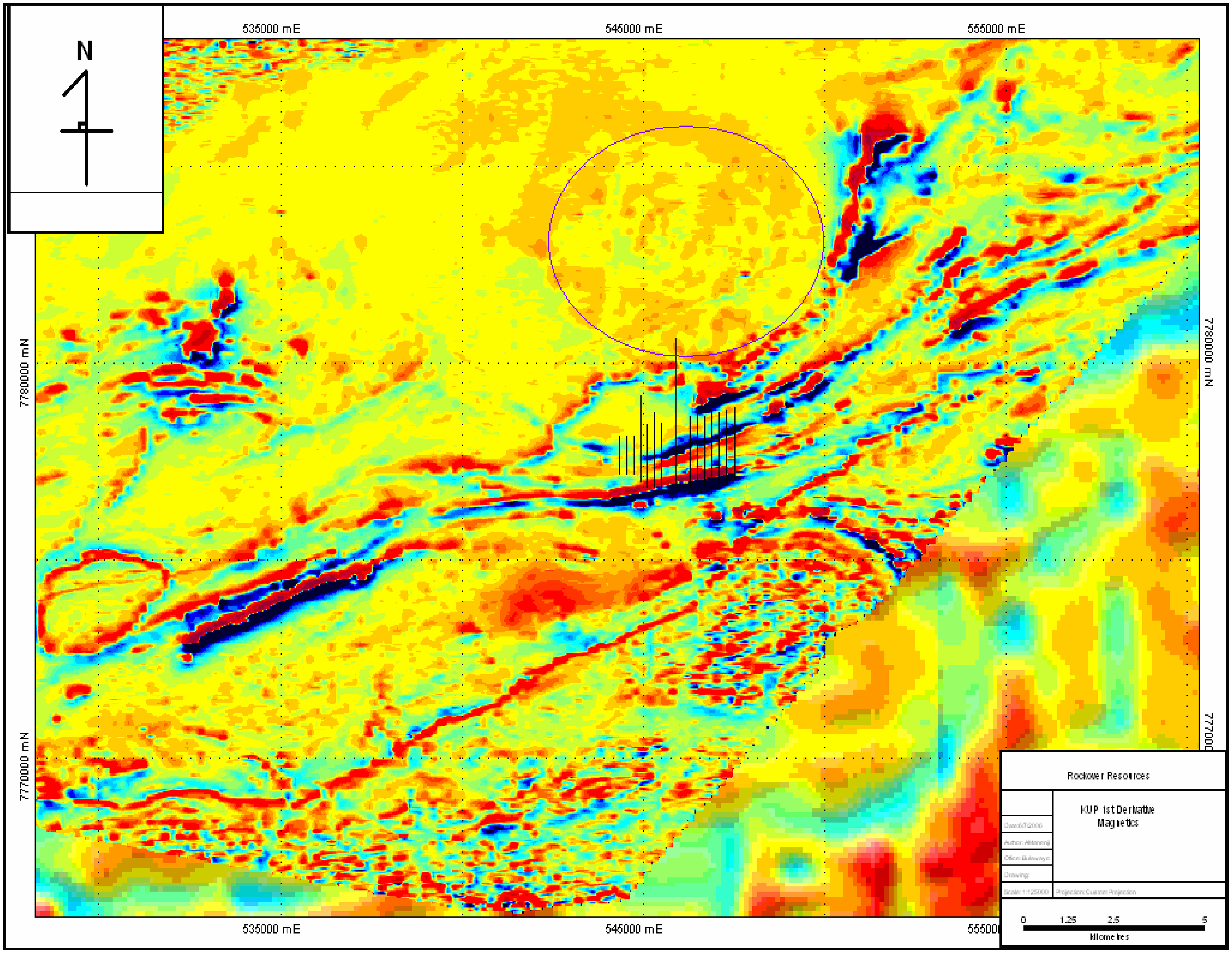

Fig. 1.24 Kupa grid on aeromagnetics background with proposed igneous feature circled.

1.4 Objectives of study

The aims of this study were to use additional geophysical techniques to the on-going exploration to help further define the potential mineral resource before drilling. The new methods to be employed were gravity, radiometrics and turam in addition to infilling IP lines. At the same time, Canister would also carry out a ground magnetic survey and provide the data to the author for processing and interpretation.

The rationale for using another electromagnetic method was that the turam technique has the ability to probe deeper than the HLEM and is less susceptible to coupling with the overburden. Fig. 1.25 shows the 'boxes' that were 'cut' in the bush for the proposed 500 m x 1 000 m transmitter loop. It was to have a 50 m overlap to ensure that all the lines traversing its length were covered. Unfortunately despite many attempts, equipment failure forced the turam survey to be abandoned.

The radiometric survey aimed at testing the effectiveness of using this technique to probe below the sand cover whilst the gravity method was used to define and delineate any dense bodies and any correlation to the target ore body. The infill IP lines would improve the IP coverage and the ground magnetic survey was designed to improve the resolution of the mapped IP and aeromagnetic anomalies.

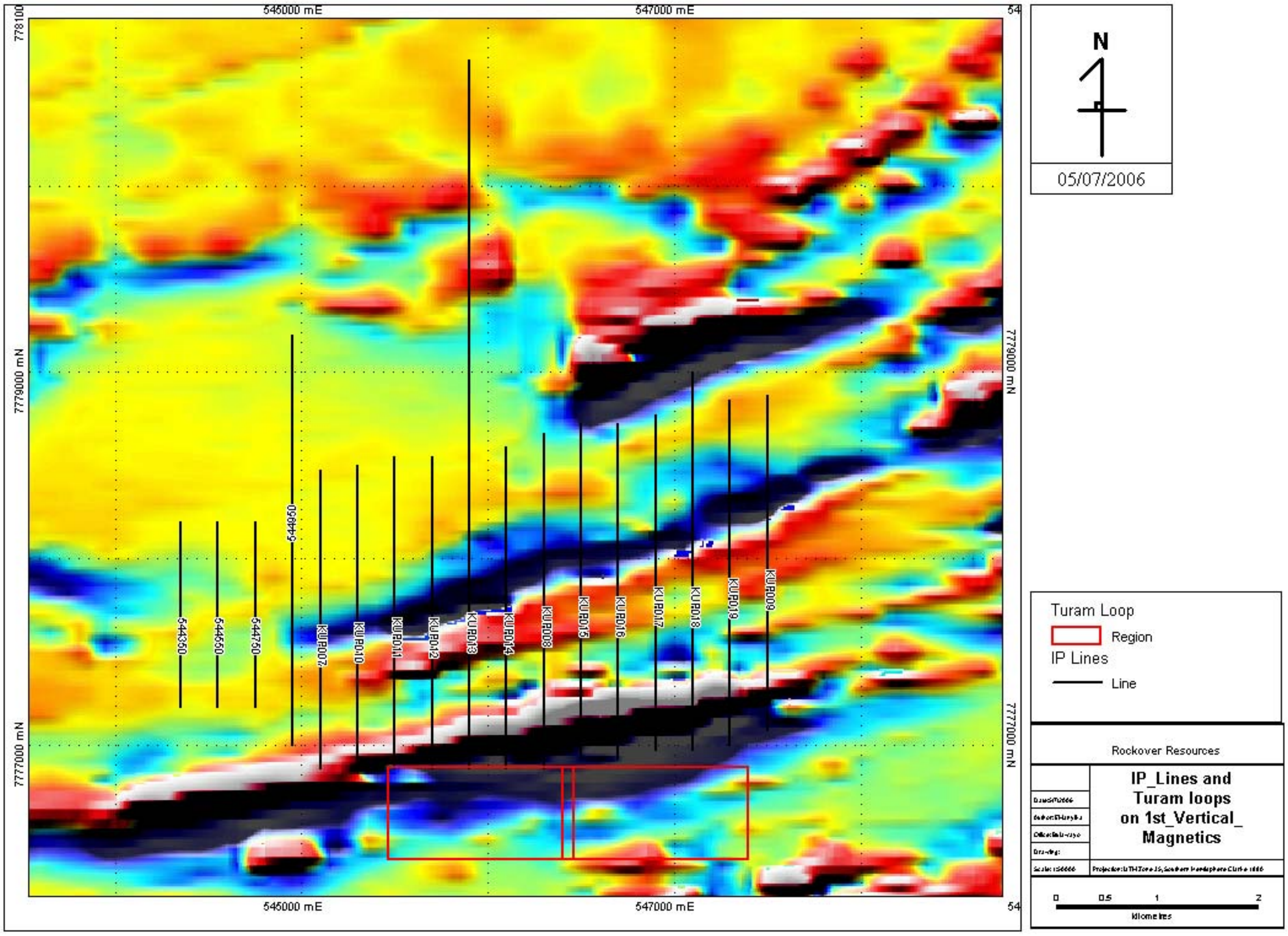

Fig. 1.25 Turam loops and Kupa grid on an aeromagnetic background (Fig. 1.24).

Chapter Two

The Gravity Method

2.1 Introduction

In gravity surveying, subsurface geology is investigated on the basis of variations in the Earth's gravitational field generated by lateral differences in the distribution of mass in the Earth's crust. The underlying concept is the idea of a causative body which has an anomalous density and causes a localized perturbation in the gravitational field known as a gravity anomaly. Sensitive instruments called gravity meters or gravimeters are used to measure relative values of gravity at different places (or stations) within a survey area. Any variations are interpreted in terms of a probable subsurface ore body or structural geologic target at a calculated position, size, shape and depth (Kearey & Brooks, 1988).

2.2 Theory

Newton's law states that the gravitational force of attraction, $\vec{F}$, exerted by two point masses m_1 and m_2 on each other is proportional to the magnitudes of their masses and inversely proportional to the square of the distance, r, that separates them:

$$\vec{F} = -\frac{Gm_1m_2}{r^2}\hat{r} \quad \text{.............................. (2.1)}$$

where the universal gravitational constant G = 6,672 598 5 x 10^{-11} N m^2 kg^{-2} (Lowrie, 1997) and $\hat{r}$ is a unit vector directed along $\vec{F}$.

The acceleration of a small mass m due to a spherical, homogeneous, non-rotating Earth of mass M of radius R on its surface is given by

$$\vec{g} = -\frac{GM}{R^2}\hat{r} \quad \text{………………………….……..} \quad (2.2)$$

with $\hat{r}$ being directed away from the Earth's centre. This is known as the acceleration of gravity or simply gravity (after Telford et al., 1990). Since gravity is a conservative field,

$$\vec{F} = \nabla U \text{ (Blakely, 1996).} \quad \text{………..……..…} \quad (2.3)$$

The gravitational potential, *U*, on the surface of such an Earth is defined by

$$U = -\frac{GM}{R}. \quad \text{………………...…………..……} \quad (2.4)$$

2.3 Gravity field of the Earth

All exploration gravity measurements are made in the gravitational field of the Earth. Therefore, knowledge of this field is required so that a proper allowance can be made for it when reducing gravity readings to a form useful for indicating geologic structure (Nettleton, 1976).

At any point, the gravimeter responds to its entire environment and thus measures the total (vector) field.

$$\vec{F}_T = \vec{F}_E + \vec{F}_U \quad \text{.............……………………....} \quad (2.5a)$$

$$\vec{F}_E = \vec{F}_G + \vec{F}_C \quad \text{...} \quad (2.5b)$$

where T is total, E is earth, U is universe, G is gravitational and C is centrifugal.

A gravity anomaly is calculated as $\Delta g = g_{obs} - g_{pred}$ ………………..… (2.6)

where g_{obs} is the observed (measured) gravity at a point and g_{pred} is the predicted (calculated) gravity at that point based on an idealized model of the Earth. This is called the normal Earth whose mass, shape and angular velocity are chosen to be a best fit to those of the actual Earth and are agreed to internationally (Fig. 2.1).

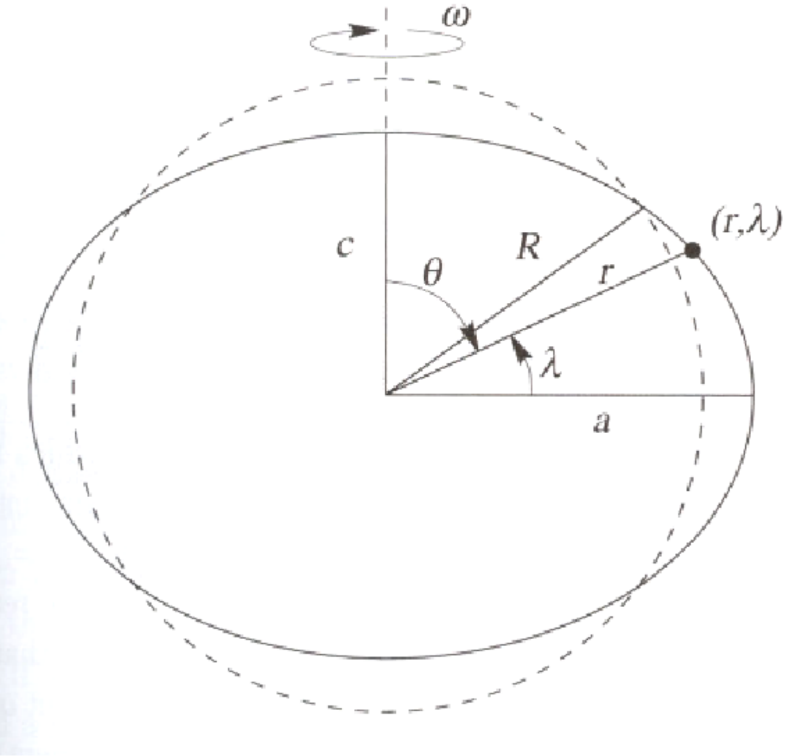

Fig. 2.1 Rotating ellipsoid Earth parameters. The parameters are: λ, geocentric latitude; θ, co-latitude; ω, angular velocity; *R*, radius of spherical earth; *r*, distance from centre; *a*, equatorial radius; *c*, polar radius.

The geopotential, $U = V + C$, ... (2.7)

where $C = \frac{1}{2}\omega^2 r^2 \cos^2 \lambda$ is the centrifugal potential. From a differential calculus and spherical harmonic analysis, Blakely (1996) shows that the gravitational potential, *V*, on the normal Earth is:

$$V(r,\theta) = -\frac{GM}{r}\sum_{n=0}^{\infty}\left(\frac{a}{r}\right)^n \sum_{m=o}^{n}\left(\alpha_n^m \cos m\phi + \beta_n^m \sin m\phi\right)P_n^m(\theta) \quad \text{................} \quad (2.8)$$

$$= -\frac{GM}{r}\left\{J_0 - \sum_{n=2}^{\infty} J_n \left(\frac{a}{r}\right)^n P_n \sin\lambda\right\} \quad \text{...} \quad (2.9)$$

where ϕ is the longitude, J_0 and J_n are Bessel functions of order 0 and n respectively, P_n are the Legendre polynomials, P_n^m are the associated Legendre polynomials of degree n and order m, α_n^m and β_n^m are the weighting coefficients of the infinite individual masses contributing to the gravitational potential, n and m being integers.

However, the symmetry of the spheroid greatly simplifies this equation with the potential having no dependence on ϕ, so $J_n = \alpha_n^0$, $\alpha_n^m = 0 \;\; \forall m \neq 0$, leading to a normal gravity formula ($g_n(\lambda)$) at any latitude:

$$g_n(\lambda) \approx g_e(1 + A_1 \sin^2 \lambda + A_2 \sin^2 2\lambda)\,, \quad \ldots\ldots\ldots\ldots \quad (2.10)$$

where g_e is the gravity at the equator and the coefficients A_1, A_2 are determined from the Geodetic Reference System of 1980 (GRS80) (see appendix A2.3). The previous GRS formula was the GRS67 (Parasnis, 1986):

$$g_{1967} = 9{,}780318(1 + 0{,}0053024 \sin^2 \phi - 0{,}0000059 \sin^2 \phi) \text{ m s}^{-2} \ldots\ldots \quad (2.11)$$

It differs from the 1980 formula by the following equation:

$$g_{1980} - g_{1967} = 8{,}316 + 0{,}782 \sin^2 \phi - 0{,}007 \sin^4 \phi \text{ m s}^{-2} \quad \ldots\ldots\ldots\ldots \quad (2.12)$$

The units used in geophysical exploration are:

1 gravity unit (g.u.) = 0,1 milligal (mGal) $=10^{-6}$ m s^{-2} .

2.4 Gravity reduction

Density variations are relatively small, and the gravity effects of local masses are very small compared with the effect of the background field of the Earth as a whole (often 1 in 10^6 to 10^7) (Telford et al., 1990). Thus before the results of a gravity survey can be interpreted, it is necessary to correct for all the variations in the Earth's gravitational field which are not due to the underlying rocks. These are instrument, tidal, latitude, elevation and terrain and are explained below.

Astronometrical tidal variations are due to the cyclical effects of the Sun and Moon in their relative orbits and exhibit diurnal to seasonal periods. Gravity also changes with latitude as shown in the normal gravity formula (eqn. 2.10) and it also diminishes with altitude above sea-level. However, the decrease of gravity with altitude is lower by an amount equal to the attraction of a mass of rock between sea-level and the gravity station. The surrounding terrain also affects the gravity measurement especially in the vicinity of the gravimeter in rugged topography. While taking measurements, the gravimeter's readings will change with time or drift and this effect should be corrected for before the readings can be made useful. The process of removing the above effects is known as gravity reduction.

2.4.1 Tidal correction

The normal value of gravity at any point will vary cyclically during the course of the day by as much as 3 g.u. (Dobrin and Savit, 1988) due to the tidal attraction of the Sun and Moon. This effect (Δg_t) can be corrected for by using published tables or a computer program for predicting the tidal gravity based on the formula:

$$\Delta g_t = -\frac{3}{2}\frac{GMR}{d^3}\left(\cos 2\psi + \frac{1}{3}\right) \text{ ....} \quad (2.13)$$

where M is mass of the Sun or Moon, d is the mean distance from the Sun or Moon and ψ is the zenith angle.

2.4.2 Instrument drift

Gravimeter readings change with time as a result of elastic creep in the springs, producing an apparent change in gravity with time at a given station. This instrument drift can be determined by repeating measurements at the same station(s), typically every

1 - 2 hours. The differences between successive measurements at the same station are plotted to produce a drift curve (Fig. 2.2).

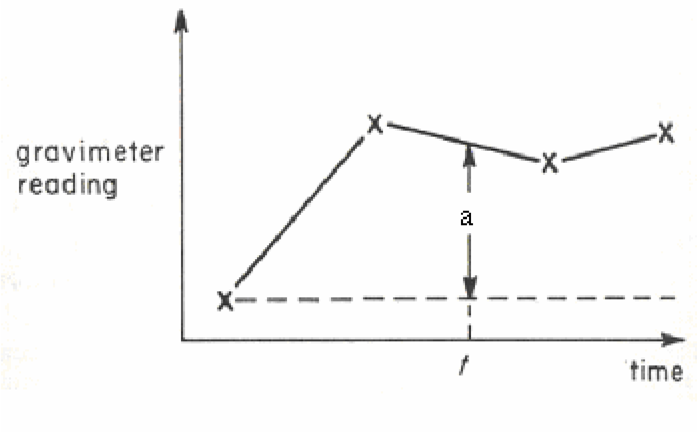

Fig. 2.2 A gravimeter drift curve plotted from repeated readings at a fixed location. The drift correction for a reading taken at time *t* is *a*.

Measured gravity values at intervening stations can be corrected by subtracting the amount of drift from the observed gravity value.

2.4.3 Latitude correction

The latitude correction takes into account the increase of gravity from the equator to the poles. This is done by subtracting the theoretical sea-level gravity, $g_n(\phi)$, from the observed value. However, for small-scale surveys which extend over a latitude range of less than 1°, and not tied into the absolute gravity network, a simpler correction can be made. A local base station is selected, normally at the centre of the grid or at some convenient and stable location, for which the horizontal gravity gradient can be determined. This is done by differentiating equation (2.10) for a N-S component of distance to get

$$\Delta g_{lat} = 8{,}108 \sin 2\phi \; \Delta L \text{ g.u./km}, \quad \ldots\ldots \quad (2.14)$$

where ΔL is the station distance in km from the base station. For a survey in the southern hemisphere, gravity decreases towards the equator, i.e. northwards. So this correction is added to the measured values for stations north of the base.

The correction is linear for distances in the N-S direction of the order of 1-2 km on either side of the base. For an accuracy of $\pm 0{,}1$ g.u., the latitudinal position of the base station needs to be known to within $\pm$ 10 m (Reynolds, 1997).

The 1967 theoretical sea-level gravity formula was used in this study since other gravity studies by Canister around Kupa used the 1967 formula.

2.4.4 Free-air correction

Assuming a spherical Earth of uniform density, using equation (2.2), the free-air correction is the predicted difference between gravity at sea-level and at height *h* in air:

$$\Delta g_{FA} = g_h - g_0 \approx -\frac{2g_0 h}{R} \quad \text{..} \quad (2.15)$$

$$= 3{,}0828h \text{ g.u./m, where } h \text{ is in m.}$$

This can be improved by using the normal Earth model and GRS80 parameters to give:

$$\Delta g_{FA} = k_{1980}h \approx (3{,}087798 - 0{,}004390\sin^2\phi + 0{,}73\times 10^{-6}h)h \quad \text{.........} \quad (2.16)$$

where *k* is the free-air gradient. In Zimbabwe at 20° latitude this gives:

$k_{1980} = 3{,}0873$ g.u./m and $k_{1967} = 3.086$ g.u./m .

2.4.5 Bouguer correction

The Bouguer correction is used to account for the rock mass between the station and sea-level (Fig 2.3). It calculates the extra gravitational pull exerted by a rock slab of thickness *h* and mean density ρ which results in measurements of gravity being overcorrected by an amount:

$$\Delta g_B = 2\pi G\rho h \text{ (g.u.)} \quad \text{...} \quad (2.17)$$

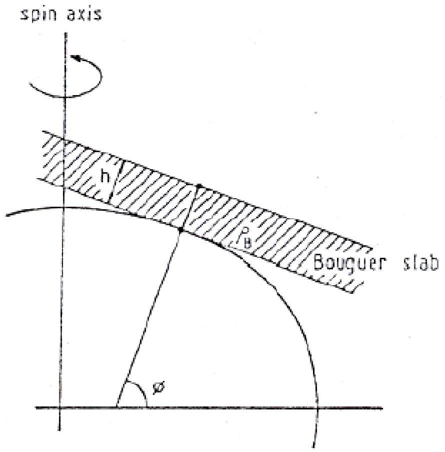

Fig. 2.3 The Bouguer slab (Podmore, 1985).

The free-air and Bouguer corrections can be combined into one elevation correction

$$\Delta g_E = \Delta g_{FA} - \Delta g_B$$

$$= (3{,}086\text{-}4{,}192\times10^{-4}\ \rho)h\ \text{(g.u.)} \quad \ldots\ldots\ldots\ldots\ldots\ldots \quad (2.18)$$

A typical value is $\Delta g_E =$ 1,967h g.u. for $\rho = 2670$ kg m^{-3}.

This correction completes the simple Bouguer anomaly which is used for flat countryside such as that of the survey area. Hence the simple Bouguer anomaly is

$$g_{BA} = g_{obs} - (g_{lat} + g_{FA} + g_B) \quad \ldots\ldots\ldots\ldots\ldots\ldots \quad (2.19)$$

where g_{obs} refers to an observed gravity which is obtained by conversion from instrument units (relative gravity) to gravity units which is then corrected for tidal variations and instrument drift, i.e. $g_{obs} = (g_{inst} + g_{TD} - g_{ID})\times$ scale factor, where g_{inst} is the gravimeter reading, g_{TD} is the tidal correction, g_{ID} is the instrument drift and the scale factor is discussed in section 2.5.

2.4.6 Terrain correction

The terrain contribution reduces the value of g_{obs} at a station due to the excess mass of hills and the deficiencies of valleys. There are several graphical and computer programs that are available to correct for surveys in regions of hilly topography. A well known scheme is the Hammer zone chart developed by Hammer (1939). Computer programs use square grids and a digital terrain model e.g. Kane, 1962 and Bott, 1959 (Nettleton, 1976).

The Kupa area is fairly flat and hence no terrain corrections were required.

2.5 Instrumentation

Gravimeters are basically spring balances carrying a constant mass. Variations in the weight of the mass caused by variations in gravity cause the length of the spring to vary and give a measure of the change in gravity. They measure the relative gravity differences between two points:

$$\Delta g = k \times \Delta \text{ (dial reading) (g.u.)} \quad \ldots\ldots\ldots\ldots\ldots\ldots\ldots\ldots\ldots\ldots\ldots \quad (2.20)$$

where k is a calibration factor that converts meter units to gravity units. This is a constant for some gravimeters (e.g. Worden) but may require a table for others (e.g. LaCoste & Romberg).

Gravimeters are portable, rugged, very sensitive (to $\pm 0{,}1$ g.u.) and fairly stable over time. They have a thermostat element to keep the temperature of the springs constant to ~$0{,}001\,^{\circ}\mathrm{C}$ (Nettleton, 1976) and about $10\,^{\circ}\mathrm{C}$ above any maximum ambient outdoor temperature (e.g. $48{,}2\,^{\circ}\mathrm{C}$ for the G-382 used in this study). Some gravimeters use fused quartz for the springs because it has a low temperature coefficient (e.g. Worden) whilst others use metal for ruggedness (e.g. LaCoste & Romberg). The pressure is kept fairly constant by sealing the moving system in a vacuum as pressure changes would alter its buoyancy.

Non-magnetic materials are used to minimise the effect of the geomagnetic field. Gravimeters need to be levelled so that the instrument measures the vertical component of gravity accurately. This is achieved by the use of very sensitive spirit levels and three adjustable foot screws. Some modern gravimeters include auto levelling, e.g. Scintrex CG3 and CG5.

The gravimeter used for this project was a LaCoste & Romberg model G-382 with a predetermined reading line of 3,10. On a LaCoste & Romberg gravimeter, the nulling dial is used to bring the beam back to the equilibrium position at the reading line (chosen position of greatest sensitivity) (see Fig. 2.4).

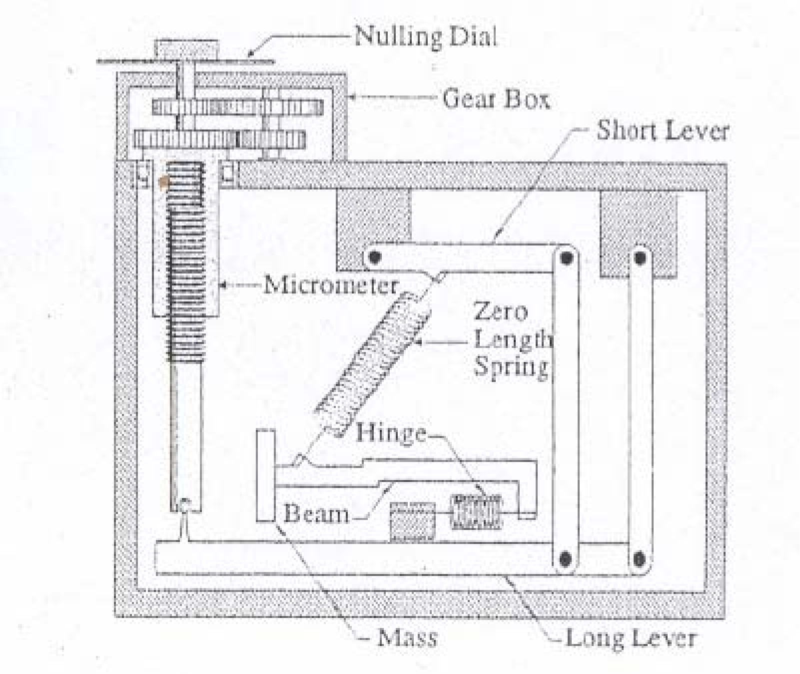

Fig. 2.4 Simplified cross-section of the LaCoste-Romberg gravimeter. Taken from LaCoste-Romberg Instruction Manual, model G and D meter, 1992.

The moving mass can be clamped so that the gravimeter is less sensitive to vibrations while being transported.

2.6 Field procedures

In mineral exploration, gravity is normally employed as a secondary detailed method for confirmation and further analysis of anomalies already outlined by magnetic and/or electrical techniques (Telford et al., 1990). To achieve the required precision of 0,1 g.u., the latitude should be known to within 10 m and the elevation differences from the datum level must be known to better than 5 cm (Parasnis, 1986).

Ideally, a conveniently located reference site (base station) where the absolute gravity has already being determined is established in the locality. The base station should be one of the sites in the 1971 International Gravity Standardization Net (IGSN71) (Robinson and Coruh, 1988) and the height related to a national bench mark or trigonometric point. However, in many exploration surveys such as this one, where only changes of gravity are deemed to be of interest, no connection to the primary net is made and the differences are simply referred to a local base at which the value of gravity is arbitrarily designated (Parasnis, 1986).

The Kupa gravity survey was done on 5 lines, Kup 13, 15, 17, 19 and WF at 25 m station spacing (see Apps. A1.2, A2.2 and A2.4). The lines were of length 1,8 – 2,0 km, with one long line (Kup 13) running 3,8 km to establish the regional gravity field. The camp site at 20°06.185' S; 27°26.940' E was chosen as the main base (Fig. A1.2.1).

2.6.1 Elevations

Height differences between gravity stations were determined using an optical ‘level’ and a levelling staff (Fig. 2.5).

Fig. 2.5 The 'dumpy level' and staff with a vertical level spirit bubble. A Sokkisha B2 A77744 dumpy level was used.

The level was set up at X (Fig. 2.6) about half-way between two gravity stations. By sighting on the levelling staff, held vertical at gravity station A with the aid of a spirit bubble, the vertical distance h_b between the ground level at the gravity station and the horizontal plane defined by the level can be read off the levelling staff at the cross-hair as shown in Fig. 2.7B.

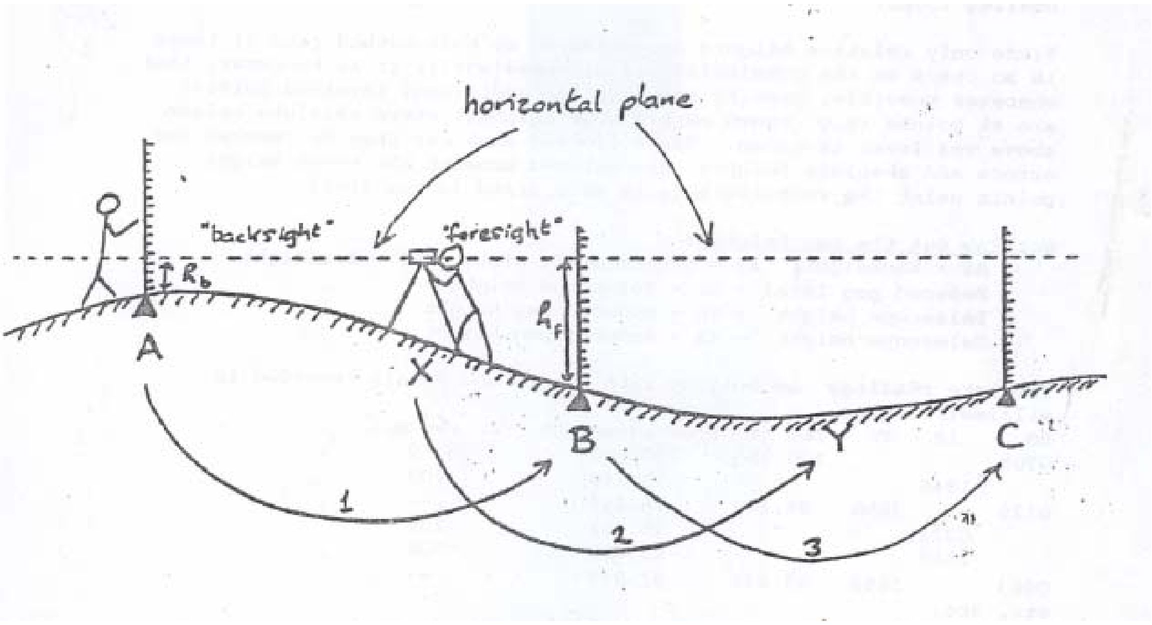

Fig. 2.6 Levelling 'leap frogging' procedure.

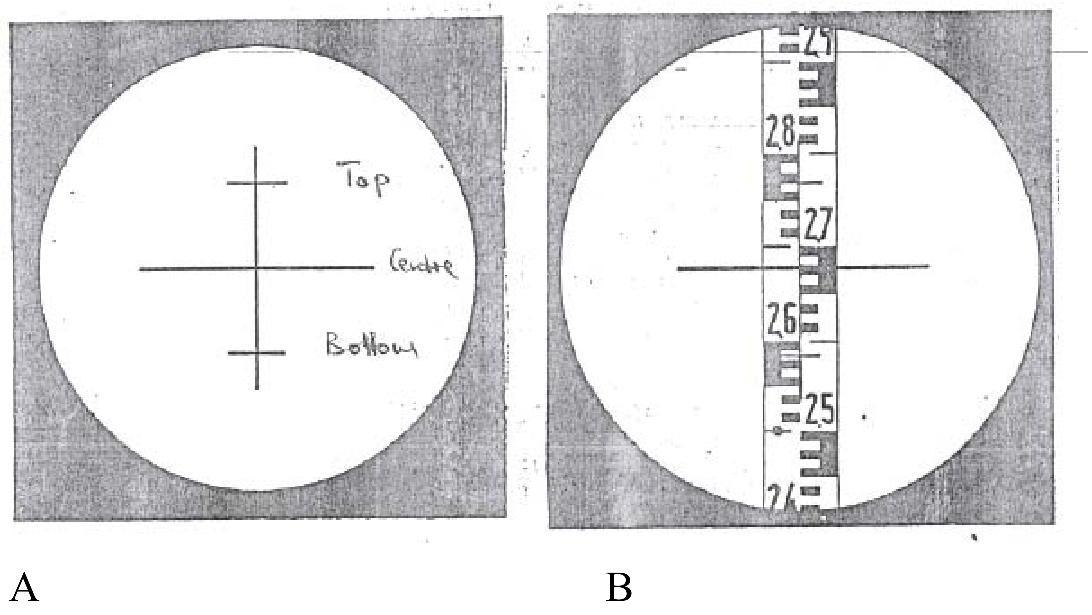

Fig. 2.7 View through the eye-piece. **A**: cross-hairs; **B**: centre cross-hair across levelling staff graduations.

The observation to A is called a "backsight". By moving the levelling staff to station B and rotating the level to look ahead (thus creating a "foresight"), the value of h_f was similarly determined. The difference in height between station A and B is h_b - h_f . As a check on the possibility of mis-readings, the top, centre and bottom readings were taken (see Fig. 2.7A). The average between the top and bottom cross-hair readings should agree with the centre reading to <1,5 mm. Hence the relative heights are accurate to $\pm$ 1,5 mm. Since only relative heights were measured, the first peg of each line was assigned a relative height, say 10 000 mm such that the topography along the line did not drop to negative values. A differential GPS survey with an accuracy in elevation of "15 cm" was done by Datum Surveying Consultants for Canister for the entire grid of 17 lines. This could be used to relate the relative heights to the absolute heights above sea level and to check for any errors.

The raw levelling data was reduced on a PC. The topography from the relative heights was compared to that from differential GPS elevations for all lines (see Fig. 2.8 for line Kup13).

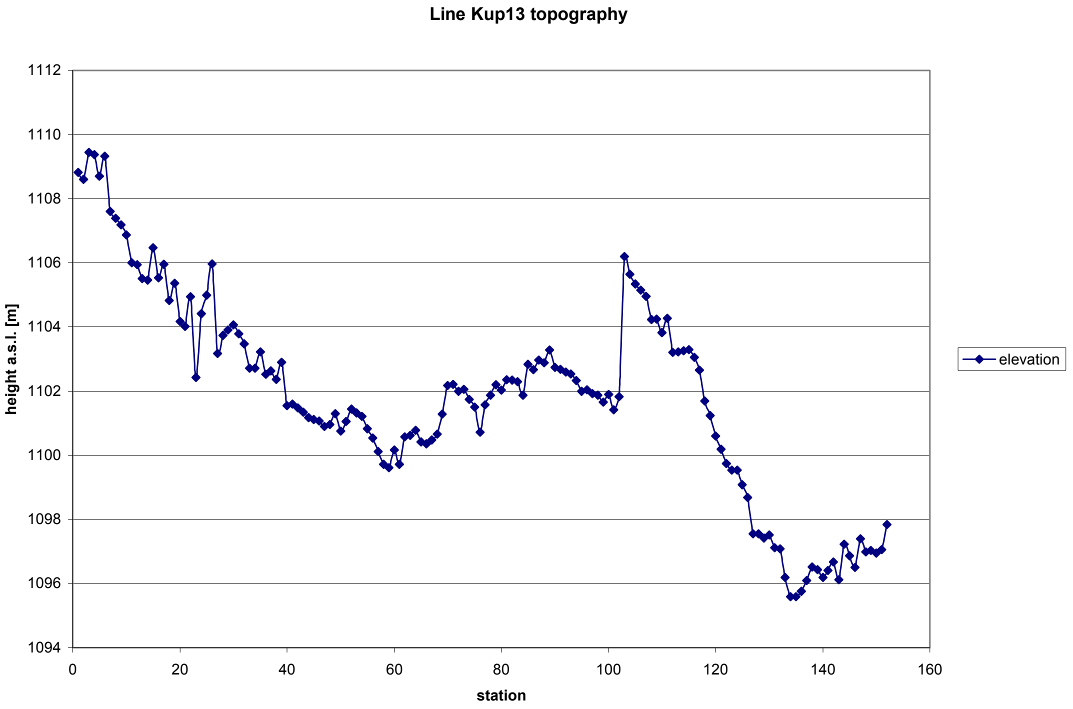

(a)

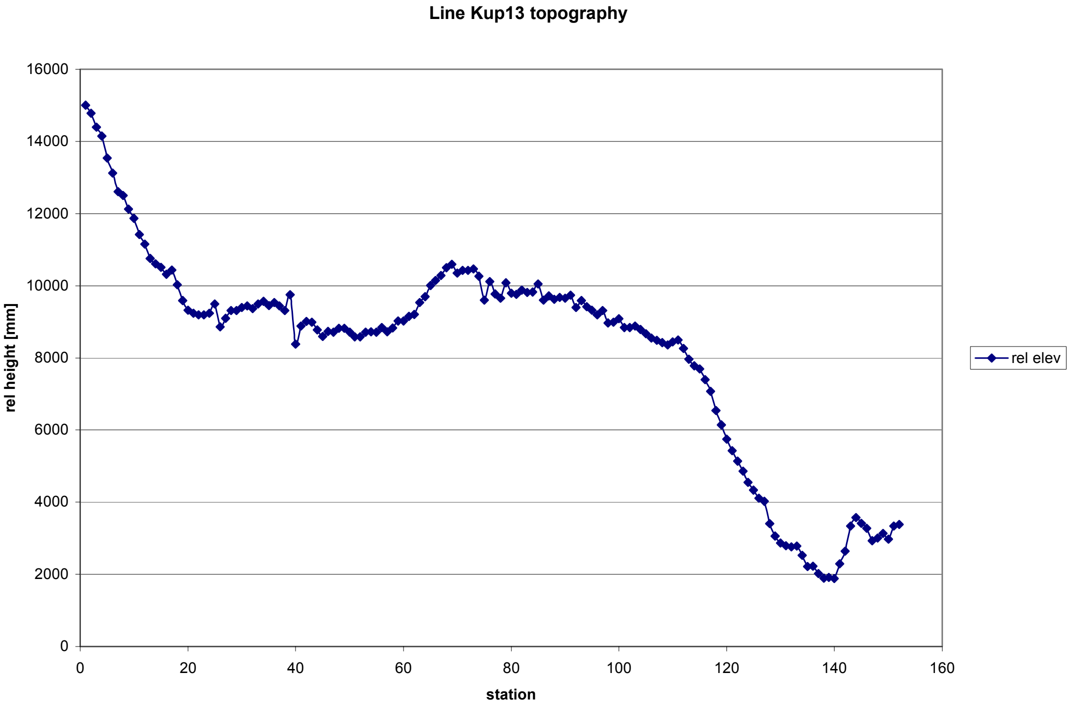

(b)

Fig. 2.8 Comparison between the differential GPS absolute elevations (a) and the levelling relative heights (b).

There is a huge disparity between the two topographic profiles with the differential GPS profile being more irregular. This suggests that the errors in determining the absolute elevations using the differential GPS were greater: hence the levelling exercise was more accurate. Fig. 2.9 shows the margin of error i.e. departure from each other of the two measurements in Fig. 2.8 for a constant datum shift of 1094,284 m applied to the levelling data. Elevations obtained by levelling were used for gravity reduction.

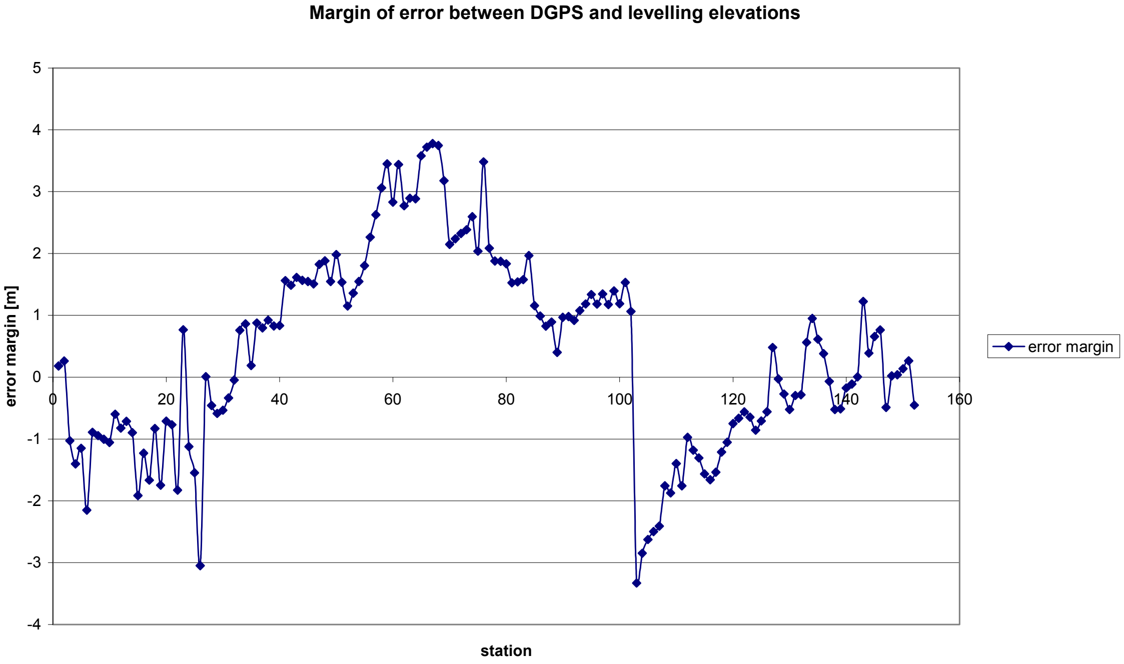

Fig. 2.9 Difference in measurement between the differential GPS (DGPS) and levelling elevations. The levelling data was adjusted for comparison using the altitude of the first peg as determined by the DGPS.

2.6.2 Gravimeter reading procedure

The gravimeter plate was placed firmly on the ground next to a peg (see Fig. 2.10). The plate height and the peg height were measured and recorded. After gently placing the gravimeter on the plate, with the observer's back to the sun, it was levelled using the foot screws.

Fig. 2.10 A gravity station.

The gravimeter was then ‘unclamped’ and the nulling dial adjusted so that the beam was a few units above the reading line. By twisting the dial anticlockwise in careful steps it was possible to make the beam settle over the reading line without ‘overshooting’ it. The reading was then taken to ± 0,001 units using the vernier on the dial. For each line the station, time, gravity reading, plate and peg heights were recorded in a notebook.

2.6.3 Station occupation for drift control

At the beginning and end of each day, a gravity reading was taken at the same position at the camp site. When starting a new line, a base station was chosen at a convenient position on the line (usually near the middle) and this base was ‘tied’ to the camp base station. If the new line was too far from the camp, the base was tied to another base on a closer line. The basic procedure for tying in a new base and station occupation for drift control is shown diagrammatically in Fig. 2.11.

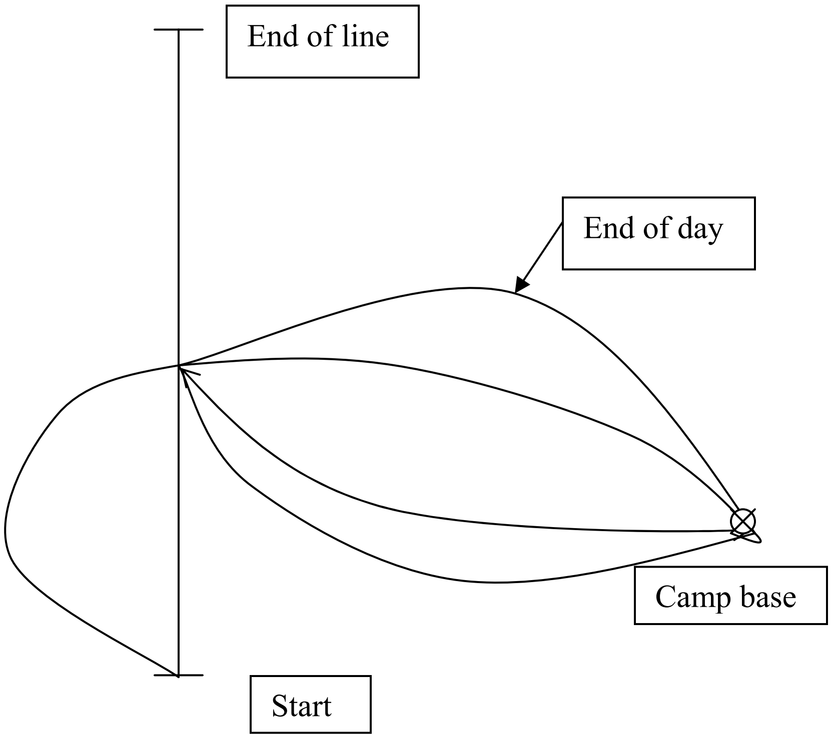

Fig. 2.11 Tying in base B1 on line L1 to camp base BC and station occupation sequence.

Using the procedure indicated in Fig. 2.11 one can calculate the instrument drift using repeated readings at the known base stations. Fig. 2.12 shows one of the drift curves obtained in this study.

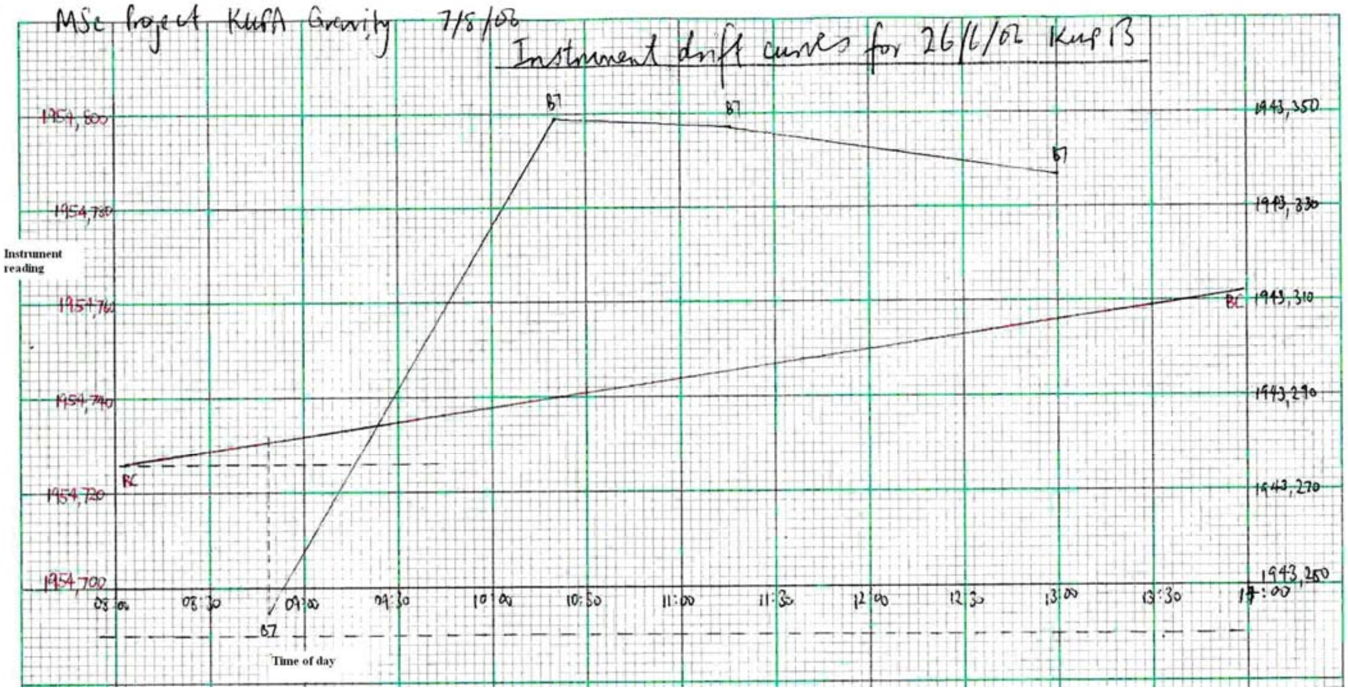

Fig. 2.12 Drift curve for a portion of line Kup 13 surveyed on the 26th of June 2006. The line base was B7 (peg 128) and BC was the camp base.

2.6.4 Field Problems

Where the lines traversed villagers' fields and homesteads, accessibility proved difficult as equipment had to be lifted over fences and thorny hedges (Fig. 1,3). Occasionally survey pegs would be found out of place especially on roads and footpaths. This was probably due to grazing livestock or mischievous children/individuals, and these would be put back at the correct locations. For this reason the optical levelling exercise preceded the gravity survey.

The over reliance on the GPS for positioning was evident from some lines that were not straight and some locations falling outside the cut/surveyed lines. This could have been a result of the fluctuating accuracy due to the availability of satellites or the periodic noise imposed on the satellite signals by the proprietor. Because there was no baseline for the grid, tying the levelling lines together was overlooked and so both the levelling and GPS data was used to get an adjusted elevation for each station (section 2.8.2).

Unreliable power outputs by the electric generators (one for U.Z. and another for G.P.R.) resulted in the batteries not being fully charged and two of the chargers burning out. This caused considerable down time as the gravimeter would require at least 4 hours to heat up and stabilize before use.

2.7 Density Determination

A knowledge of rock density is necessary both for the application of the Bouguer correction and for the interpretation of gravity data. Large hand specimens (~1 kg) representative of the rock units of the area were weighed in air and water on a density balance. The difference in mass provides the volume of the sample and so the dry density can be obtained:

$$V_T = \frac{m_a - m_b}{\rho_w} \quad \ldots\ldots\ldots\ldots\ldots\ldots\ldots\ldots \quad (2.21)$$

and

$$\rho_d = \frac{m_a}{m_a - m_b}\rho_w, \quad \ldots\ldots\ldots\ldots\ldots\ldots\ldots\ldots \quad (2.22)$$

where V_T is the total volume (voids and particles), m_a and m_b are masses of the sample in air and water respectively and ρ_w is the density of water.

For porous rocks, the saturation density was obtained by repeating the above procedure after saturating the rock in water:

$$\rho_p = \frac{\rho_d}{1-p} \quad \ldots\ldots\ldots\ldots\ldots\ldots\ldots\ldots\ldots\ldots \quad (2.23)$$

and

$$\rho_s = \rho_d + p\rho_w, \quad \ldots\ldots\ldots\ldots\ldots\ldots\ldots\ldots \quad (2.24)$$

where ρ_p is the particle density, ρ_d the dry rock density and ρ_s the saturated density. The porosity ratio is

$$p = \frac{V_{voids}}{V_T}, \quad \ldots\ldots\ldots\ldots\ldots\ldots\ldots\ldots\ldots\ldots \quad (2.25)$$

where V_{voids} is the volume of voids.

A total of 18 rock samples (Appendix A1.1) were measured for density determinations and were classified into 8 categories shown in Table 2.1.

Table 2.1 Average dry rock densities for hand specimens collected in the Kupa grid. ρ_w taken as 998,23 kg/m^3 at 20º C and 1 atm pressure (Tennent, 1979).

Rock type	Number of samples	m_a [g] ave.	m_b [g] ave.	ρ_d [kg/ m^3] ave.
Quartz	2	955,25	593,25	2634
Granite	4	1485,75	906,50	2560
Augen-gneiss	2	871,00	535,50	2592
Mylonite-gneiss	1	529,50	323,00	2560
Diorite	3	842,83	563,83	3016
Greenstone	4	982,25	652,13	2970
Sandstone	1	1460,00	950,00	2858
Calcrete	1	1870,00	875,00	1876

The masses were measured to ± 0,5 g on a beam balance making the densities accurate to ± 0,07 % in a 1 kg sample.

2.8 Results

2.8.1 Adjusted heights and gravity anomalies

As explained in section 2.6.4, the relative heights for each line were adjusted to “absolute heights” by adding a datum shift to all the relative heights. The datum shift was obtained by calculating the average difference of the two profiles, i.e. the GPS elevation – the relative height. The adjusted “absolute heights” are presented as topographic profilesfor the lines. The adjusted heights were used to reduce the measured gravity values using the GRS 1967 formula and a Bouguer density of 2670 kg m^{-3}. This was done using the GRAVRED program in Geosoft and the results are presented in the next section.

2.8.2 Gravity and elevation profiles

The reduced gravity profiles for lines Kup 13, 15, 17, 19 and WF are displayed in Figs. 2.13 - 2.2.17 along with their topographic profiles. All the lines display a simple anomaly shape on which a linear or a second order regional can be fitted. Only a qualitative description shall be given. The gravity data is presented in Appendix 2.2.

Caution needs to be taken when comparing the elevation and gravity profiles as the elevation has a large vertical exaggeration. There seems to be little correlation of the gravity profile with the elevations as the anomaly sometimes coincides with high ground or low ground on the different lines.

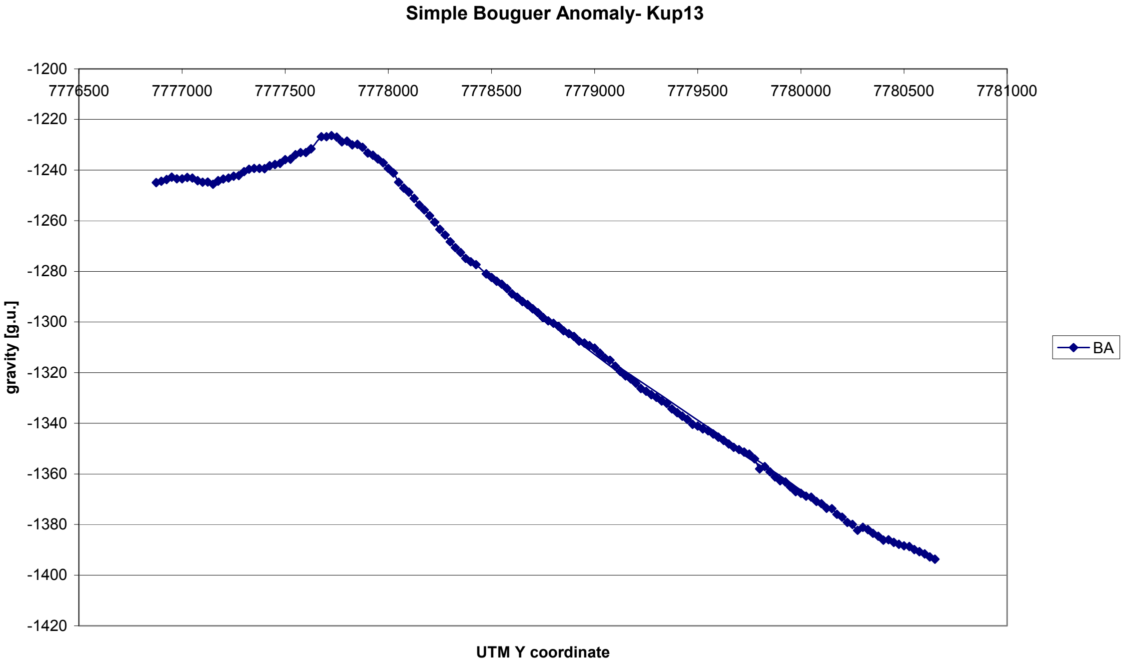

Fig. 2.13 (a) Line Kup13 gravity profile.

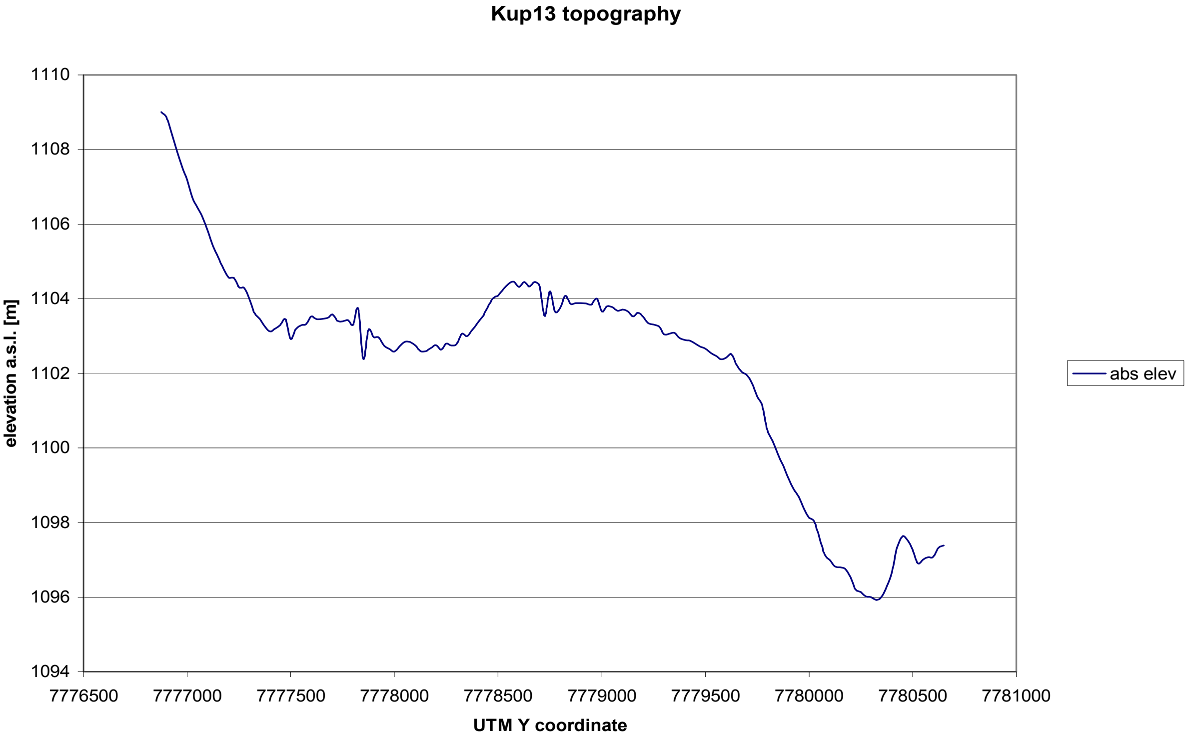

Fig. 2.13 (b) The topography profile of line Kup 13.

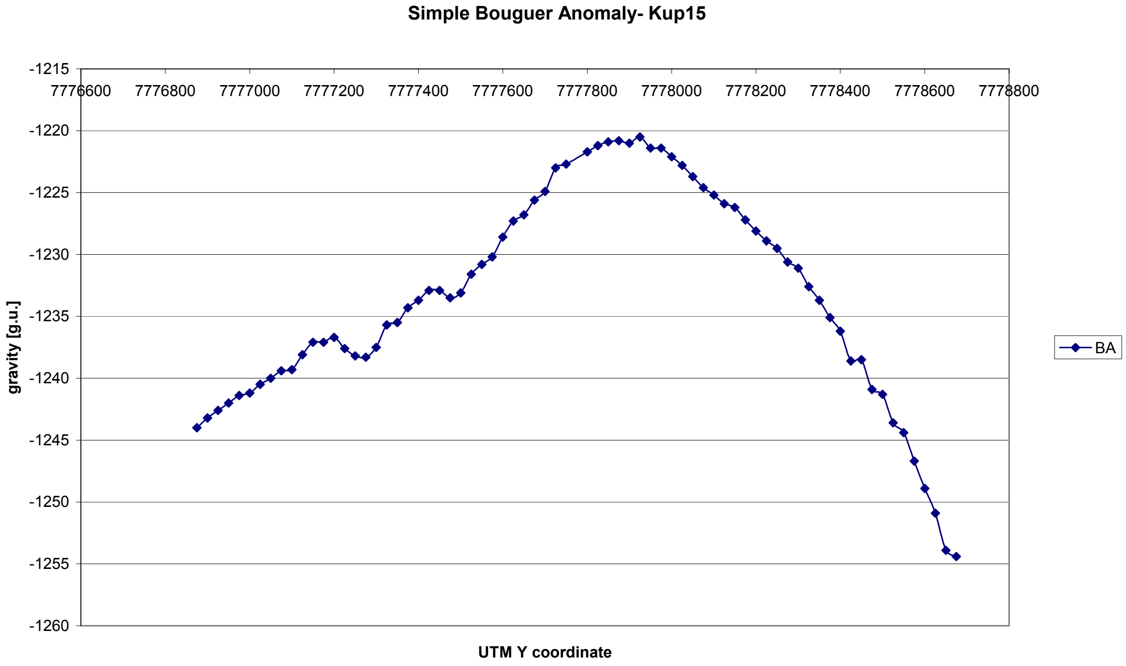

Fig. 2.14 (a) Line Kup15 gravity profile.

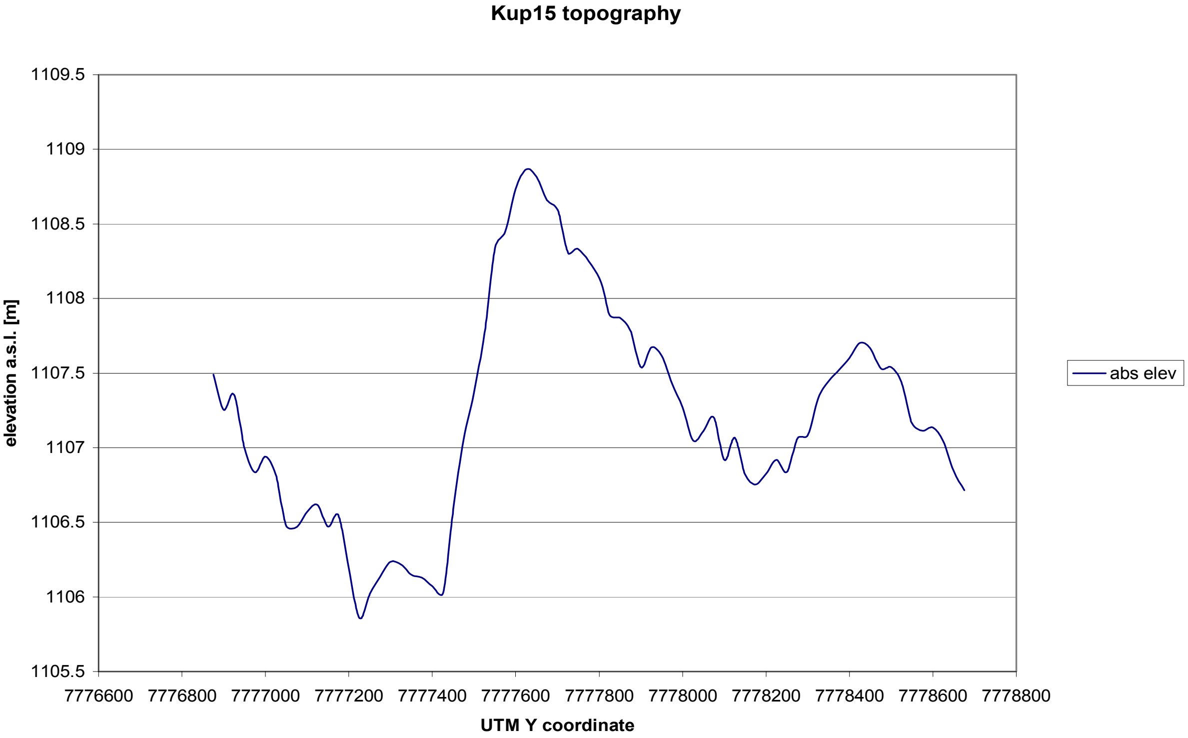

Fig. 2.14 (b) The topography profile of line Kup15.

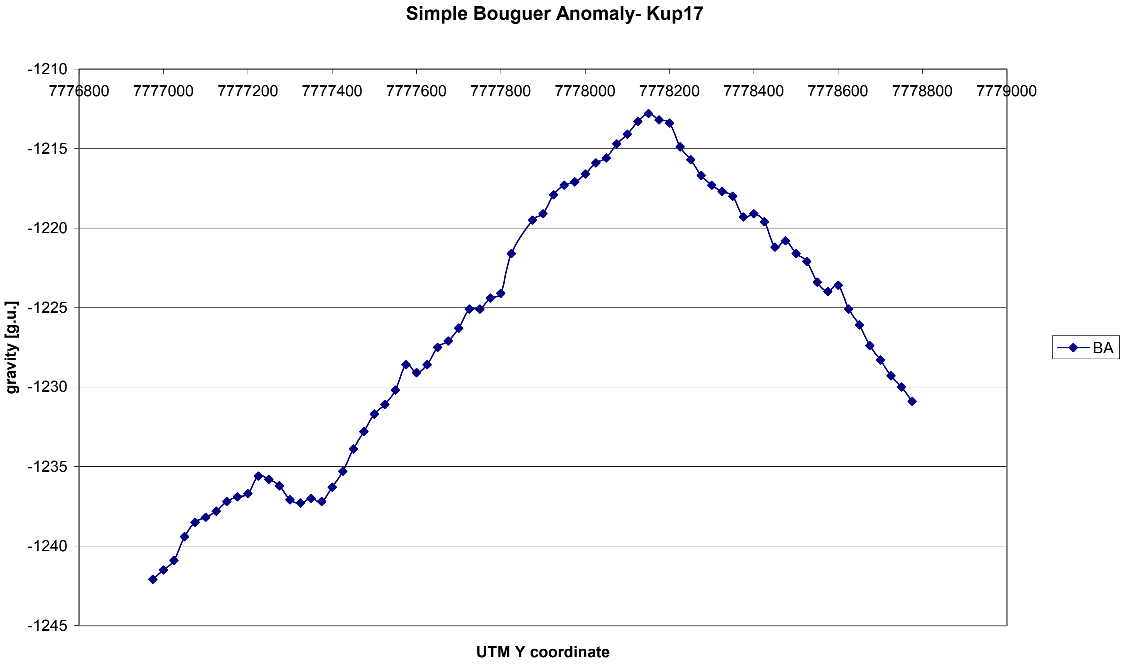

Fig. 2.15 (a) Line Kup17 gravity profile.

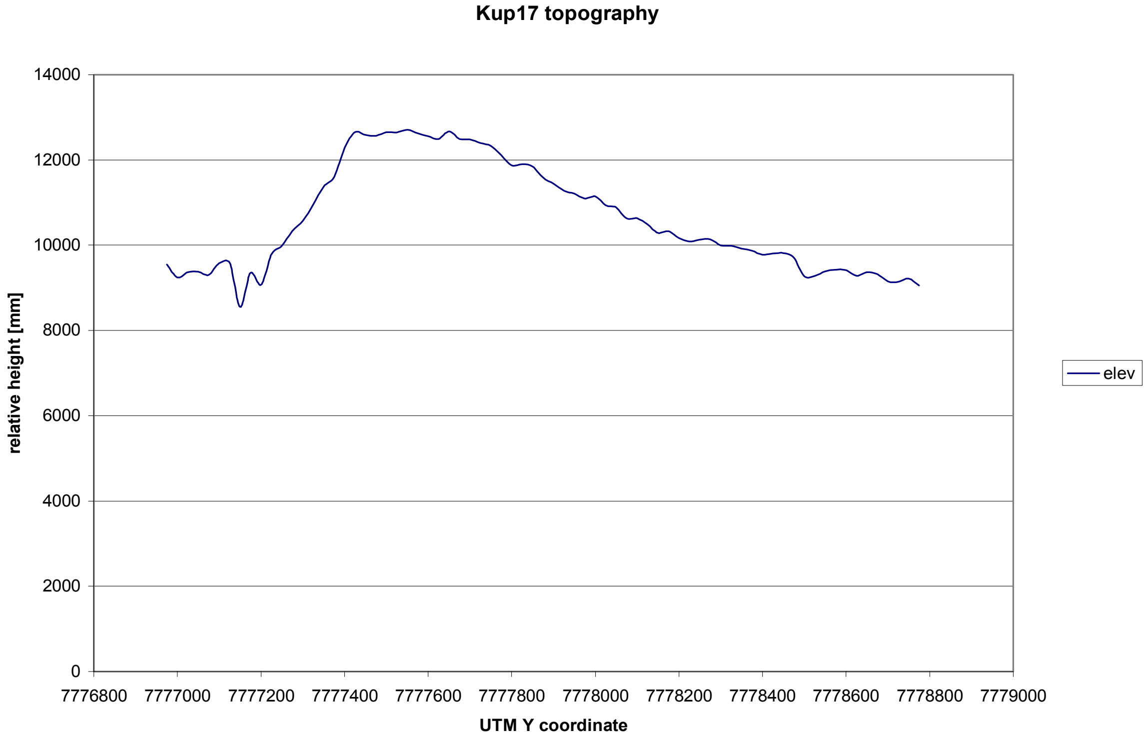

Fig. 2.15 (b) The topography profile of line Kup17.

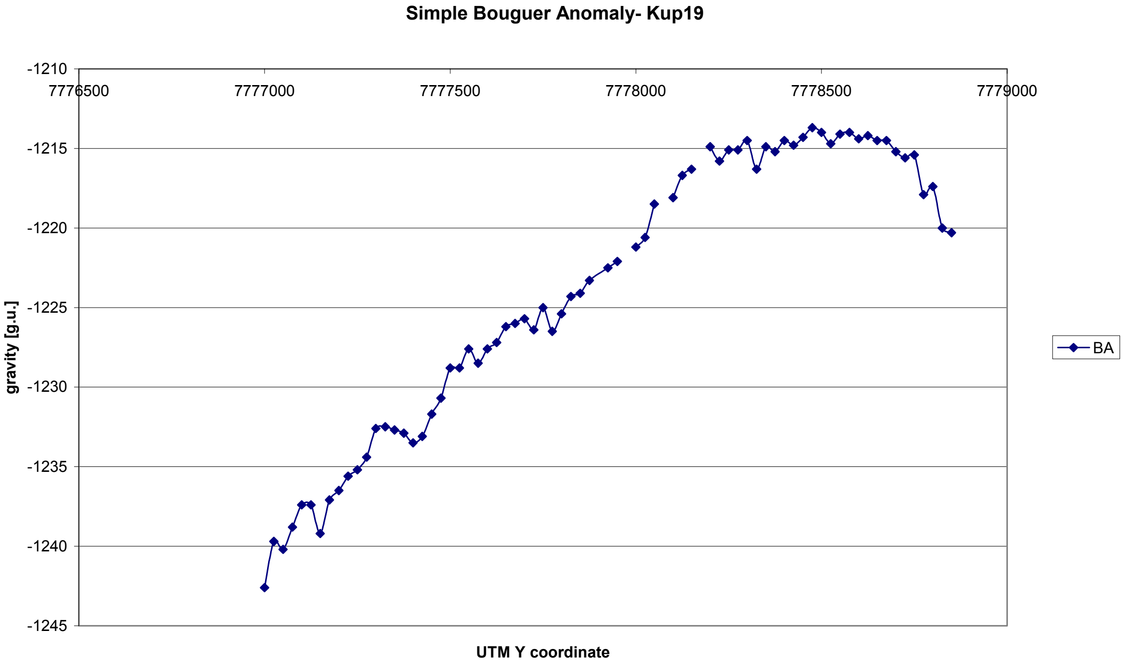

Fig. 2.16 (a) Line Kup19 gravity profile.

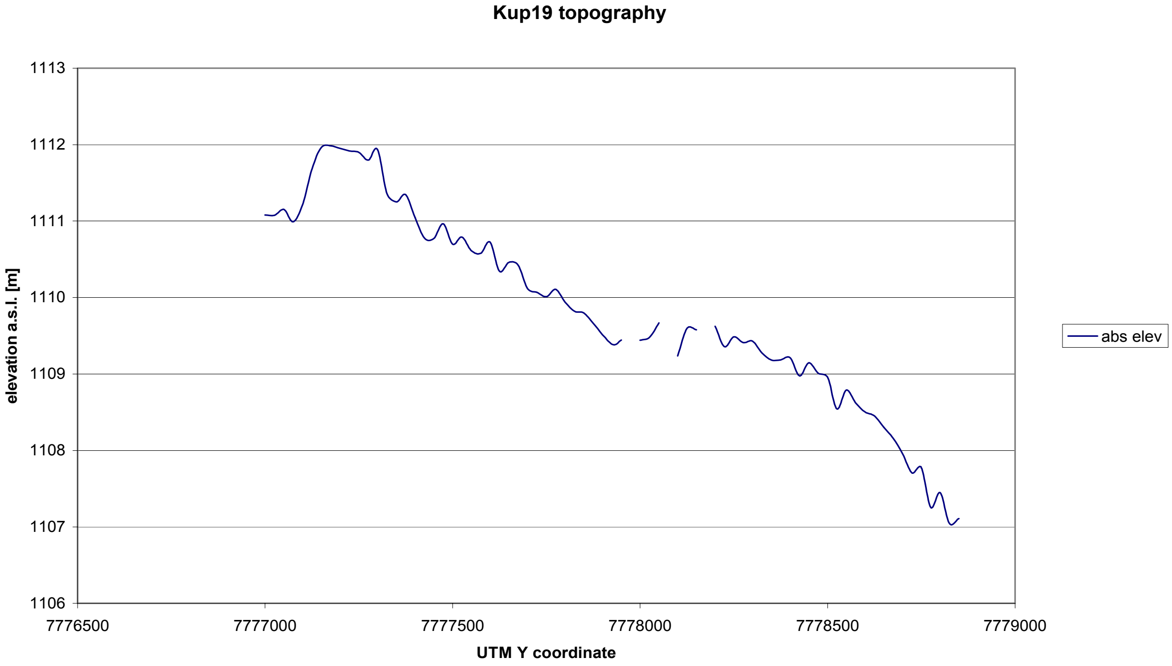

Fig. 2.16 (b) The topography profile of line Kup19.

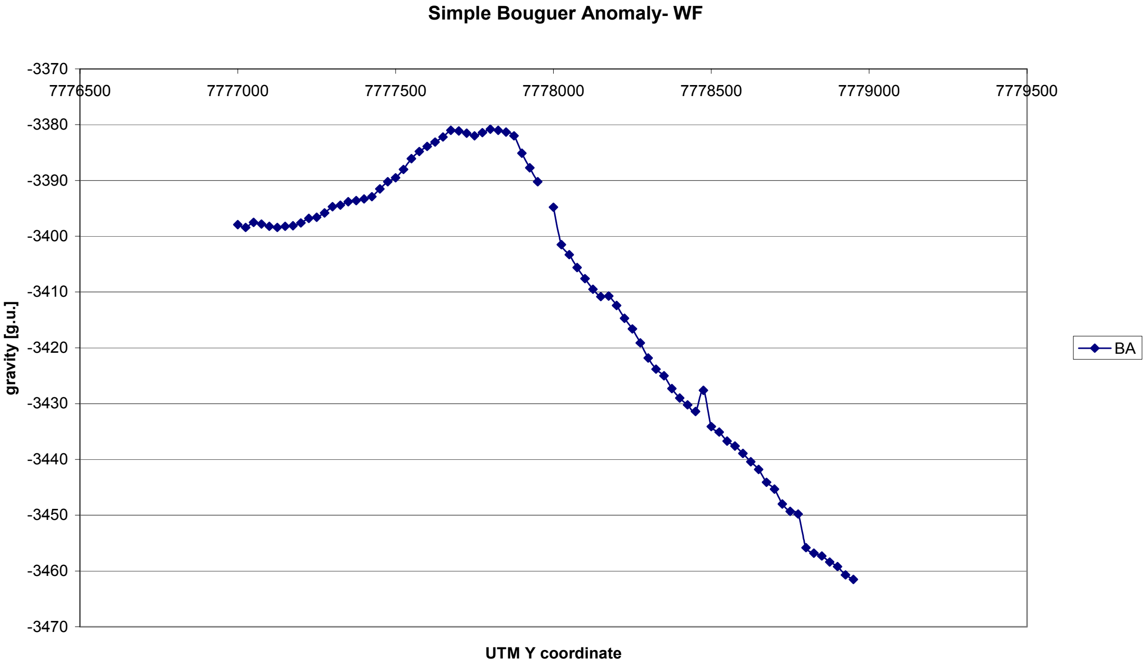

Fig. 2.17 (a) Line WF gravity profile.

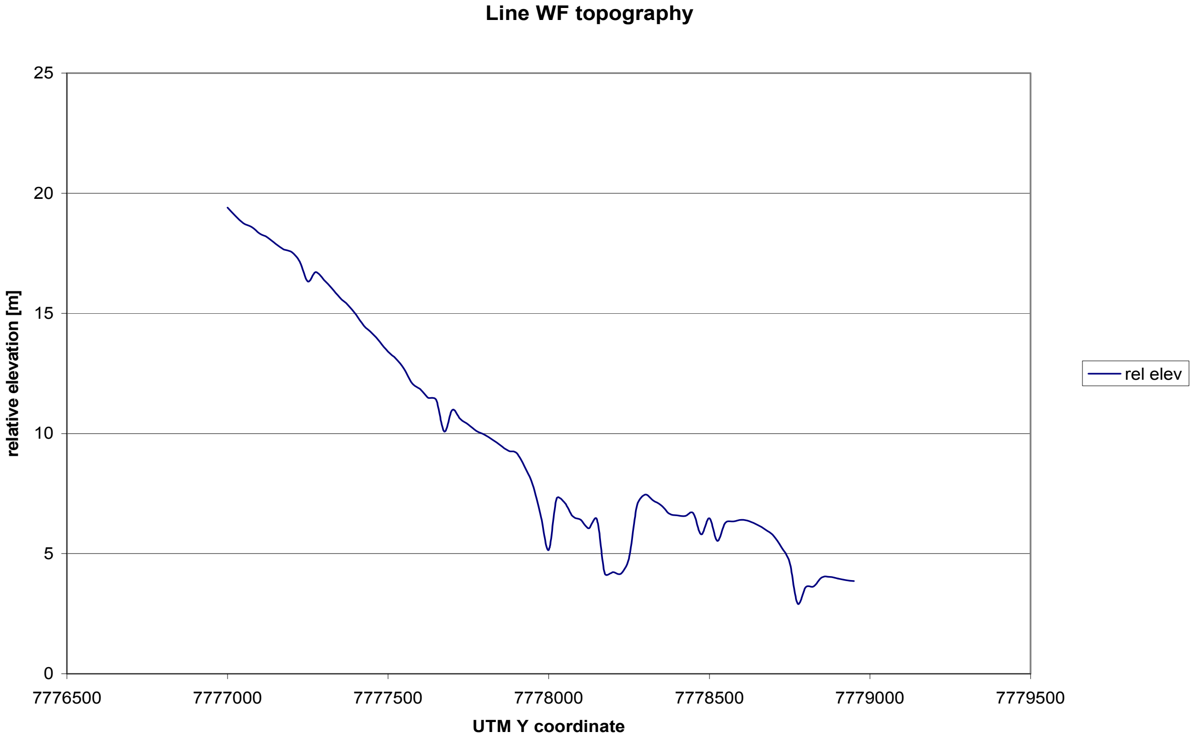

Fig. 2.17 (b) The topographic profile of line WF.

2.8.2.1 Line Kup13 (545900E)

The gravity anomaly curve rises to a local peak of -1242,8 g.u. at UTM (777)6950N and dips to a local low of -1245,6 g.u. at 7150N. It then climbs to the main anomaly at 7750N attaining -1227,0 g.u. which coincides with a wide topographic depression. From this point the gravity values steadily decrease towards the north to a minimum of -1393,7 g.u., defining the regional field which may be fitted as linear. The topography climbs to higher ground after the depression mentioned above before dropping steadily in a northerly direction and crossing a small stream towards the end of the line. The line has an elevation range of about 13 m.

2.8.2.2 Line Kup15 (546500E)

At the first station, 6875N, the gravity is at -1244,0 g.u. and rises steeply to -1236,7 g.u., a localised peak at 7200N. It then dips sharply to a low at 7275N of -1238,3 g.u. This pattern is repeated as the gravity values rise at 7450N; -1232,9 g.u. and 7475N; -1233,5 g.u. The dominant anomalous peak is at 7925N and -1220,5 g.u. The lowest value of -1254,4 g.u. is at the end of the line at 8675N. A parabolic regional trend may be inferred from its shape. The topography drops to a small stream and then rises to higher ground coinciding with the southern flank of the anomaly peak. The depression north of the high ground coincides with the northern flank of the anomaly.

2.8.2.3 Line Kup17 (546900E)

A similar shape to the gravity of Kup15 is observed, although this one is steeper and is more jagged with several small local highs and lows. It starts at its lowest value of -1242,1 g.u. at 6975N rising to the main anomaly peak of -1212,8 g.u. at 8150N. The several smaller peaks occur at 8400, 8475 and 8600N before the line ends at 8775N with a value of -1230,9 g.u. A similar regional to Kup15 may be defined. The topography is gentler than the above lines, rising from a small stream near the beginning of the line to high ground between 7400 and 7800N before descending steadily to the end of the line. There is no apparent correlation between the topography and the residual gravity.

2.8.2.4 Line Kup19 (547300E)

This anomaly is defined by a steadily rising but irregular trend attaining a broader maximum and then dropping off sharply. The gravity values range from -1242,6 g.u. at the beginning (7000N) to a peak of -1213,7 g.u. at 8475N. Another parabolic regional can be fitted. The topography is characterised by a gentle descending slope towards the north.

2.8.2.5 Line WF (545300E)

This line shows a similar shape to Kup13, however, the gravity values are considerably different because the absolute elevation data was not available and so the relative heights from the levelling exercise were used in the gravity reduction. It has a steeper ascent to the anomaly peak and descent into the regional. There is a broad low with a minimum of -3398,4 g.u. at 7125N and it then rises to a double peak of -3381,0 g.u. and -3380,8 g.u. at 7675N and 7800N respectively. The regional low is -3461,5 g.u. at the end of the line. A linear regional can be defined for this profile. The topography descends relatively steeply to the three Chamata river intersections where the river meanders near the end of the line (Fig. 1.2).

2.8.3 Contour map

Fig. 2.18 shows the simple Bouguer anomaly contour map produced by the GEOSOFT Oasis Montaj 43 mapping program for the lines Kup13, 15, 17 and 19.

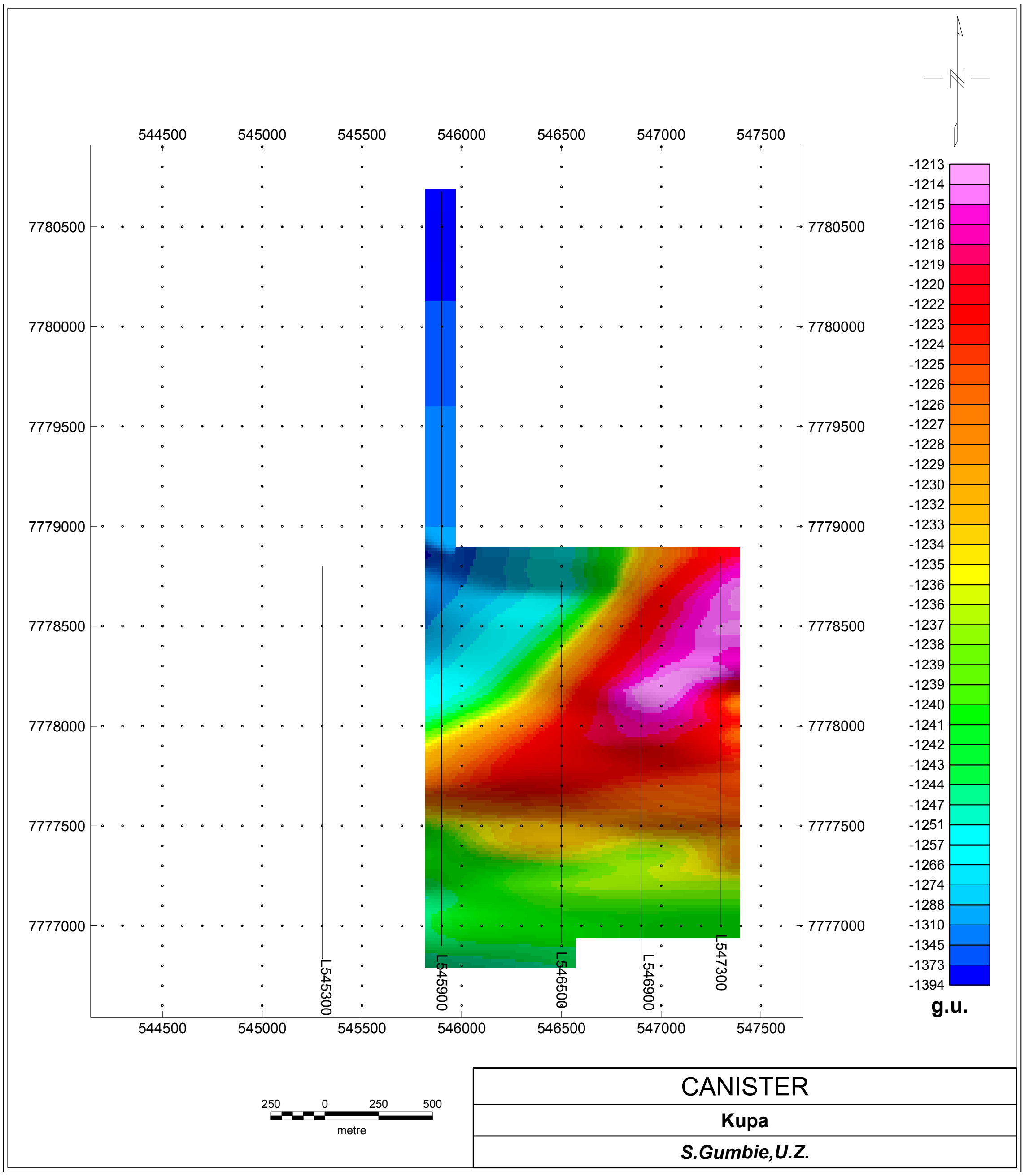

Fig. 2.18 The simple Bouguer anomaly contour map of part the Kupa grid.

The map shows a central gravity high trending NE-SW and tapering towards the western end. At the western tip of the gravity high, the strike becomes E-W with the regional descending in a NW direction. A discussion/interpretation of the gravity survey data is given in section 6.4.

Chapter Three

The Magnetic Method

3.1 Introduction

Magnetic prospecting is the oldest method of geophysical prospecting with measurements of variations in the Earth's magnetic field being made in Sweden to locate iron ore deposits as early as 1640 (Parasnis, 1986). The physical background of the magnetic method is similar to that of the gravitational technique since both are potential field methods. However, the gravity field is simpler since it depends on the density, a scalar quantity, whereas the magnetic field is complex because it depends on the magnetisation of rocks which is a vector quantity.

The aim of a magnetic survey is to investigate subsurface geology on the basis of anomalies resulting from the magnetic properties of the underlying rocks. Although most rock-forming minerals are effectively non-magnetic, certain rock types contain sufficient magnetic minerals to produce significant magnetic anomalies. The magnetic properties of rocks may differ by several orders of magnitude and the anomalies are large relative to the main field. This method can be used to delineate faults, lithological contacts and the structure of subsurface basement crystalline rocks below non-magnetic sediments to assist in geological mapping. The detection of metalliferous mineral ore lodes is of particular interest here. Due to the speed and economy of airborne reconnaissance surveys, the magnetic method is by far the most widely used geophysical method.

3.2 Basic concepts

Within the vicinity of a bar magnet a magnetic flux is developed which flows from one end of the magnet to the other (Fig. 3.1).

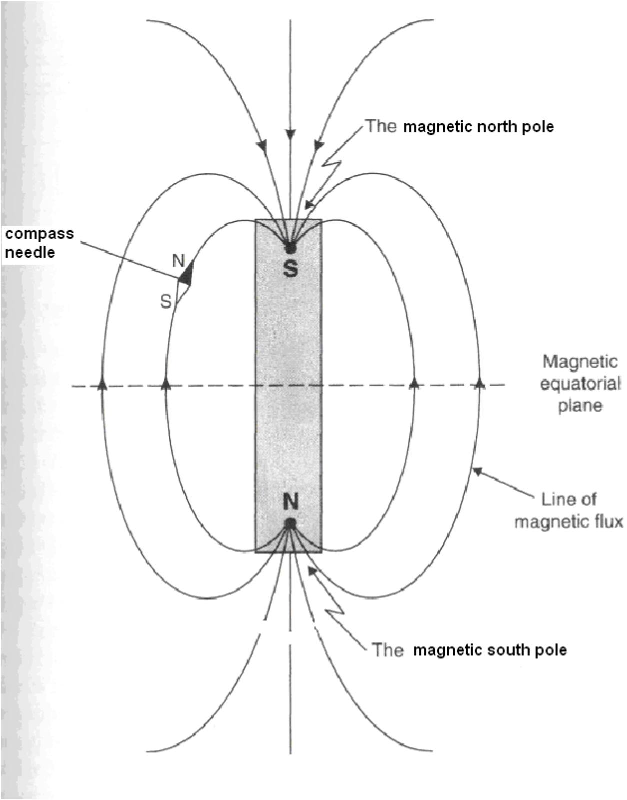

Fig. 3.1 Lines of magnetic flux around a bar magnet (Reynolds, 1997).

This flux can be mapped from the directions assumed by a small compass needle suspended within it. The points within the magnet where the flux converges are known as the poles of the magnet. A freely-suspended bar magnet similarly aligns with the flux of the Earth's magnetic field in a N-S direction.

The force **F** between two magnetic poles of strengths p_1 and p_2 in a medium of magnetic permeability μ separated by a distance *r* is given by

$$\mathbf{F} = \frac{p_1 p_2}{4\pi\mu r^2}\hat{r} \quad \text{(Reynolds, 1997)} \quad \ldots\ldots\ldots\ldots\ldots\ldots\ldots\ldots \quad (3.1)$$

where $\mu = \mu_0 \mu_r$, $\mu_0 = 4\pi \times 10^{-7}$ H m^{-1} is the permeability of free space and μ_r is the relative permeability of the medium. The force is attractive for unlike poles and repulsive for like poles. The magnetic field or flux density **B** of a pole of strength *p* at a distance *r* away is given by:

$$\mathbf{B} = \frac{p}{4\pi\mu r^2}\hat{r} \quad \text{……………………………………………..} \quad (3.2)$$

The magnetic scalar potential V is

$$\mathrm{V} = \frac{p}{4\pi\mu r} \quad \text{……………………………………………} \quad (3.3) \text{ and}$$

Hence $$\mathbf{B} = -\nabla V \quad \text{……………………………………………} \quad (3.4)$$

The magnetic field strength **H** is defined by

$$\mathbf{B} = \mu\,\mathbf{H} \quad \text{……………………………………………} \quad (3.5)$$

and susceptibility κ by:

$$\kappa = \mu_r - 1 \quad \text{……………………………………………...} \quad (3.6)$$

Combining equations (3.4) and (3.5) leads to

$$\mathbf{J} = \mu_0\,\kappa\,\mathbf{H} \quad \text{……………………………………………..} \quad (3.7)$$

which is the definition of the intensity of magnetisation, **J**.

The flux density is measured in webers per square metre [Wb/m^2] also called the tesla [T]. For geophysical work in the Earth's magnetic field, the nanotesla is used instead, with $1\mathrm{nT} \equiv 1\gamma$; $\gamma = 10^{-5}$ gauss in c.g.s. units. The magnetic permeability is measured in henrys per metre [H/m].

3.3 The Earth's magnetic field

3.3.1 Introduction

Magnetic anomalies caused by rocks are localised effects superimposed on the normal magnetic field of the Earth (the geomagnetic field). Consequently, knowledge of the geomagnetic field is necessary in both the reduction of magnetic data to a suitable datum and in the interpretation of the resulting anomalies. The geomagnetic field is geometrically more complex than the gravity field of the Earth and exhibits irregular variation in both orientation and magnitude with latitude, longitude and time.

3.3.2 Origin of the main field

Many theories have been proposed for the origin of the main field, e.g. Parker (1955) in a text by Jacobs (1987). However, none are fully comprehensive as any model must account for a fairly stable field with secular variations (~ 1000 years) and field reversals over geological time (~ 10^6 years) (Parkinson, 1983). The most successful theories involve magnetohydrodynamics. This involves multiple convection cells constituting electric currents in a spinning shell of liquid nickel-iron alloy at great temperatures and pressures. The significance of the main field is that it controls all other fields directly or indirectly, contributing ~ 99% of the field as measured at the Earth's surface. Almost 90% can be represented by the field of a theoretical dipole at the centre of the Earth and inclined at ~ 11,0º to the axis of rotation (Kearey and Brooks, 1988).

3.3.3 Elements of the geomagnetic field

There are seven interrelated magnetic elements (Fig. 3.2).

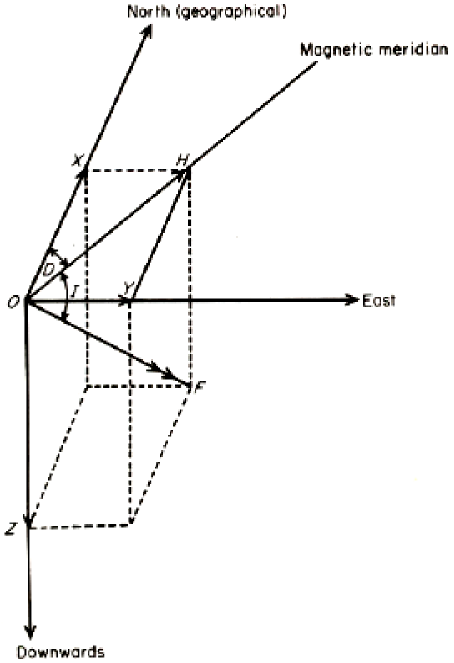

Fig. 3.2 The main elements of the geomagnetic field (from Merrill and McElhinny, 1983).

These are:

B, T or **F**- the total magnetic field vector
D- declination, horizontal angle between angle between geographic and magnetic north;
I- inclination, the dip of **B**;
Z- vertical component of **B**;
X- horizontal component of **B** in the direction of true N;
Y- horizontal component of **B** due E;
H- horizontal component of **B**, defining the direction of magnetic north.

Some relationships between the elements:

$$\begin{array}{ll} B^2 = H^2 + Z^2 = X^2 + Y^2 + Z^2 & \} \\ X = H\cos D & \} \\ Y = H\sin D & \} \qquad \ldots\ldots\ldots\ldots\ldots\ldots\ldots\ldots \quad (3.8) \\ Z = B\sin I & \} \\ \tan D = Y/X,\ \ \tan I = Z/H & \} \end{array}$$

The magnitude of the geomagnetic field typically ranges from 25 000 nT to 70 000 nT with $B_e \approx 30\ 000$ nT (magnetic equator) and $B_p \approx 60\ 000$ nT (magnetic poles). In Zimbabwe (1995) from N to S the ranges of B, D and I are listed below:

B [nT]	D	I	
31 500	7°W	-59,5 $^\circ$	
30 000	12°W	-63,5 $^\circ$	(Podmore, pers. comm., 2006).

3.3.4 The International Geomagnetic Reference Field (IGRF)

The IGRF is a best fit model to the geomagnetic field expressed as a set of spherical harmonic coefficients and their time rates of change. The global field is mapped regularly, typically every 5 years, to monitor secular variations by land measurements at observatories and magnetic base stations combined with satellite magnetometer surveys, e.g. MAGSAT (Reynolds, 1997). Each year that the IGRF coefficients are specified is called an epoch.

The global field must satisfy Laplace's equation in regions free of sources;

$$\nabla^2 V = 0. \quad \text{(3.9)}$$

Assuming a spherical Earth of radius a, the geomagnetic potential due to internal sources alone is:

$$V(r,\theta,\phi) = a\sum_{n=1}^{\infty}\sum_{m=0}^{n}\left(\frac{a}{r}\right)^{n+1}\left(g_n^m \cos m\phi + h_n^m \sin m\phi\right)P_n^m(\cos\theta) \quad \text{(3.10)}$$

where $0 < m \leq n$; r is the radial distance from the centre of the Earth; θ is the colatitude; ϕ is the longitude; $P_n^m(\cos\theta)$ is the associated Legendre function of degree n and order m (Schmidt quasi-normalised); g_n^m and h_n^m are the spherical harmonic coefficients in nT (Peddie, 1982). From equation (3.4), the components of **B** on a spherical Earth are:

$$B_x = -B_\theta = \frac{1}{r}\frac{\partial V}{\partial \theta} \quad \text{(north)} \quad \text{(3.11)}$$

$$B_y = B_\phi = -\frac{1}{r\sin\theta}\frac{\partial V}{\partial \phi} \quad \text{(east)} \quad \text{(3.12)}$$

$$B_z = -B_r = \frac{\partial V}{\partial r} \quad \text{(down)} \quad \text{(3.13)}$$

Substituting eqn. 3.10 with the $P_n^m(\cos\theta)$ polynomials given in tables and comparing with the potential expression

$$V = \frac{\mu_0 \vec{m}.\hat{r}}{4\pi r^2} \quad \text{(3.14)}$$

for a dipole centred at the origin, where **m** is the dipole moment; it can be shown that the term n = 1 describes the magnetic field of a dipole centred at the origin (Blakely, 1996). Depending on the epoch used, the field produced by the "best" geocentric dipole is called the dipole field (Fig. 3.3).

The IGRF represents the regional magnetic trend which should be removed from the magnetic survey readings to isolate variations due to local near surface geology. IGRF maps for 2005.0 are available on website http://swdcdb.kyoto_u.ac.jp/igrf (Podmore, pers. comm., 2006).

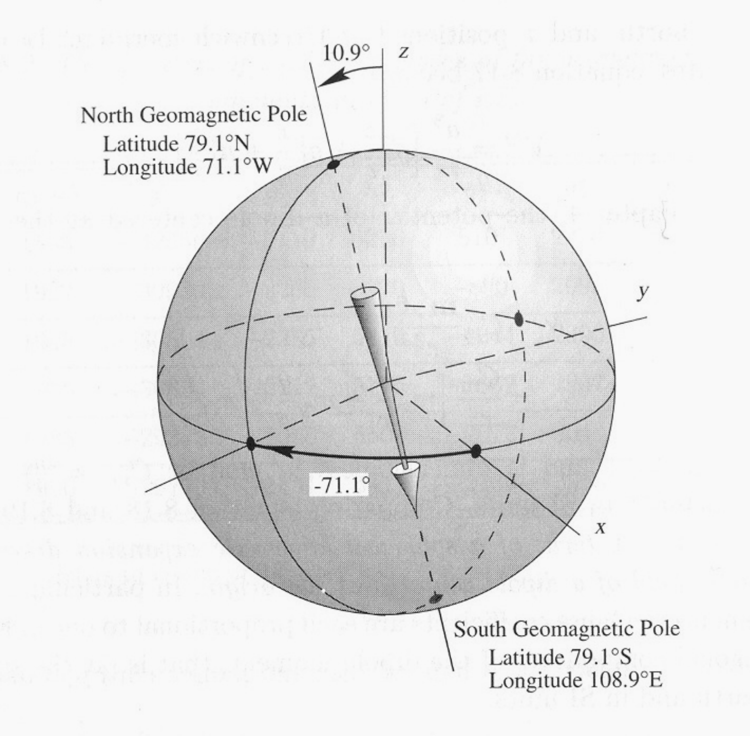

Fig. 3.3 The IGRF 1990 geocentric dipole (after Blakely, 1996).

3.3.5 The external magnetic field

Magnetic effects of external origin cause the Earth's field to vary on a daily basis to produce diurnal variations. Under normal conditions (Q or quiet days) the diurnal variation is smooth and regular and has an amplitude of about 20 - 80 nT, being at a maximum in polar regions. This variation is due to the magnetic field induced by the flow of charged particles within the ionosphere towards the magnetic poles, as both the circulation patterns and diurnal variations vary in relation to the tidal effects of the Sun and Moon (Kearey and Brooks, 1988). The seasons and the latitude also affect the diurnal drift (Fig. 3.4).

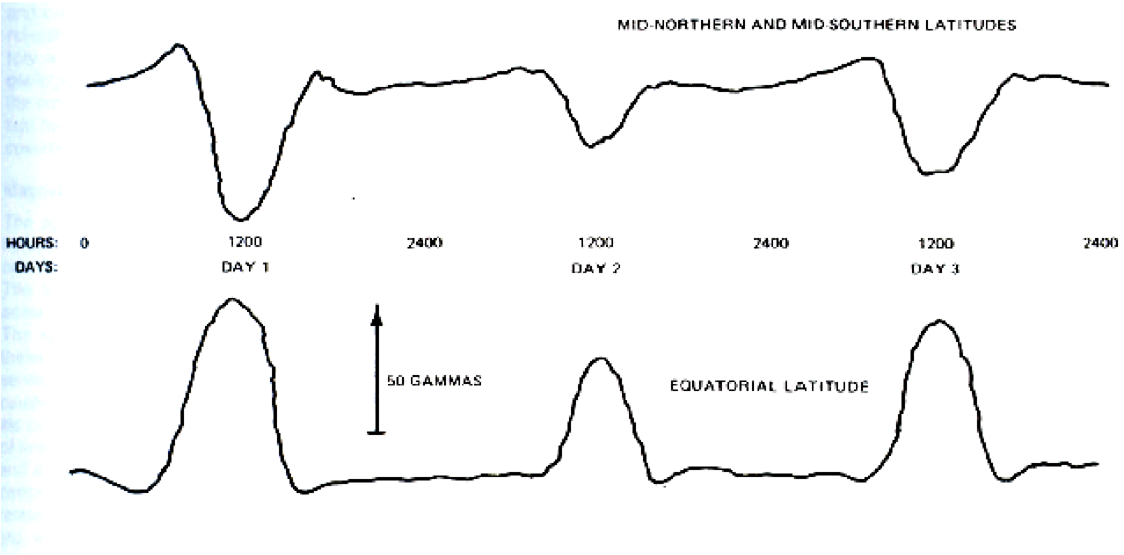

Fig. 3.4 Typical diurnal field variations in the total field intensity (Breiner, 1973).

Some days (D or disturbed days) are distinguished by large, short term erratic disturbances in the geomagnetic field, with amplitudes of up to 1000 nT known as magnetic storms. These are usually associated with intense solar activity and result from the arrival in the ionosphere of charged particles. Magnetic surveying should be discontinued during such storms since it is impossible to correct the rapid, high-amplitude changes in the magnetic field data (Fig. 3.5).

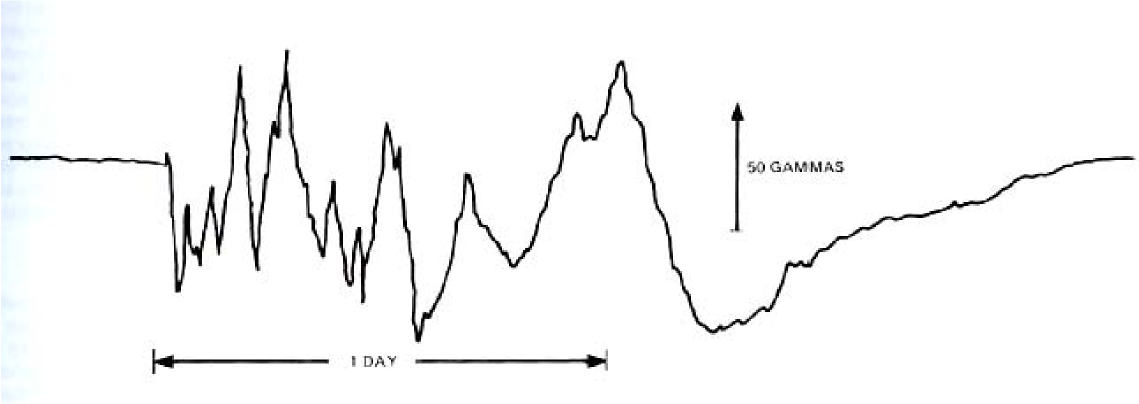

Fig. 3.5 Typical magnetic storm (Breiner, 1973).

3.3.6 Rock magnetism

The magnetic method depends upon measuring accurately the anomalies of the local geomagnetic field produced by the variations in the intensity of magnetisation in the subsurface rock formations. The magnetisation of rocks is partly due to induction by the Earth's magnetic field and partly to their remanent magnetisation. The induced intensity depends primarily upon the magnetic susceptibility as well as the magnetizing field, and the remanent intensity upon the mineralogy, composition and geological history of the rock.

3.3.6.1 Induced magnetisation

All substances are magnetic at an atomic scale and may be classified as diamagnetic and paramagnetic. In special cases where the field is very low (< 1 mT) ferromagnetic materials can exhibit induced magnetisation (Collinson, 1983). Ferromagnetic materials can be further subdivided into truly ferromagnetic, antiferromagnetic and ferrimagnetic (Fig. 3.6).

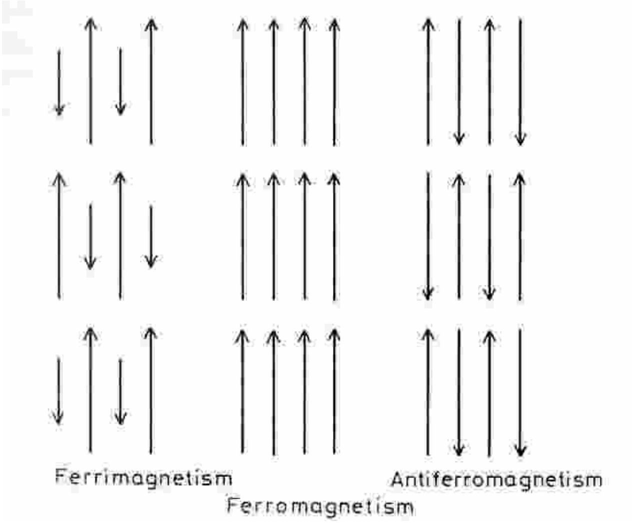

Fig. 3.6 Dipole alignment in ferrimagnetic, ferromagnetic and antiferromagnetic domains (Kearey and Brooks, 1988).

Quantum theory can account for these phenomena on a sub-atomic level. Basically, the orientation of the magnetic dipoles of the atoms gives rise to the various magnetisation states.

3.3.6.2 Remanent magnetisation

The inherited magnetisation remaining after the removal of the applied field is known as remanent magnetisation. Several types exist, namely:

- Thermoremanent magnetisation (TRM)- primary remanent magnetisation acquired by magnetic minerals of igneous rocks on cooling below their Curie temperature;
- Detrital remanent magnetisation (DRM)- alignment of magnetic particles of a sediment as they settle in the Earth's field;
- Chemical remanent magnetisation (CRM)- secondary remanence as magnetic minerals recrystallize during diagenesis or metamorphism;
- Viscous remanent magnetisation (VRM) - may develop slowly in a rock *in situ* in the ambient magnetic field.

3.3.6.3 Susceptibility of rocks

The susceptibility of rocks is almost entirely controlled by the amount of ferrimagnetic minerals in them. Their grain size, mode of distribution and shape are extremely variable. Magnetite is by far the most common magnetic mineral and it is reasonable to classify the magnetic behaviour of rocks according to their overall magnetite content. Basic igneous rocks such as basalts, dolerites and serpentinites are usually highly magnetic with the proportion of magnetite decreasing with increasing acidity. Sediments and acid igneous rocks have small susceptibilities, Fig. 3.7.

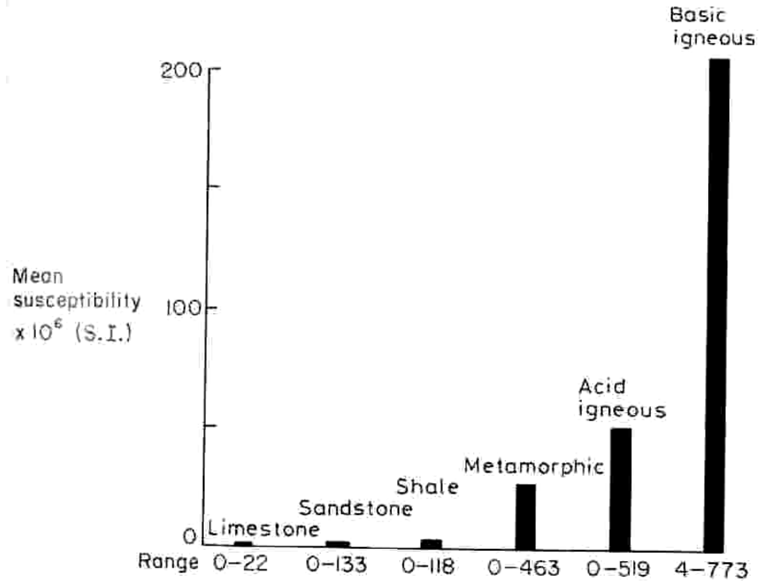

Fig. 3.7 Histogram showing mean values and ranges in susceptibility of common rock types (Kearey and Brooks, 1988).

3.4 Anomalies

All magnetic anomalies caused by rocks are superimposed on the geomagnetic field. The induced magnetization of a subsurface rock unit combined with any remanent magnetization produces a magnetic flux density around the body which combines vectorially with the geomagnetic field at the point of observation to give a resultant magnetic field. The shape of a magnetic anomaly varies dramatically with the dip of the Earth's field, as well as with the shape and strike of the source body and its direction of magnetization.

The normal geomagnetic field can be described by a vector diagram (see Fig. 3.8a) and the geomagnetic elements are related by equation (3.8).

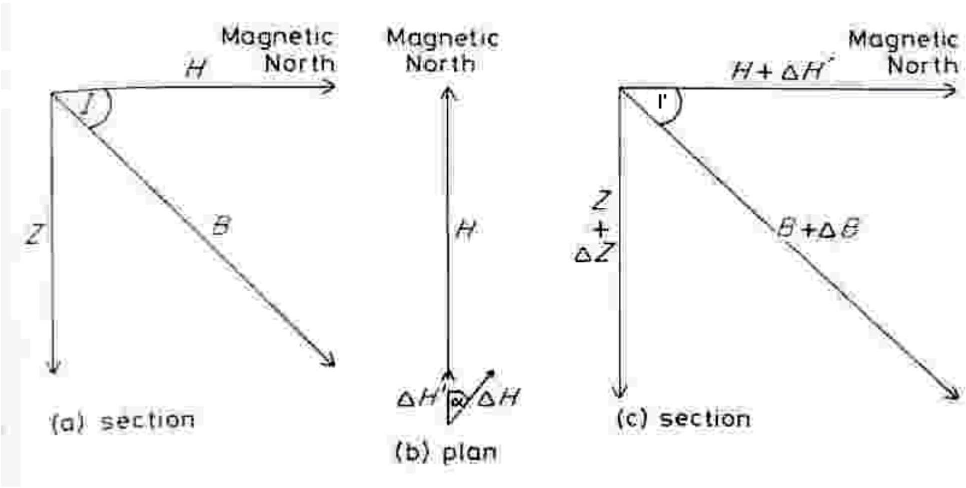

Fig. 3.8 Simplified vector representation of the geomagnetic field without (a) and with (c) a superimposed magnetic anomaly.

A magnetic anomaly superimposed on the Earth's field causing a change ΔB in the strength of the total vector **B** is shown in Fig. 3.8(c). Let the anomaly produce a vertical component ΔZ and a horizontal component ΔH at an angle α to H (Fig. 3.8b). Only $\Delta H'$ contributes to the anomaly:

$$\Delta H' = \Delta H \cos\alpha \quad \text{………………………………} \quad (3.15)$$

Using a similar vector diagram to include the anomaly (Fig. 3.8c), its magnitude, if higher terms in Δ are ignored, reduces to

$$\Delta B = \Delta Z(Z/B) + \Delta H'(H/B) \quad \text{……………………} \quad (3.16)$$

Substituting equation (3.15) and the angular relations of the geomagnetic elements from equation (3.8) gives

$$\Delta B = \Delta Z \sin I' + \Delta H \cos I' \cos\alpha \quad \text{……………….} \quad (3.17)$$

(Kearey and Brooks, 1988).

3.5 Field procedures

3.5.1 Instrumentation

Two GEOMETRICS G-856 Memory-Mag Proton Precession Magnetometers (PPM) (Fig. 3.9) were used in the magnetic survey.

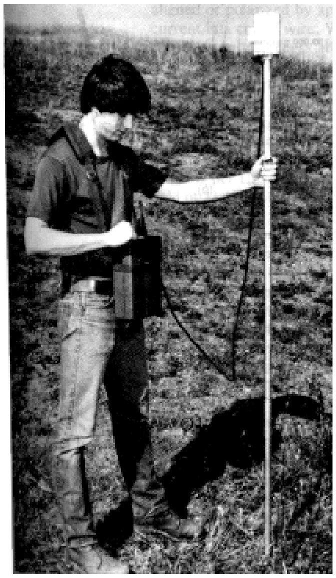

Fig. 3.9 Portable proton precession magnetometer (Dobrin and Savit, 1988). The sensor is mounted on an aluminium pole of about 2 m long.

The principle of operation is that a PPM makes use of the small magnetic moment of the hydrogen nucleus (proton). The sensing element consists of a bottle with a low freezing-point hydrocarbon fluid, about which is wound a coil of copper wire. A current of the order of an ampere or more is passed through the coil creating a strong axial magnetic field along which the proton moments are aligned. When the current is switched off, the protons try to re-align in the direction of the external field, precessing about the field direction. The precession frequency, f, is proportional to the field strength;

$$B = \frac{2\pi f}{\gamma_p}, \quad \ldots\ldots\ldots\ldots\ldots\ldots\ldots\ldots\ldots\ldots\ldots\ldots \quad (3.18)$$

where γ_p = 2,675197 x 10^8 T^{-1} s^{-1} is the gyromagnetic ratio of the proton and f the frequency of this precession which can be measured very accurately by phase-sensitive circuitry. Consequently, the accuracy of modern PPMs is 1,0 - 0,1 nT (Milsom, 1989).

The G-856 is a portable, man-carried magnetometer/gradiometer and “base station” magnetometer. It features simple, push button operation and a built-in digital memory which stores over 5000 readings which eliminates transcription errors and allows the use of a computer to automatically record and process the data from the magnetic survey. The G-856 Memory-Mag will also record automatically at regular intervals, so it can be left unattended to monitor diurnal changes. These readings (up to 12 500) are used to correct simultaneous field measurements for high accuracy surveys by using an identical G-856 as the roving magnetometer. The time-of-day is recorded with each reading by a built-in digital clock (Geometrics Operation Manual, undated).

3.5.2 Magnetic survey

The magnetic survey was executed by Canister’s geophysical technician, Mr. Stephen Ndlovu and an assistant. The general procedure was as follows:

- The operator was “de-magnetized”- all sources of magnetic noise removed, e.g. watch, compass, pen knife, keys, geological hammer;
- magnetometers checked for sensor fluid and range tuned for the survey area;
- check readings of the two magnetometers at the same place and time. A difference of 1 - 2 nT is tolerable with modern equipment;
- base station magnetometer set up in a magnetically “quiet” region, i.e. low magnetic gradients, and an assistant placed to guard against disturbances, e.g. livestock and people;
- repeated readings taken at each station to monitor gradients, ± 1 nT deviation acceptable;
- battery levels carefully monitored during survey for proper functioning of continuous measuring instrument; and

- field notes made of relevant topographical or geological features and suspected magnetic sources (cultural effects).

The Kupa grid was surveyed at a 12,5 m station spacing along 15 of the total 17 lines. The operator employed a “zigzag” pattern by going from the last peg of the current line to the last peg of the next line to save from walking back to the beginning of each line. Care was taken to assign the right values to the right pegs when changing lines.

The diurnal variation corrections done were similar to gravity drift corrections but with PPMs there is no instrument drift. One base station was sufficient for the small survey area of a few square kilometres.

3.6 Presentation of results

3.6.1 Total magnetic field profiles

The diurnal variations for the duration of the survey are presented using the Julian calendar in Figs. 3.10 - 3.13. The diurnal variations were typical of quiet days with a maximum amplitude attained of about 30 nT. From the magnetic readings (Appendix A3), the corrected magnetic profiles are displayed in Figs. 3.14 – 3.28 and show the characteristic bipolar nature of most magnetic anomalies with dominant positive anomalies from linear regional trends. The magnetic curves generally display simple shapes except Figs. 3.21 and 3.22 which show double peaks. Figs. 3.14 and 3.26 - 28 are more complicated but still reveal the more dominant positive anomalies. From the east of the grid, the profiles show a rise from the beginning of the line to the dominant peak and then fall to a regional minimum before rising gradually again to the trend line. From line 544950 going west, however, the profiles start with high magnetic values. The range of the magnetic field strength measured on the profiles is from 29 800 nT to 32 000 nT with line 546500 having the greatest amplitude. Five of the profiles, selected on the basis of their different shapes, are described below in a normal sequence from west to east.

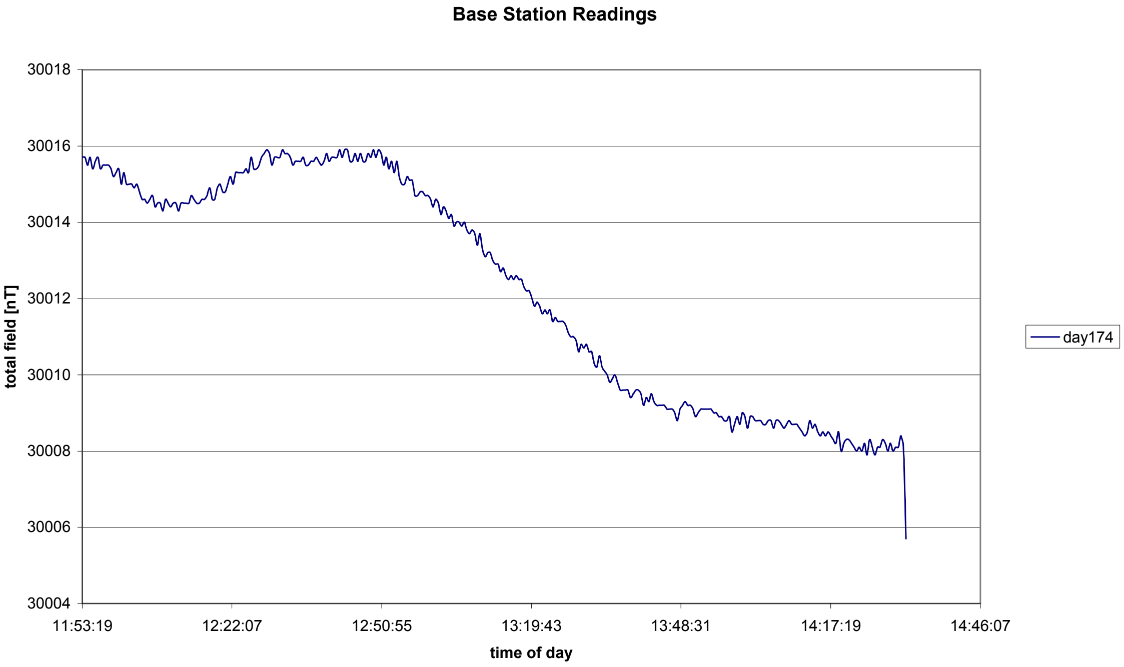

Fig. 3.10 Base station readings for day 174.

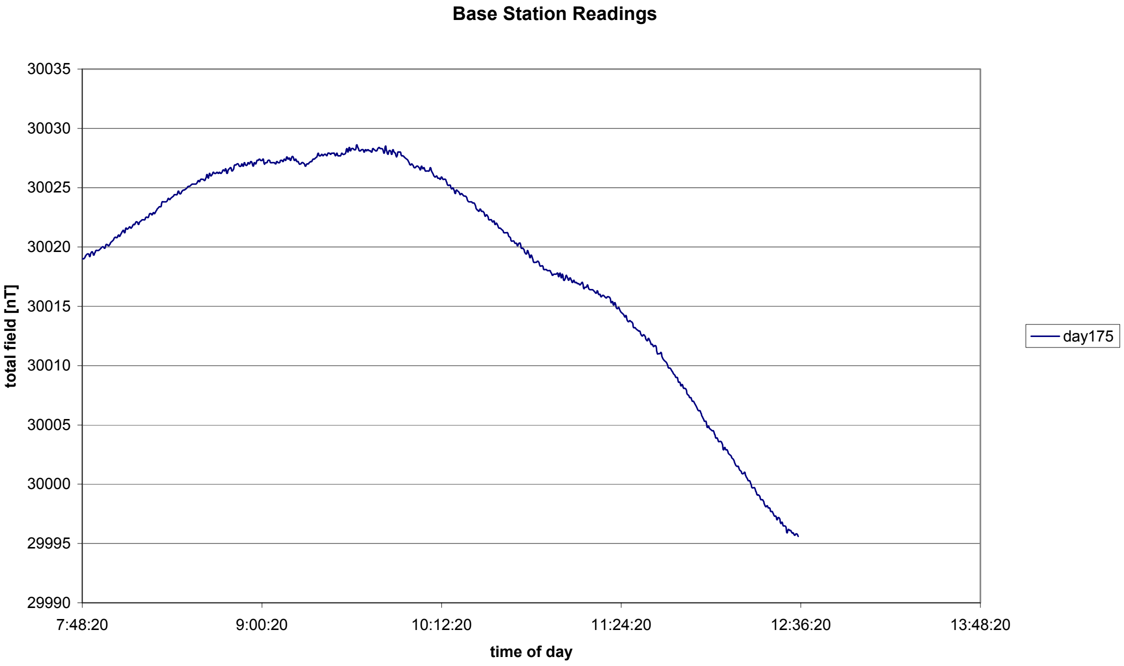

Fig. 3.11 Base station readings for day 175.

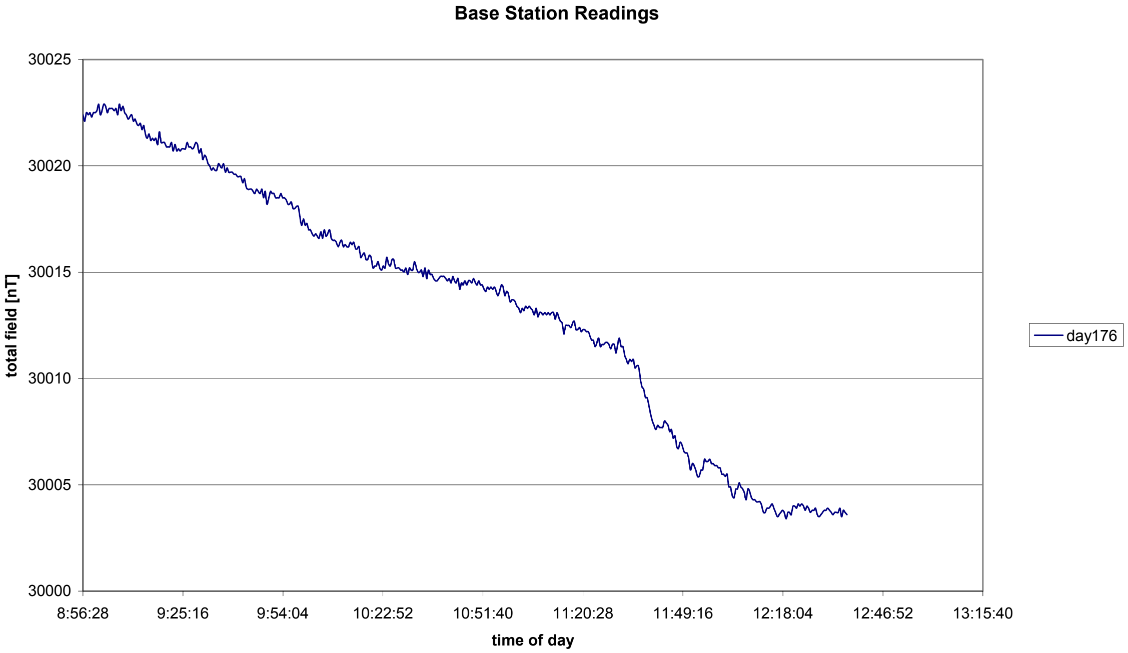

Fig. 3.12 Base station readings for day 176.

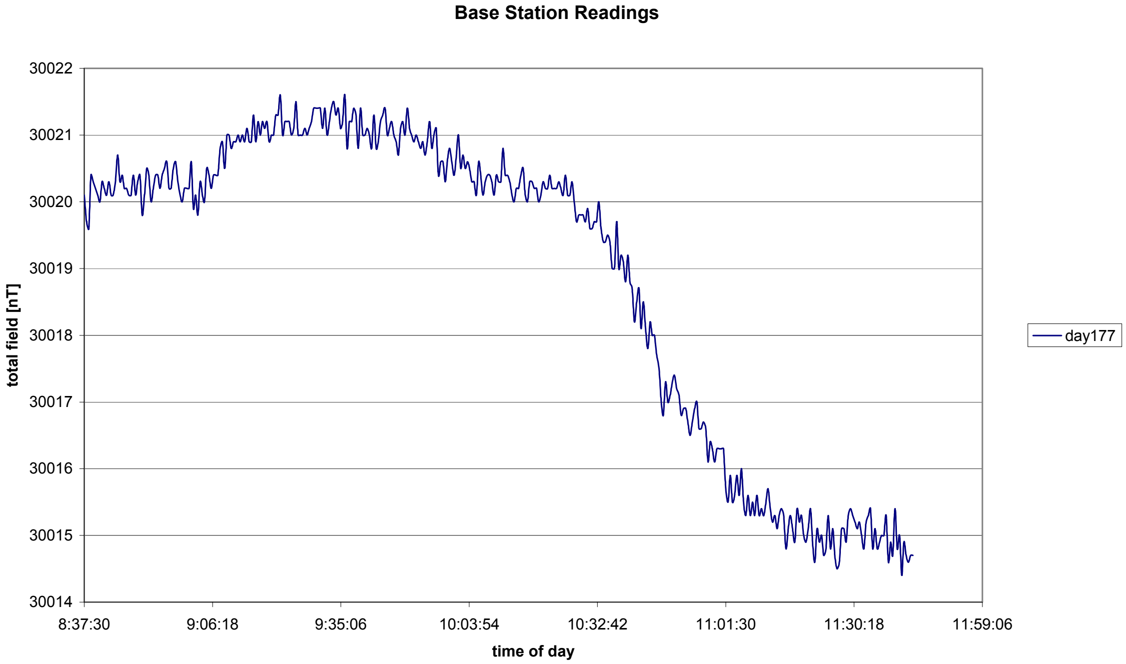

Fig. 3.13 Base station readings for day 177.

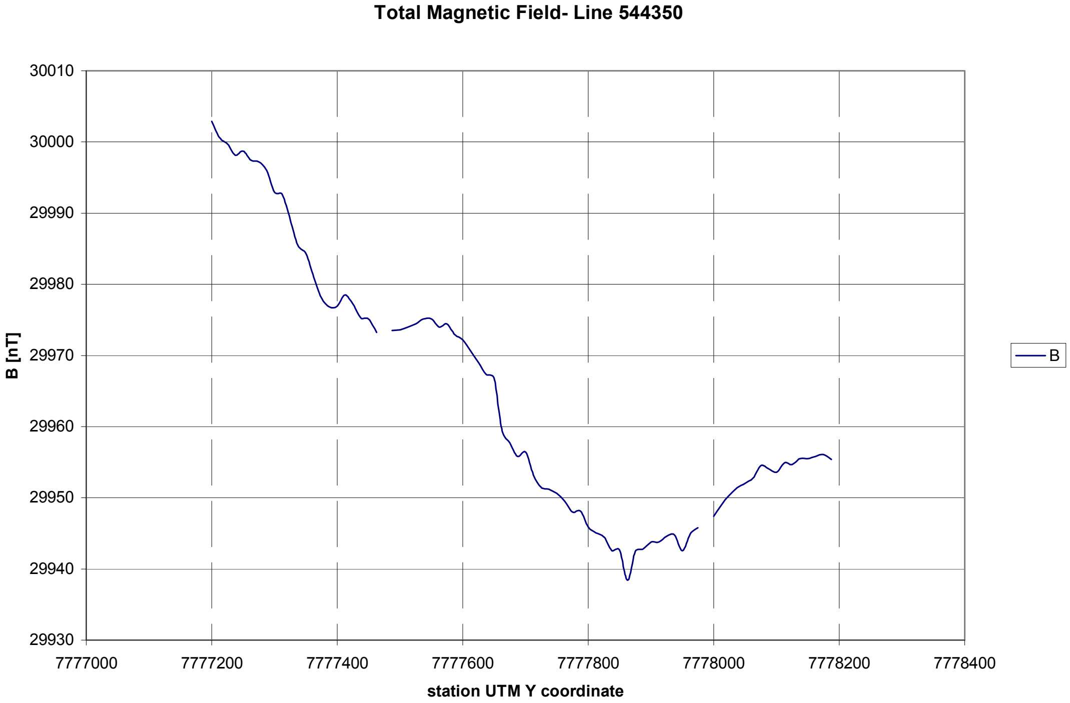

Fig. 3.14 Corrected Total Field for line 544350E.

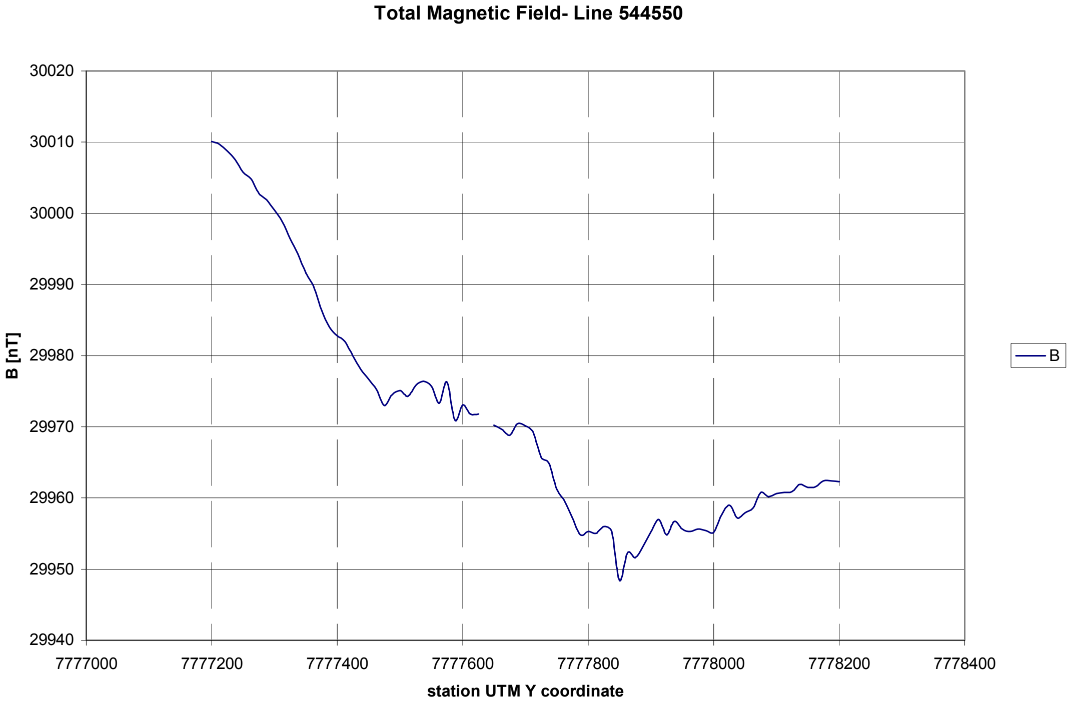

Fig. 3.15 Corrected Total Field for line 544550E.

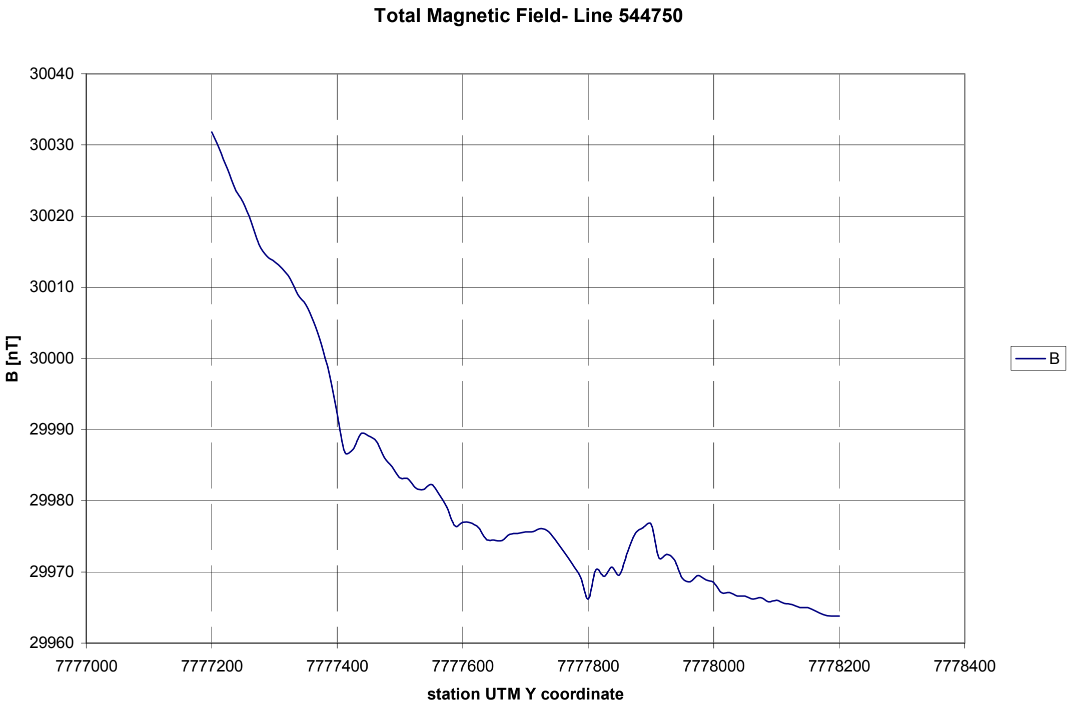

Fig. 3.16 Corrected Total Field for line 544750E.

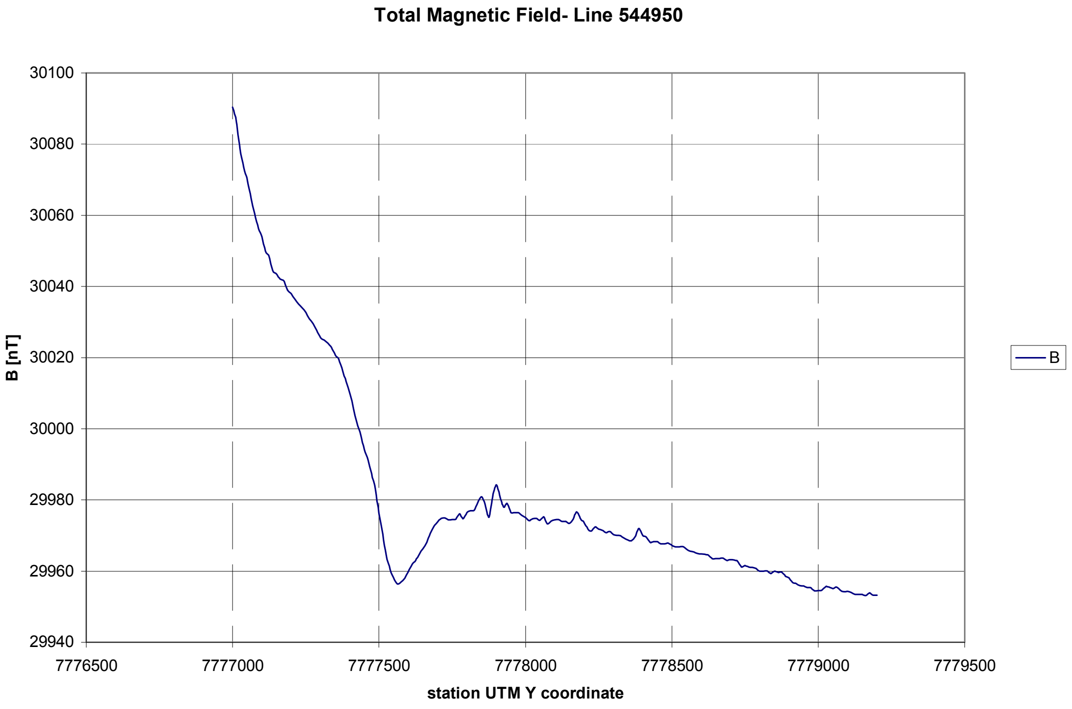

Fig. 3.17 Corrected Total Field for line 544950E.

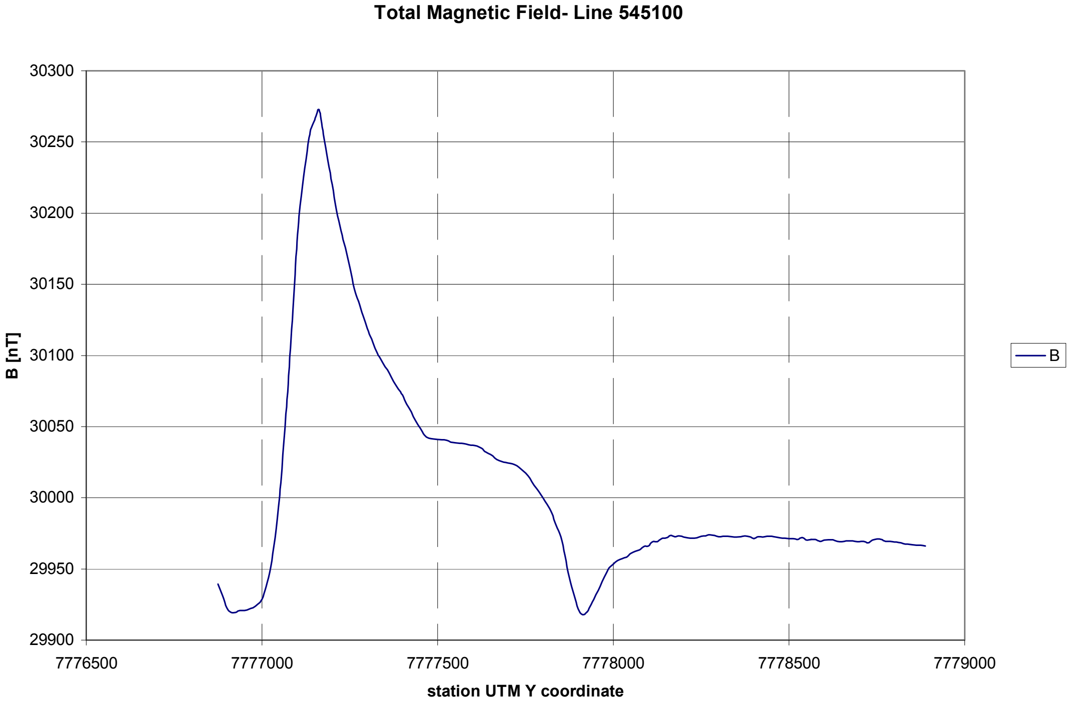

Fig. 3.18 Corrected Total Field for line 545100E (Kup7).

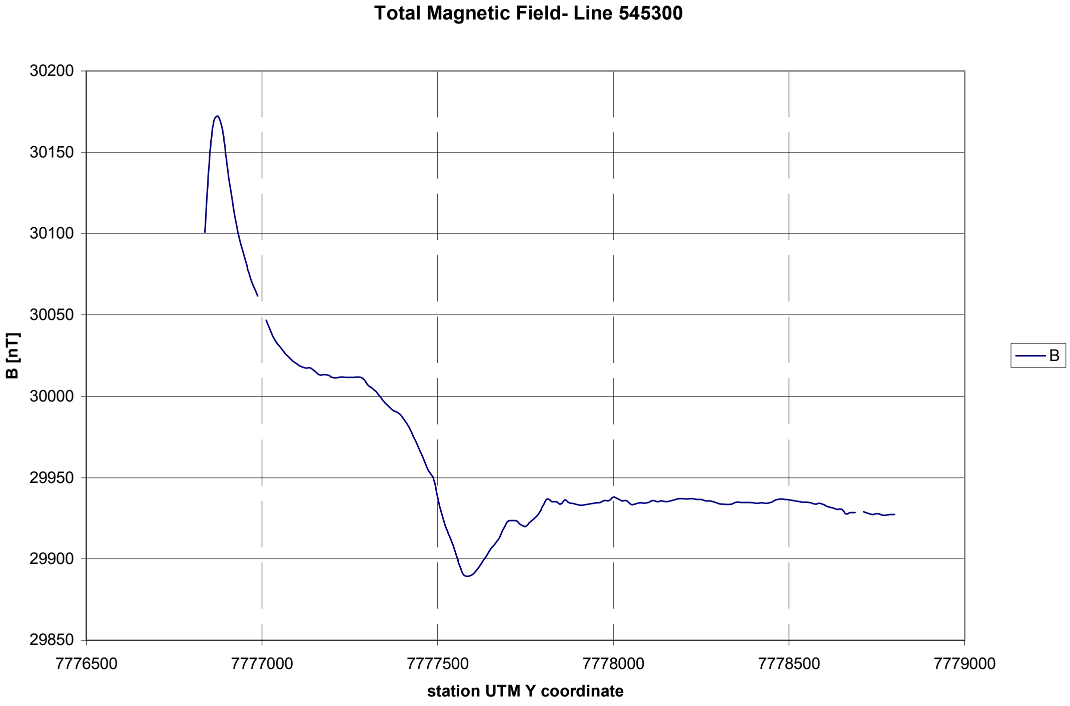

Fig. 3.19 Corrected Total Field for line 545300E (WF).

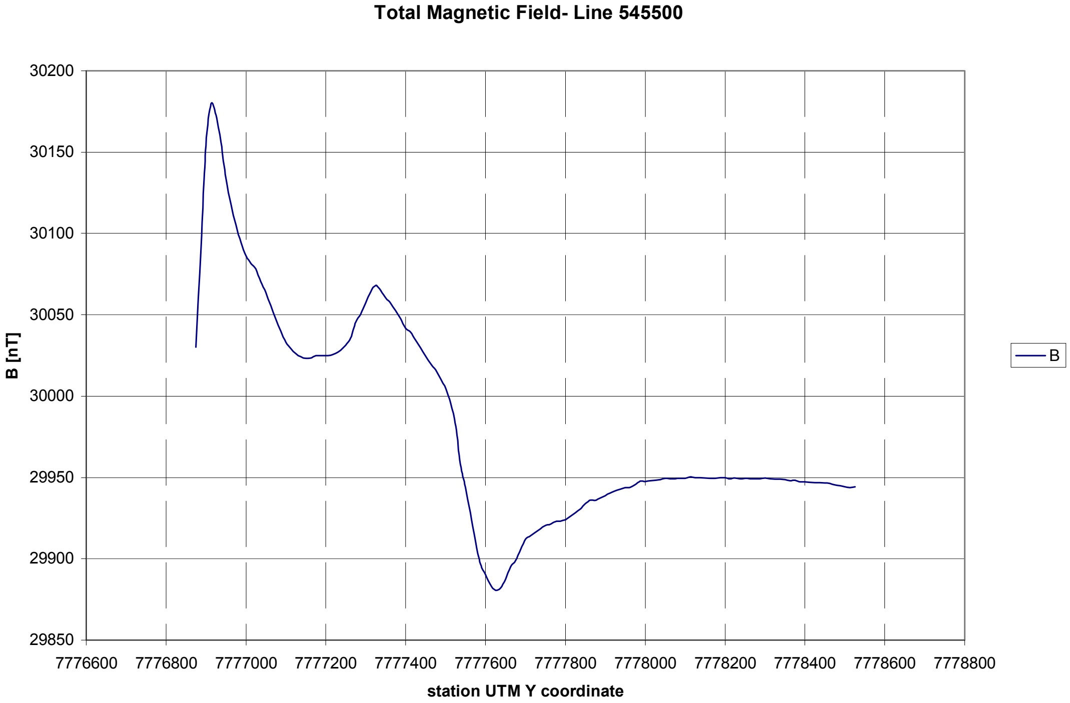

Fig. 3.20 Corrected Total Field for line 545500E (Kup21).

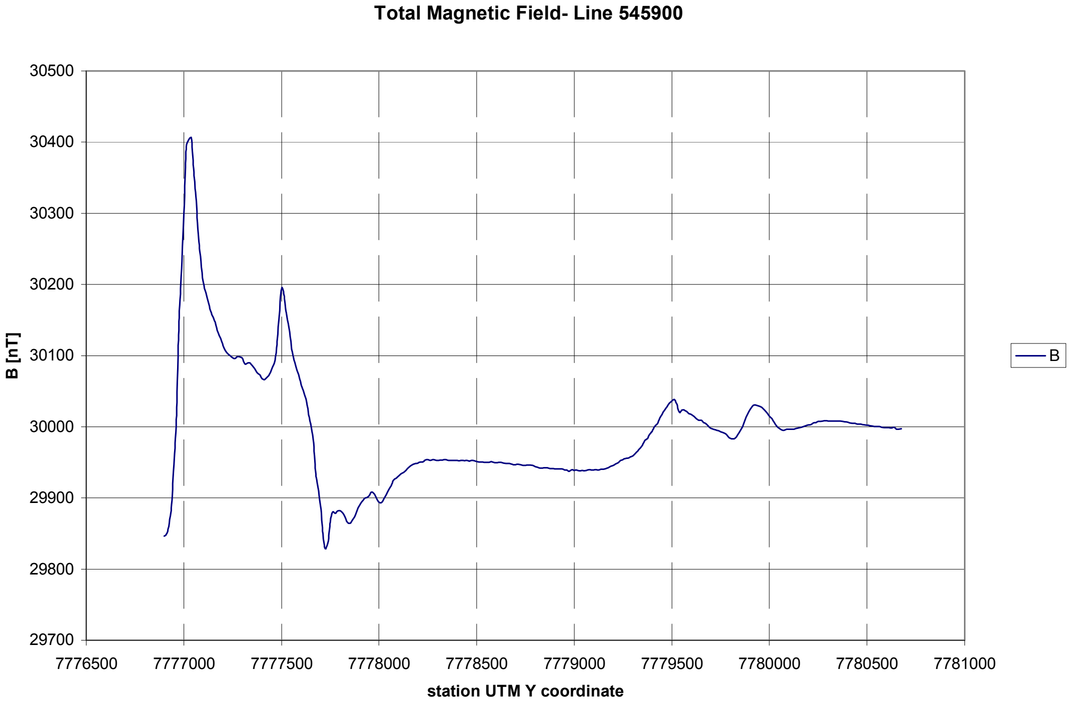

Fig. 3.21 Corrected Total Field for line 545900E (Kup22/13).

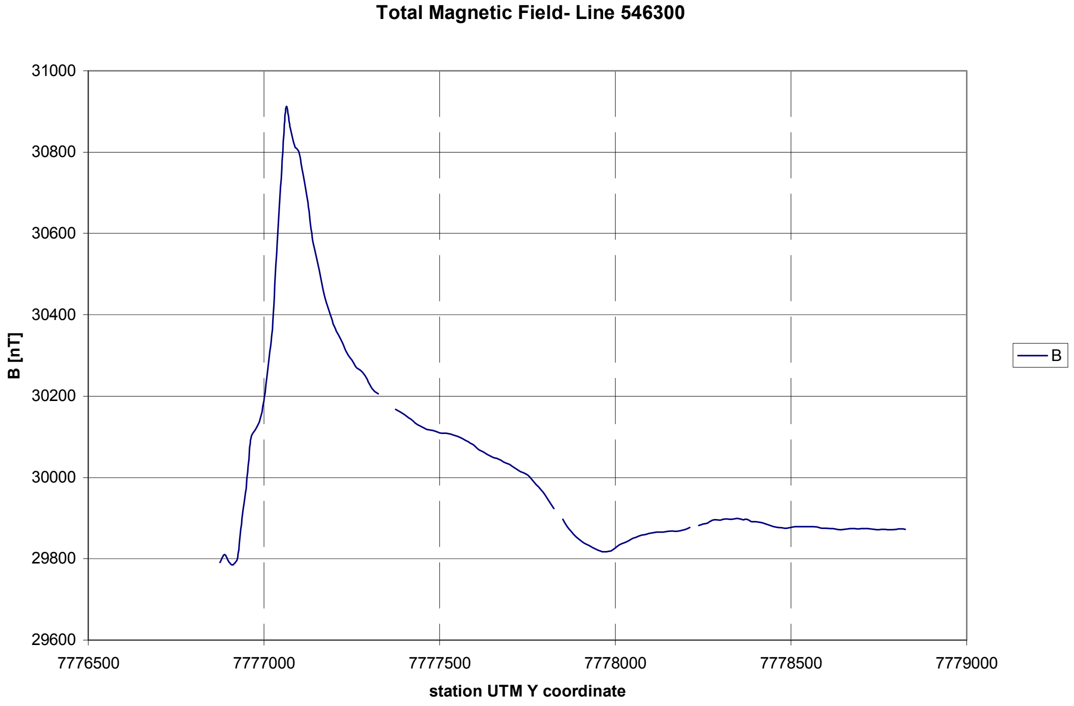

Fig. 3.22 Corrected Total Field for line 546300E (Kup8).

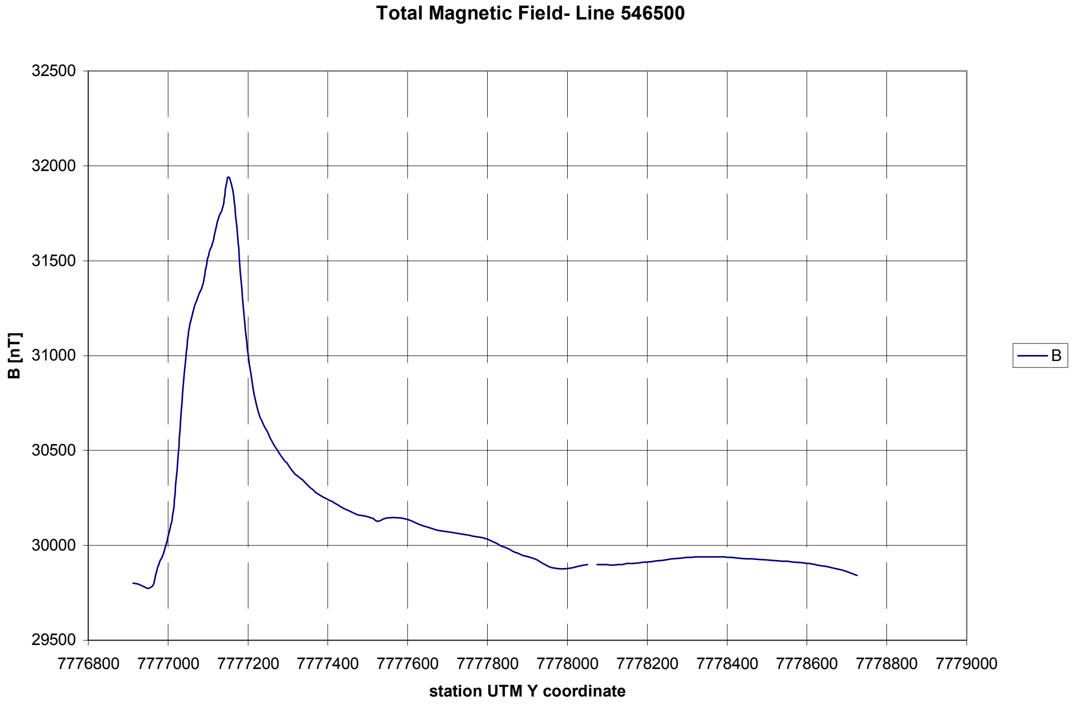

Fig. 3.23 Corrected Total Field for line 546500E (Kup15).

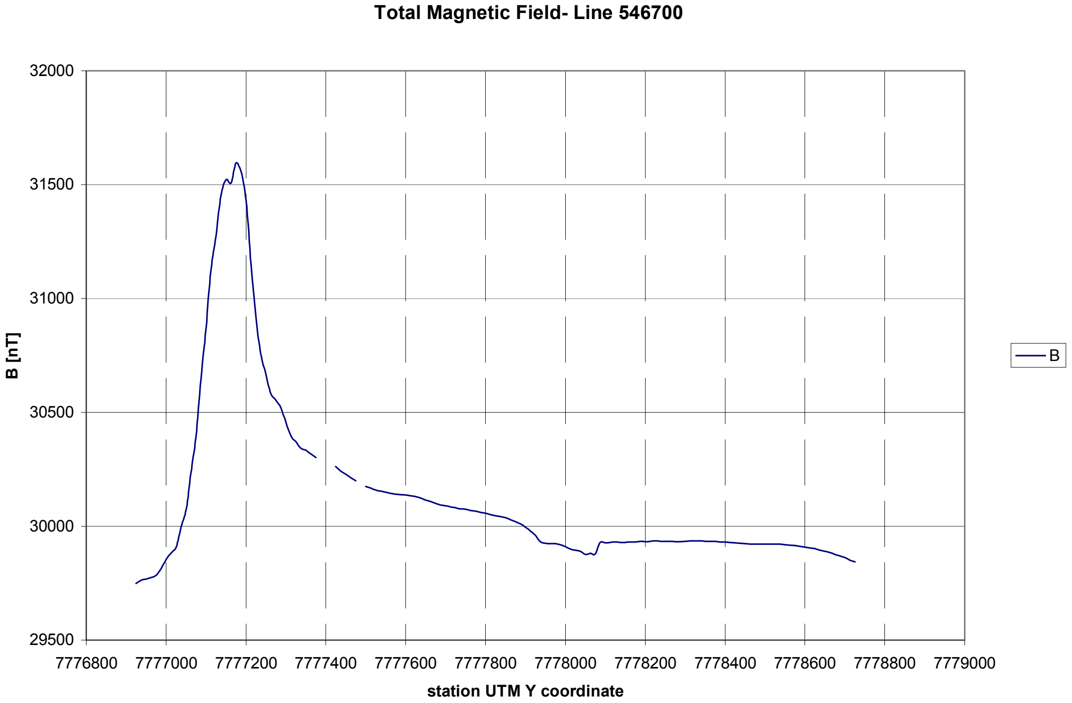

Fig. 3.24 Corrected Total Field for line 546700E (Kup16).

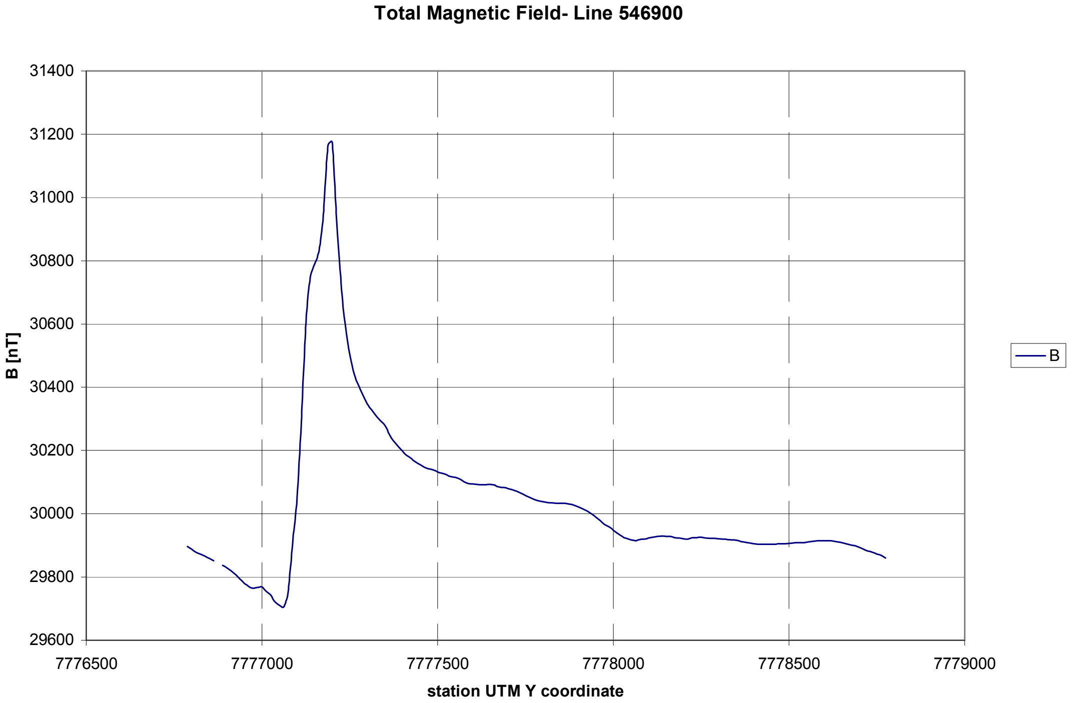

Fig. 3.25 Corrected Total Field for line 546900E (Kup17).

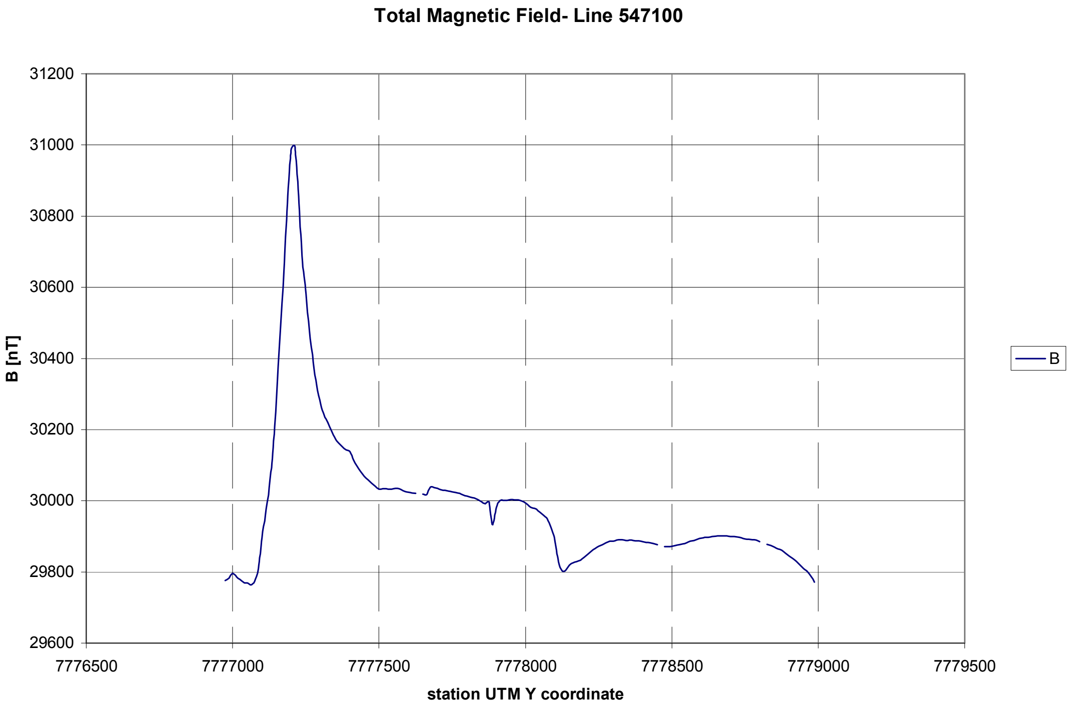

Fig. 3.26 Corrected Total Field for line 547100E (Kup18/20).

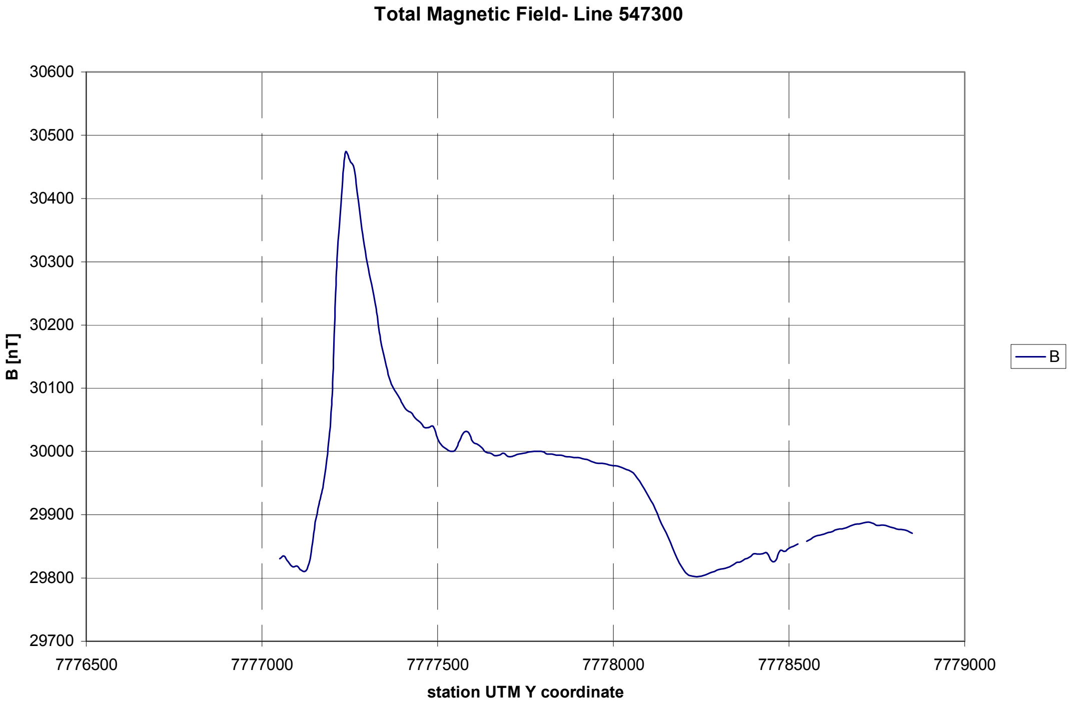

Fig. 3.27 Corrected Total Field for line 547300E (Kup19).

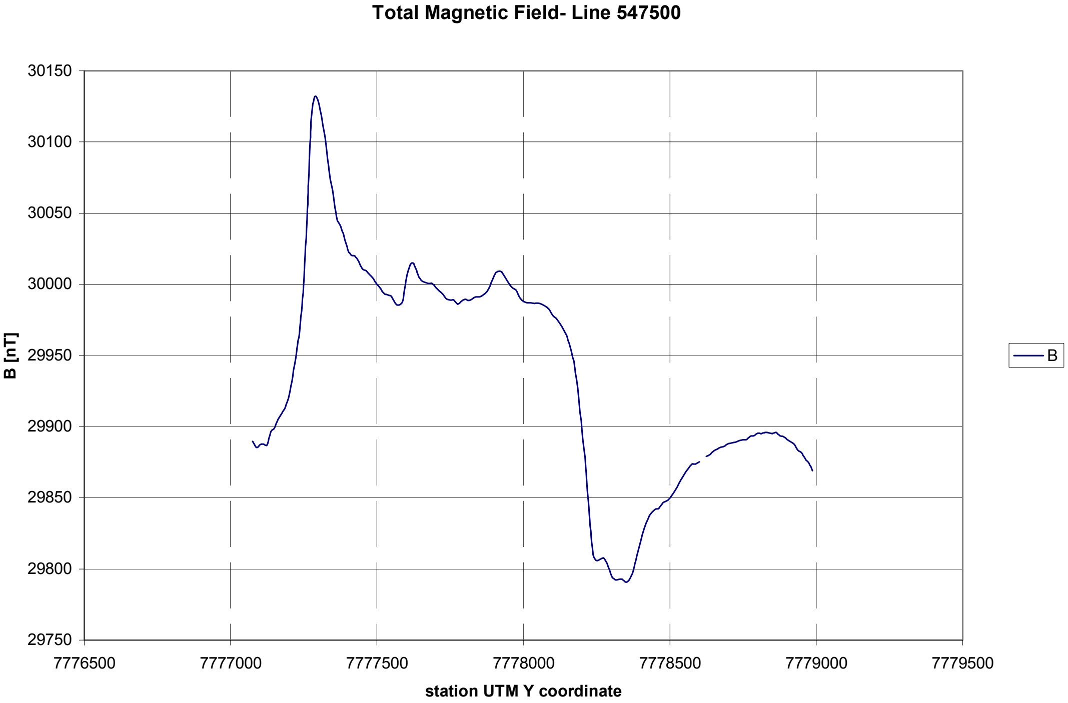

Fig. 3.28 Corrected Total Field for line 547500E (Kup9).

3.6.1.1 Line 544350

This profile (Fig. 3.14) begins at its maximum value of 30000,9 nT decreasing to a minimum of 29938,4 nT at 7862,5 N. The sloping regional gives this profile a negative anomaly amplitude of -35 nT.

3.6.1.2 Line 544950

Again like the profile above, this profile (Fig. 3.17) begins at its maximum value with part of its peak at the start of the line and decreases steadily to its minimum of 29956 nT at 7562,5 N. The sloping regional suggested for this profile gives a negative anomaly amplitude of -40 nT.

3.6.1.3 Line 545900

This profile (Fig. 3.21) displays double peaks at 7025 N and 7500 N. It then descends to the prominent negative anomaly at 7725 N, climbs to the regional and again to two small positive peaks at 9475 N and 9925 N. The dominant positive and negative anomaly amplitudes are 450 nT and -115 nT respectively.

3.6.1.4 Line 546900

This profile (Fig. 3.25) starts the line at around 29 900 nT and dips to the negative residual anomaly at an amplitude of about -200 nT. It then climbs rapidly to the anomaly peak at around 7175 N which has an amplitude of 1 300 nT. Beyond the peak going north the profile values diminish gradually to the regional.

3.6.1.5 Line 547500

The anomaly attains an amplitude of about 225 nT above the regional (Fig. 3.28). The profile rises sharply to the anomaly at around 7275 N before dropping to a level step with two superimposed peaks on it of about 25 nT each. From about 8250N to 8500N it falls to its negative residual with an amplitude of -110 nT.

3.6.2 Total field contour map

The contour map (Fig. 3.29) was generated using the Geosoft Oasis Montaj 43 mapping program. A lobe shaped anomalous magnetic feature in the southern part of the map is clearly defined striking ENE - WSW. This magnetic anomaly is enveloped by a broader ‘ridge’ of magnetic high values with a similar trend. The interpretation of the magnetic survey data is given in section 6.3.

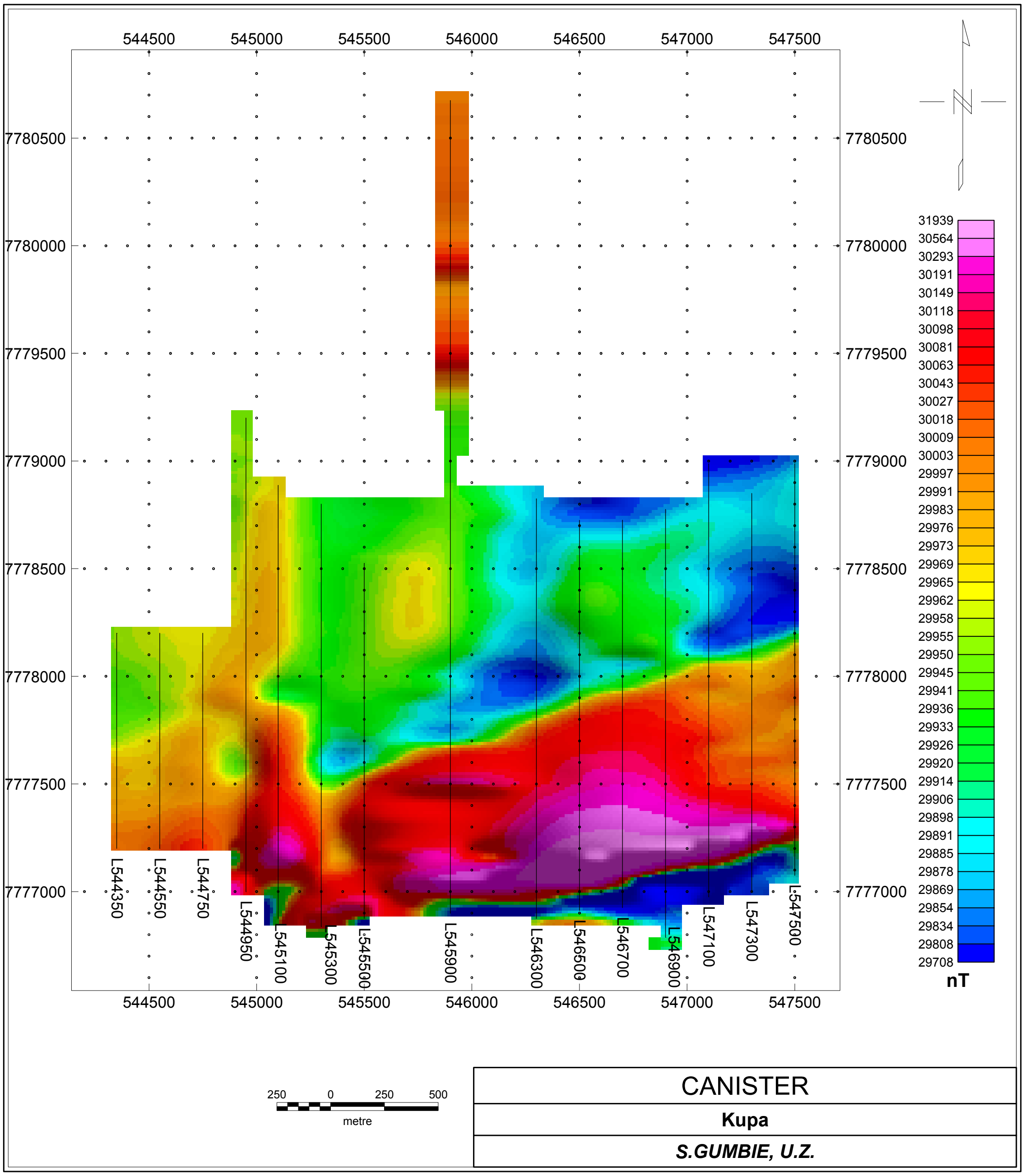

Fig. 3.29 Total magnetic field contour map for the Kupa ground magnetic survey.

Chapter Four

The Induced Polarisation Method

4.1 Principles

When a constant electric current is injected into the ground and is then abruptly turned off, it is observed that the voltage difference measured at two potential electrodes does not drop to zero immediately. After a large initial drop the voltage suffers a gradual decay and may take many seconds to reach a zero value. A similar effect is observed when the current is switched on. After an initial sudden voltage increase, the voltage increases gradually over a discrete time interval to a steady state value (Fig. 4.1). The ground thus acts as a capacitor by being able to store charge when a constant voltage is applied. This phenomenon is called induced polarisation (IP).

Two main mechanisms are responsible for the conduction of current in rocks: membrane or electrolytic polarisation and electrode polarisation. The two IP effects are indistinguishable by field measurements.

4.1.1 Membrane polarisation

This is due to the mobility of ions in the pore fluids and may occur in rocks which do not contain any metallic minerals. Clays and other platy minerals have negatively charged surfaces which attract positive ions from the pore fluids. When an electric field is applied, the positive-ion clouds are distorted and negative ions move into them, impeding current flow. A reverse current flows and slowly establishes the original equilibrium when the

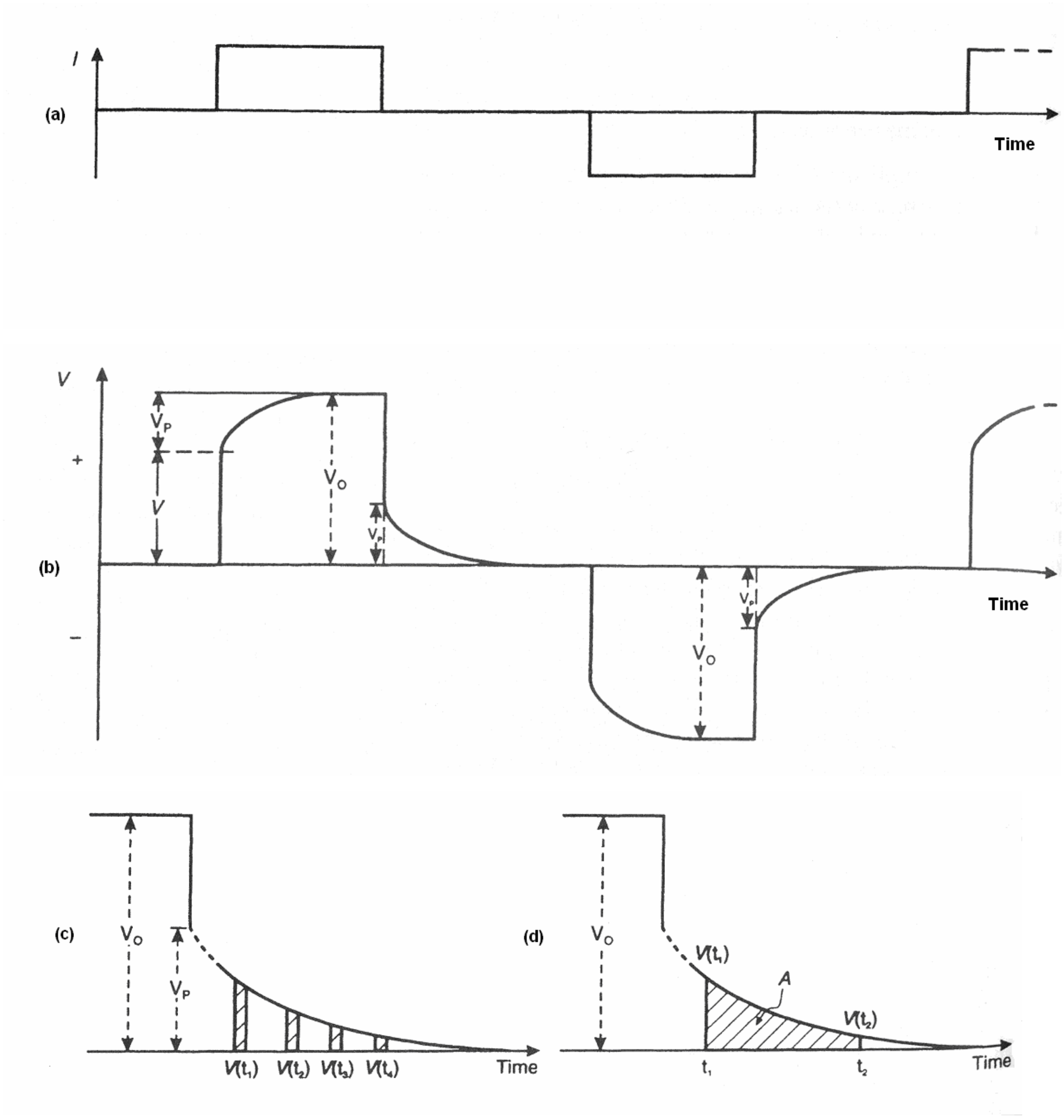

Fig. 4.1 The IP effect and the parameters used to quantify it (after Reynolds, 1997).
(a) input ac current; (b) observed voltage difference (V_o) in rocks and the effects of the overvoltage or polarisation voltage (V_P) on the actual voltage (V) producing rise- and decay-times; measurement of chargeability by: (c) integration of voltage ‘slices’ (~ 100 ms) or; (d) area under curve between t_1 and t_2.

field is removed. Also most rock forming minerals have a net negative charge on their interface with the pore fluids and where the passages are constricted: this causes charges to build up on either side of the blockage when the external current is applied (Fig. 4.2).

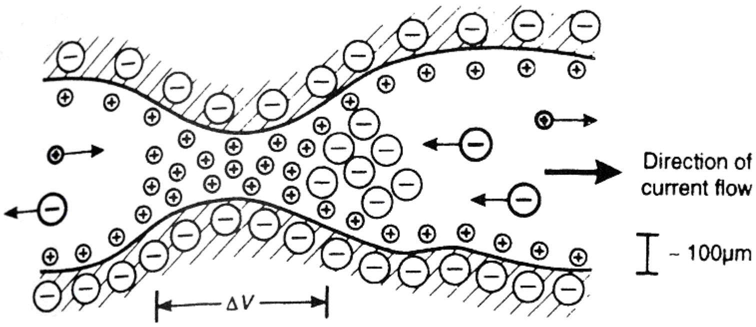

Fig. 4.2 Accumulation of charge at a constriction illustrating membrane polarisation (after Reynolds, 1997).

When the external current is switched off, the charges drift back to their equilibrium state and in the process cause the current to decay slowly to zero, thus displaying the IP effect.

4.1.2 Electrode polarisation

Electrode polarisation occurs when there are metallic particles distributed throughout the rock. The mechanism of conduction is both electrolytic and electronic and involves most metallic sulphides and oxides such as magnetite, ilmenite and cassiterite. Graphite also demonstrates this type of polarisation particularly well and may deceive the metals explorer.

Consider a blockage in a pore passage as shown in Fig. 4.3. The presence of a mineral grain in blocking a pore and having net surface charges of opposite sign on either face results in an accumulation of ions in the surrounding electrolyte.

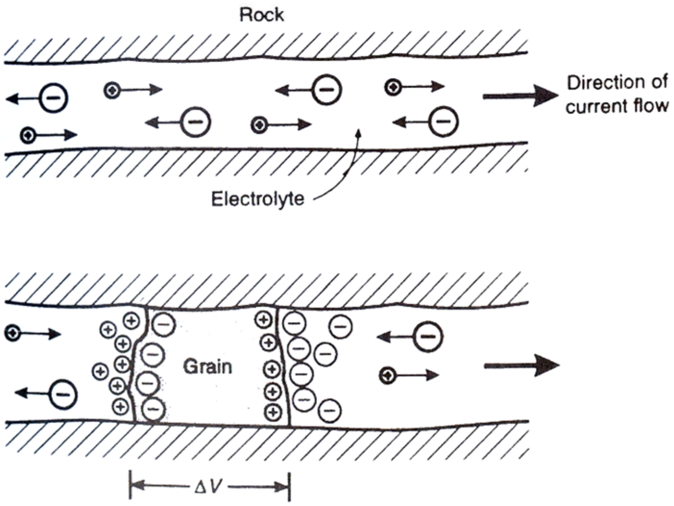

Fig. 4.3 Blockage of a pore passage by a mineral grain in electrode polarisation (after Reynolds, 1997).

When current flows, an electron exchange takes place at this interface and because current flow in the electrolyte is much slower than in the metal, the pileup of ions is maintained by the external voltage. On switching off the current, the residual voltage decays as the ions diffuse back to their original equilibrium state. This is the observed IP effect. The magnitude of the effect depends on the impressed voltage, mineral concentration and porosity, but since it is a surface phenomenon, it is larger for disseminated rather than massive minerals.

4.2 Measured IP parameters

IP measurements may be made in either the time domain or the frequency domain. The measurement of a decaying voltage over a time interval is known as Time Domain IP surveying. Measurement of apparent resistivity at two or more low ac frequencies is known as Frequency Domain IP surveying. The parameters determined from the measurements are apparent resistivity, chargeability, frequency effect and metal factor. The time domain parameters are defined and discussed in section 4.2.2. A discussion on the different geometrical layouts employed in the field is considered next.

4.2.1 Geometric arrays

The most commonly used field configurations are the Schlumberger, gradient, dipole-dipole and pole-dipole. The dipole-dipole and pole-dipole are the arrays that are commonly used (see Fig. 4.4). These are discussed below.

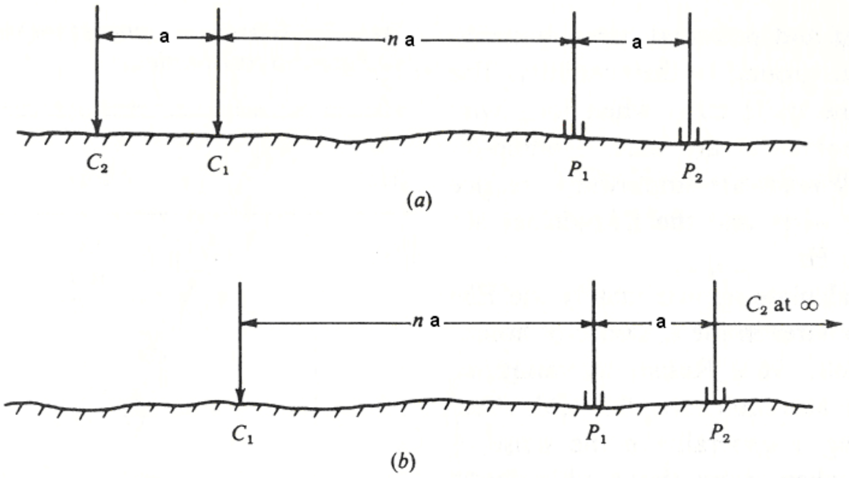

Fig. 4.4 Typical IP spreads (a) the dipole-dipole and (b) the pole-dipole. For the pole-dipole array, the current electrode at 'infinity' is usually located at > 5*na* (after Telford et al., 1990).

4.2.1.1 Dipole – dipole array

As shown in Fig. 4.4 (a), this array is symmetrical about a central point with the two current electrodes close together on one side of the centre and two potential electrodes equally close together on the other side. This has good resolution both horizontally and vertically such that even narrow vertical bodies can be resolved. The disadvantage is that it has a low signal level compared to the pole – dipole array and thus it requires more power. Data is plotted at the intersection of 45° lines from the midway of $C_1C_2 - P_1P_2$

(Fig. 4.5) and anomalies are symmetrical giving a characteristic “pant leg” or triangular shape on the so-called pseudosections.

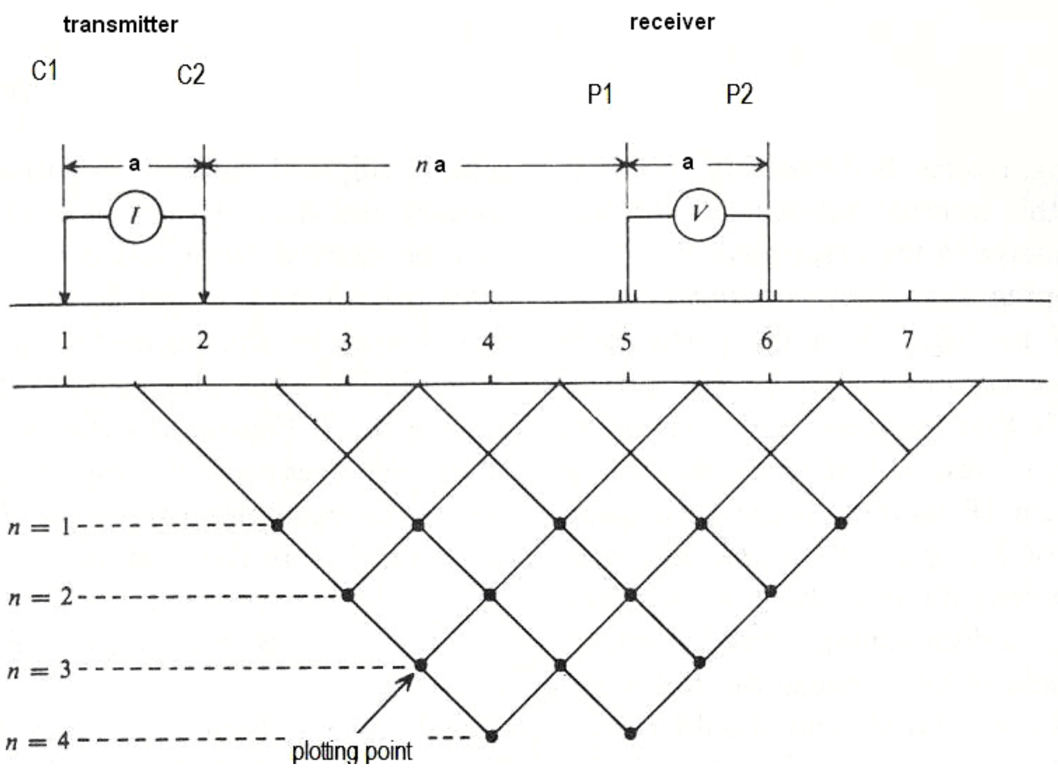

Fig. 4.5 The dipole – dipole plotting point for IP pseudosections.

The apparent resistivity over homogeneous ground for the dipole-dipole array is

$$\rho_a = \pi n(n+1)(n+2)a\frac{V}{I} \quad \text{…...………………} \quad (4.1)\ \text{(Telford et al., 1990)}$$

4.2.1.2 Pole – dipole array

This array is shown in Fig. 4.4 (b) and has an increased signal strength compared to the dipole – dipole array. Its vertical and horizontal resolution are poorer compared to the dipole-dipole array. Anomalies are asymmetrical and appear to dip away from the infinite current pole. Data is plotted at the midpoint of $C_1 - P_n P_{n+1}$ with the ‘infinity’ electrode C_2

being located far from the line. The apparent resistivity over homogeneous ground for this configuration is

$$\rho_a = 2\pi n(n+1)a\frac{V}{I} \quad \ldots\ldots\ldots\ldots\ldots\ldots\ldots\ldots\ldots \quad (4.2)$$ (Telford et al., 1990)

4.2.2 Time domain

Fig. 4.1 illustrated the quantities used in making the measurements.
The apparent resistivity, ρ_a is obtained from

$$\rho_a = \frac{V_p}{I} \times K, \quad \ldots\ldots\ldots\ldots\ldots\ldots\ldots\ldots\ldots \quad (4.3)$$

where *K* is the geometric factor of the array (section 4.2.1).

A quantity known as apparent chargeability *M* is defined (Sumner, 1976) as

$$M = \frac{1}{V_p}\int_{t_1}^{t_2} V(t)dt \quad \ldots\ldots\ldots\ldots\ldots\ldots\ldots\ldots \quad (4.4)$$

and is measured in ms. The instrument evaluates the area between t_1 and t_2 (Fig. 4.1(d)) allowing more information on the curve to be obtained which enables a value of V_p to be determined since it is not possible to measure this value directly due to the high gradients and transient electromagnetic fields at current turn off. This is achieved essentially by an integrating voltmeter with a range from dc to very low frequency ac. The chargeability may also be defined (Fig. 4.1(c)) and computed by

$$\mathrm{M} = \frac{1}{V_p}\frac{\int_{t_1}^{t_2} V(t)dt}{(t_2 - t_1)} \quad \ldots\ldots\ldots\ldots\ldots\ldots\ldots\ldots \quad (4.5)$$

and is measured in mV/V.

4.3 Field procedures

4.3.1 Instrumentation

A Scintrex IPC-7/1 KW solid state transmitter was powered by an electric generator consisting of a VW 4-cylinder engine and dynamo mounted on a metal frame as illustrated in Fig. 4.6. The generator is capable of producing 115 V a.c. at 400 Hz which can be multiplied to 5000 V at the transmitter. Typical operating currents are 0,5 – 2,5 A working in low resistive ground such as clays to highly resistive sands. The operating parameters of the transmitter are: a maximum voltage of 300 V a.c. or 5 kV d.c.; 20 A current; a 2 s, 4 s, 8 s (on/off) pulse range and; a 0,71 – 1,20 multiplier range.

a **b**

Fig. 4.6 IP power generation and transmission equipment; (a) transmitter, (b) generator. The equipment shown belongs to GPR Zimbabwe.

The receiver was a Scintrex IPR-12 time domain induced polarisation/resistivity receiver. It can accept signals from 8 potential dipoles simultaneously, is capable of solid state memory recording and can automatically calculate the IP parameters. Information is displayed on a large 16 line by 42 character liquid crystal display using a 17-key keypad (Fig. 4.7). Data can be output to a printer or a computer and the receiver has an internal power supply.

Fig. 4.7 The front panel of the Scintrex IPR-12 receiver.

Fig. 4.8 shows the field setup of the equipment. Radio communication of the input current to the ground from the transmitter was achieved using 3 Kenwood 2-way radios with the antenna located at the highest point near the transmitter. These radios have a range of the order of a few kilometres which was sufficient for the project area.

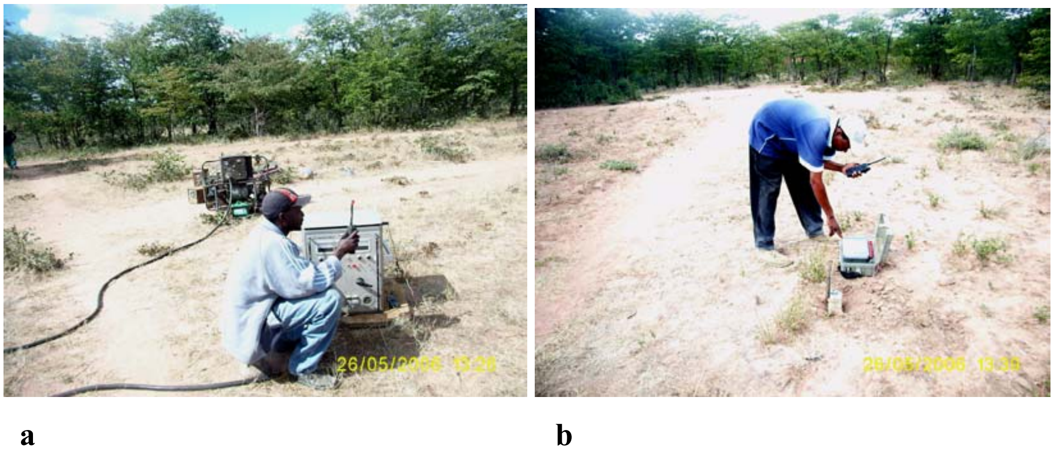

Fig. 4.8 (a) Generator and transmitter in field operation. (b) Receiver taking measurements. An illustration of the use of the communication radios.

4.3.2 The IP survey at Kupa

GPR Zimbabwe had been contracted by Canister to carry out the IP survey and had already done 4 lines before the author joined them. The client preferred the pole – dipole array since the survey area is in sands which are operationally difficult to drive reasonable currents into the ground. Thus, a pole-dipole array was employed with a station spacing of 50 m. The current electrode at infinity (C_2) was located at 500 m perpendicular to the survey line. It was constructed by digging two 30 cm^3 holes 1 m apart and driving two steel stakes firmly into the ground and filling with water. They were then connected to each other and to the transmitter cable by insulated copper wire. The 'in-line' electrode (C_1) consisted of two steel stakes to increase contact with the ground and was located 100 m behind the first potential electrode (P_1). The spread consisted of 7 potential 'pot' electrodes (n = 6) with the receiver located midway at P_4. Three additional IP lines were done by the author, Line 545500E (Kup21), 545900E (Kup22) and 546700E (Kup23). All lines were surveyed from south to north.

A typical daily survey included the following procedures:

- Ensuring enough labour is available for the survey, a complement of 22 people was used.
- Potential electrodes checked for damage and filled with $CuSO_4$ solution.
- Generator serviced and run.
- Communication radios checked for operation.
- On site, coordinates of C_2 electrode entered into GPS and located on ground by one crew.
- Another crew assigned to dig all holes to be used by electrodes at survey pegs and fill them with water.
- Two crews delegated with cable reels to C_1 and C_2 whilst 7 individuals were assigned to pot electrodes.

- The last crew placed at roads, pathways and other strategic positions to guard cables from human and animal interference. A supervisor was elected to coordinate this critical function.
- The geophysicist or field operator has the overall responsibility for the safety of all staff and conducting the survey.

The survey proceeded by:

- The receiver operator (usually the geophysicist) entering the coordinates of all the potential electrodes into the receiver and checking that they are all connected by observing the resistances on the receiver screen.
- Communicating to the transmitter operator and the C_1 crew by the receiver operator that the survey is ready to commence.
- The transmitter operator communicates to survey crew to take caution before starting the generator.
- The size of the current is communicated to the receiver operator from the transmitter operator and after 7 cycles of the input waveform, the information is stored digitally and the whole array is advanced by 50 m to the next peg.
- When the leading pot (P_7) reaches the end of the line, it is removed and the pots are eliminated from the array successively after each reading until the P_4 pot with the receiver reaches the last peg. Then the pots are removed from behind (P_4 remains fixed) until only two potential electrodes remain in the spread. C_1 is maintained at a constant separation from the lagging pot throughout the survey.

At the end of the day, the data was downloaded or “dumped” onto a field computer and the pseudosections checked before handing them to the client (geologist).

4.3.3 Precautions and problems

Some essential precautions were:

- Enforcing strict safety at the current electrodes by protecting them against animal and human contact as the high currents and voltages used are potentially lethal.
- Ensuring that a good separation of about 5 m is kept between the current and potential cables in order to minimize electromagnetic field effects.
- Monitoring of parameters whilst taking measurements on the receiver to check for the quality of the readings.

Some of the major problems encountered were:

- Training of new labour.
- Breakdown of generator.
- Breakdown of communication radios.
- Water shortage in the field, far away from camp.
- Villagers' fields and homesteads in survey grid (see Figs. 1.2 and 1.3). On one occasion the survey had to be discontinued because a villager refused to have a survey line run through his homestead area.
- Busy tracks used by donkey carts causing disruptions.
- Occasional cable breakages due to vegetation and roaming livestock but this was rare on well executed surveys and clear lines.

4.4 Presentation of results

The IP data for line Kup23 is given in Appendix A4. IP pseudosections of apparent resistivity and chargeability, were produced for six lines: 545500E (Kup21), 545900E (Kup22), 546500E, 546700E (Kup23), 546900E and 547100E (Figs. 4.9 – 4.14). Caution needs to be practiced in extrapolating the positions of the anomaly peaks as they are displaced from the centres of conductive or chargeable bodies. Because the current electrode trails behind the potential electrodes, there is a shift to the north of the actual measurement positions. A ‘distillation’ map of the IP results at different n ‘depth’ values would have greatly aided the qualitative analysis of the results but unfortunately time did not permit.

In general, the main anomalous high chargeability feature was seen in a central position on the line furthest west (Kup21) and it shifted to the northern sections of the lines as the grid was traversed towards the east. In a similar traverse across the grid, the low resistivity anomaly started fairly ‘flat’ from surface to shallow depths, deepening towards the north and then shallowing again on line 547100E (Fig. 4.12).

4.4.1 Line 545500E (Kup21)

The resistivities are anomalously low (< 300 Ω m) across the whole line to a relatively shallow-medium depth (n = 1 to n = 4) (Fig. 4.9). Two chargeability anomalies of magnitude 1,8 mV/V are noted at surface, one in the southern part of the line and the larger near the centre, widening with depth to form a typical “pants leg” anomaly.

4.4.2 Line 545900E (Kup22)

The southern chargeable body on surface starts at 7075 N with values of 2,6 mV/V and is about 100 m wide, fanning out with depth (Fig. 4.10). The second chargeable high, 2,0 mV/V in magnitude, is only about 50 m wide starting from 7750 N but is the larger subsurface feature of the two. A peculiar low resistivity feature (< 400 Ω m) surrounded by higher resistivities (reaching > 700 Ω m) lies below the southern chargeable body centred around n = 5 but this could be a single point data error. The general resistive pattern is of a deepening of low resistivities (< 550 Ω m) towards the north with these low resistivities going down to n = 6 from 8125 N.

4.4.3 Line 546500E (Kup15)

Fig. 4.11 shows a broad southern chargeable anomaly, with peak values of 2,6 mV/V, which widens with depth and is separated from another high chargeability feature (of value 2,2 mV/V) further north by an anomalously low chargeability (< 1,0 mV/V) subvertical region. The low resistivity anomaly zone, of values < 500 Ω m, deepens from south to north along the line.

4.4.4 Line 546700E (Kup23)

The two chargeable zones seen in line Kup22 have separated and are further away from each other with the southern anomaly becoming elongate (Fig. 4.12). The resistivity lows begin to the south going down to a shallow depth (n = 2) and then increase more rapidly with depth than in Kup22. From 8075 N going north the low resistivities (< 500 Ω m) extend to n = 6.

4.4.5 Line 546900E (Kup17)

Three prominent chargeable anomalies (> 2.3 mV/V) are seen along the line at n = 4 (Fig. 4.13). The largest and northernmost one widens with depth in a pants leg shape. There is a narrow tabular low resistivity feature (< 150 Ω m) at peg 8031 N spanning approximately 80 m on surface and dipping steeply to the north which is not visible in the other pseudosections.

4.4.6 Line 547100E (Kup18)

The dominant chargeability anomaly is in the northern section of the line and begins from the surface as two broad features of values of 3,4 mV/V, that merge with depth and is inclined to the south (Fig. 4.14). In the resistivity pseudosection, the low resistivities reach their deepest in the north, extending to n = 6.

Further consideration of these results is given in section 6.5.

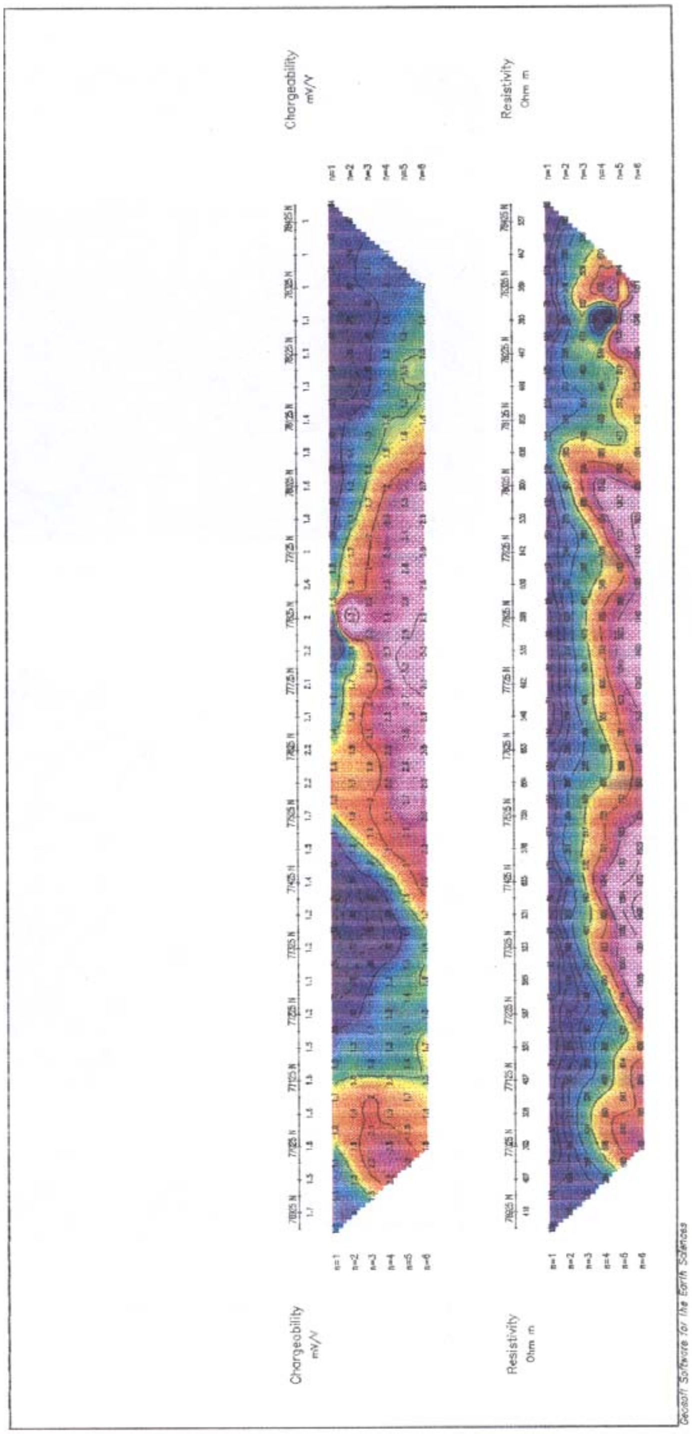

Fig. 4.9 Pseudosections of chargeability and resistivity for line 545500E (Kup21).

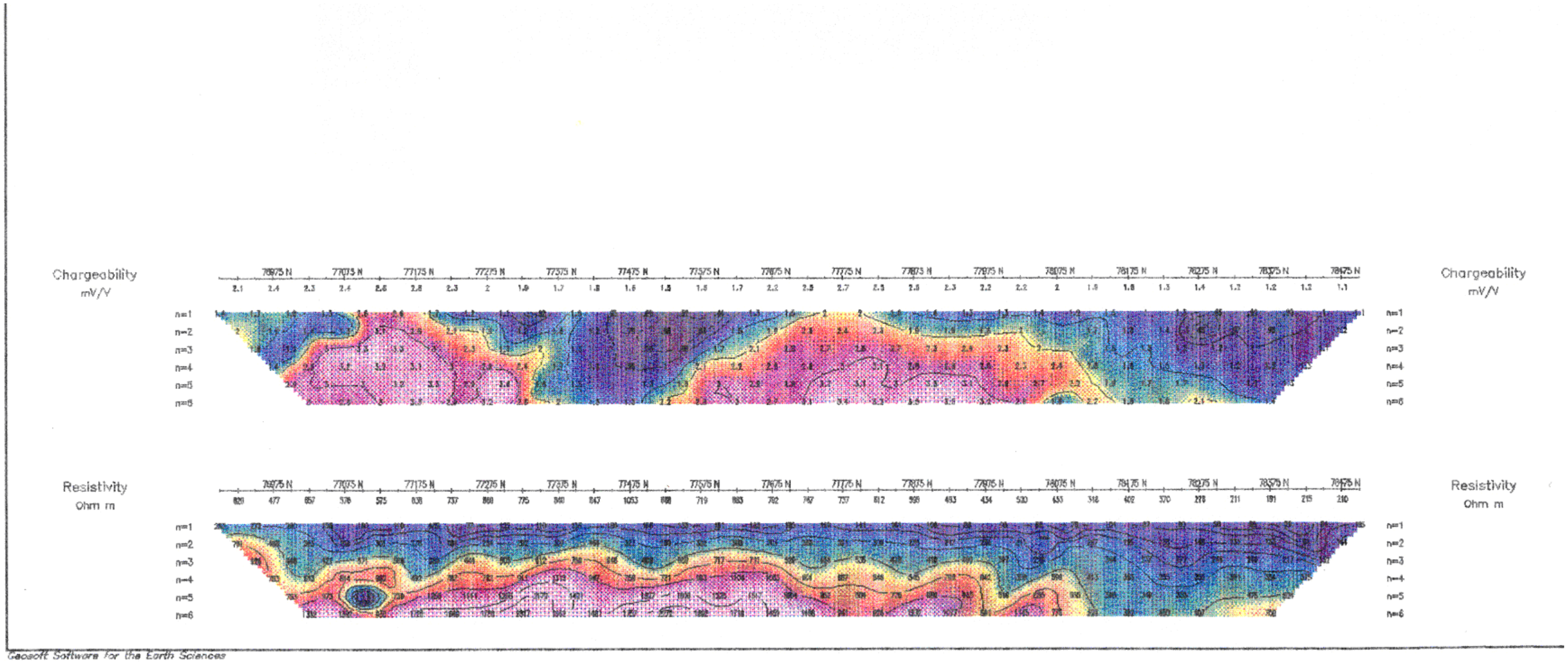

Fig. 4.10 Pseudosections of chargeability and resistivity for line 545900E (Kup22).

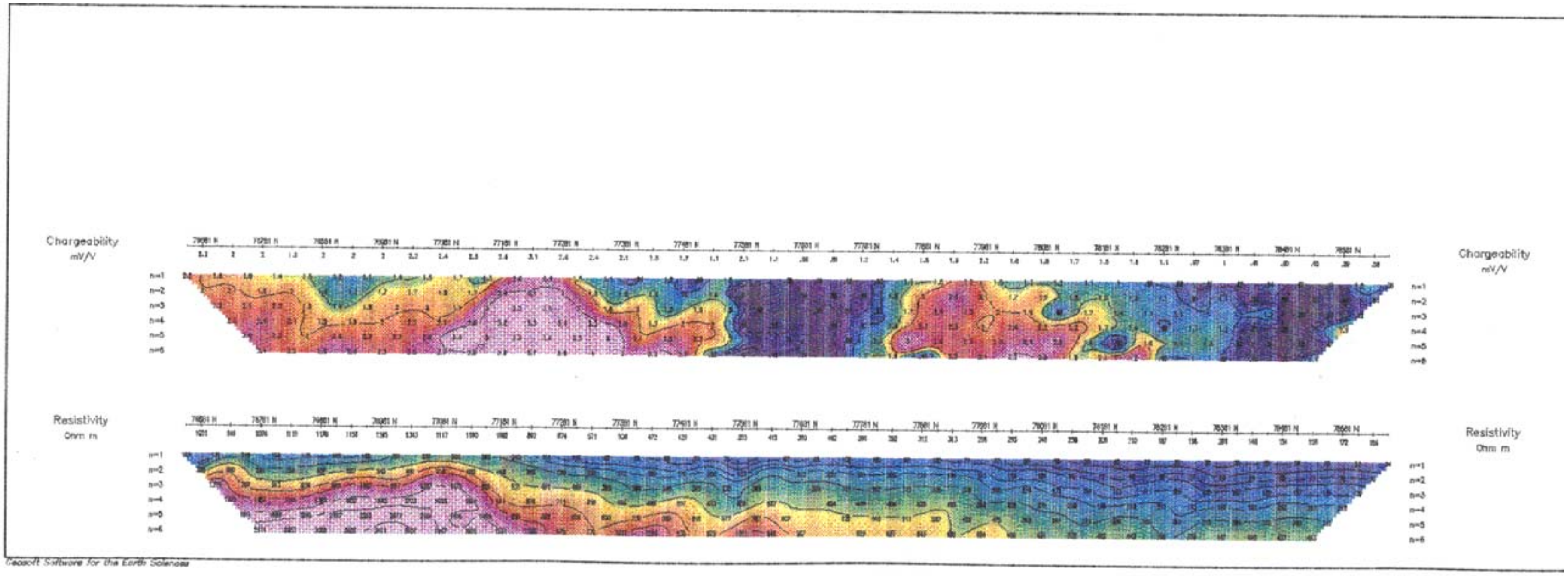

Fig. 4.11 Pseudosections of chargeability and resistivity for line 546500E (Kup15).

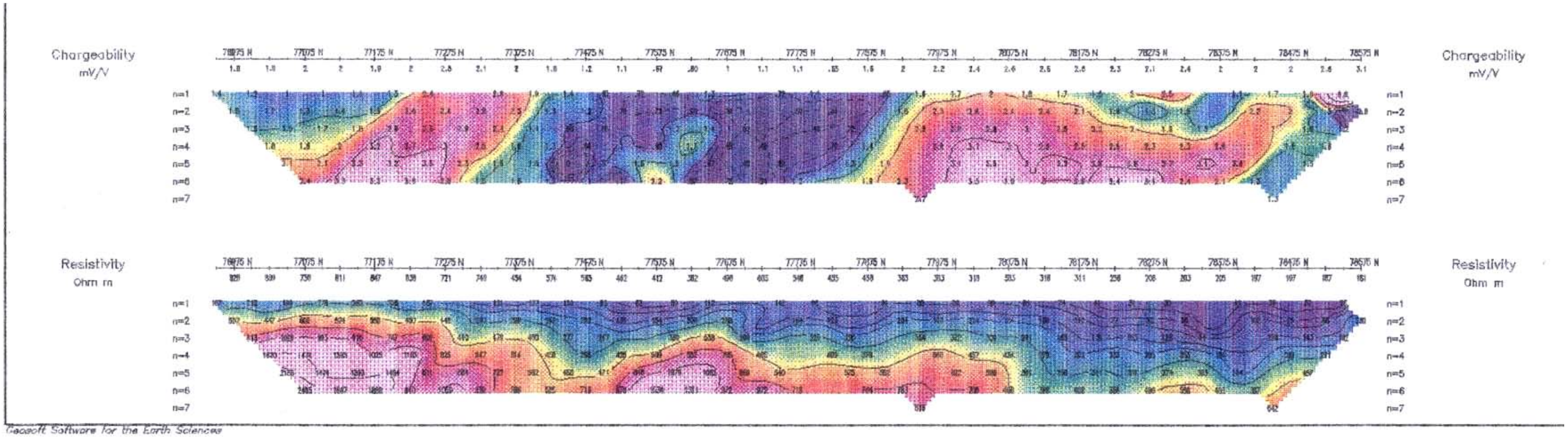

Fig. 4.12 Pseudosections of chargeability and resistivity for line 546700E (Kup23).

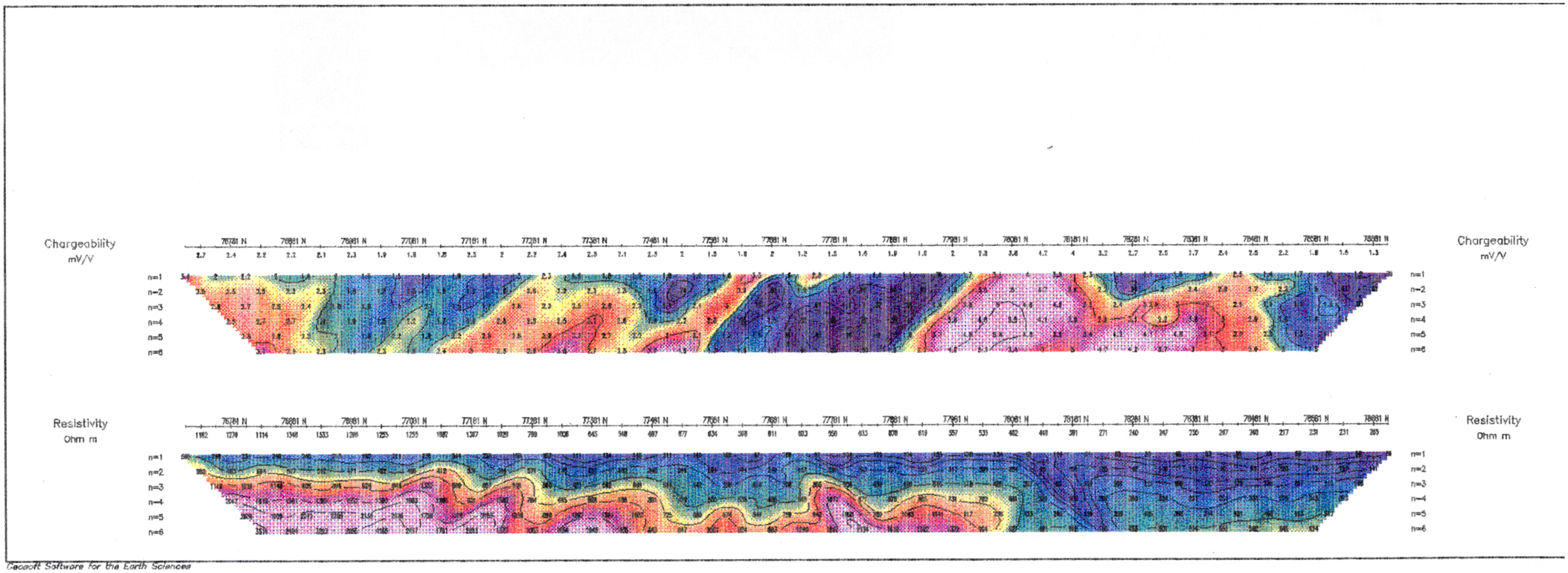

Fig. 4.13 Pseudosections of chargeability and resistivity for line 546900E (Kup17).

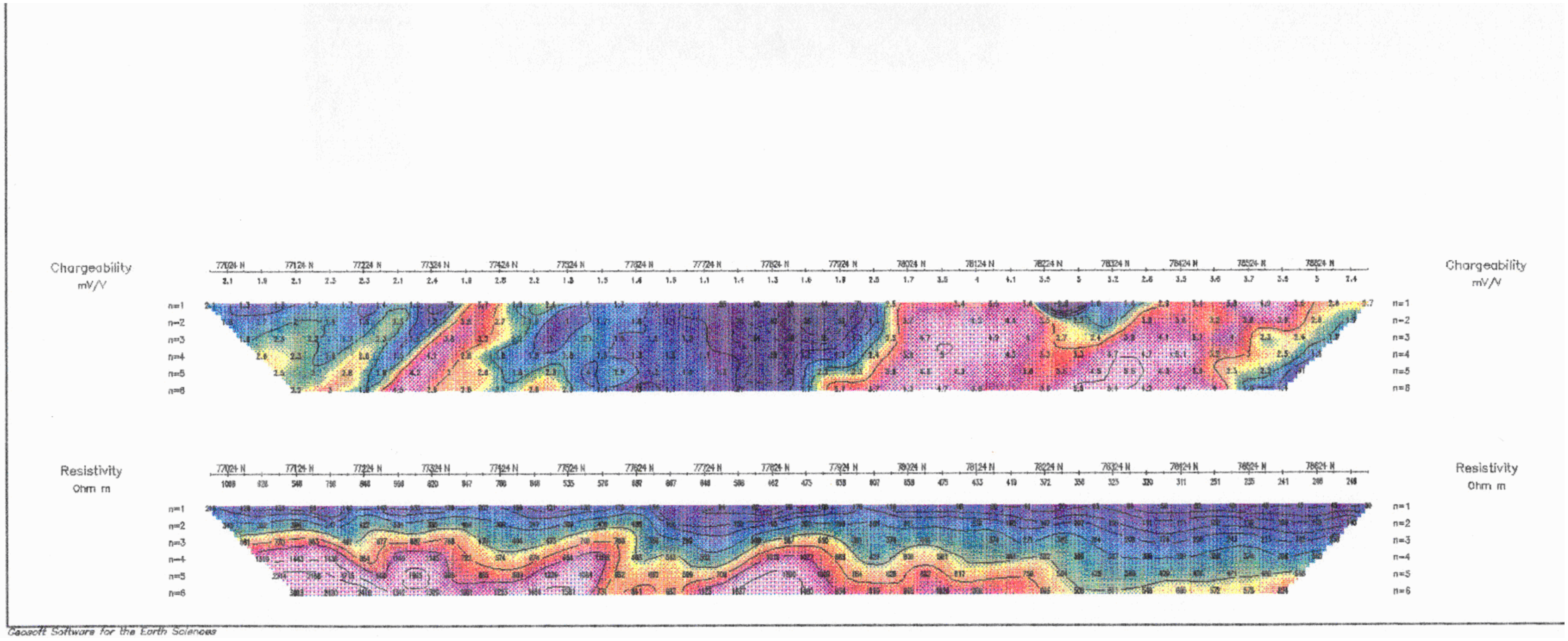

Fig. 4.14 Pseudosections of chargeability and resistivity for line 547100E (Kup18).

Chapter Five

The Radiometric Method

5.1 Introduction

The radiometric method is based on the radioactive properties of rocks and has been used with relatively minor emphasis for ground geophysical investigations. However, gamma-ray prospecting, as it is sometimes known, is a cheap and fast method of searching for some industrial minerals and potassium in alteration zones associated with base metal mineralization (Morse, 1977). Geological mapping and structural interpretations can also be done.

5.2 Basic Principles

5.2.1 General

Many heavy atoms are unstable and decay spontaneously to a less massive form. Radioactive atoms decay by the emissions of alpha (α) or beta (β) particles and gamma (γ) rays. An α particle is an ionised helium atom. A β particle is an electron that originates from the nucleus when (a) a neutron splits into a proton and an electron (β^-) or (b) a proton splits into a neutron and a positron (β^+). γ rays are electromagnetic radiation identical to X-rays but differing in their origins; γ rays emanate from the nucleus whilst X-rays are derived from outer electrons moving to inner orbits and in the process emitting characteristic spectral lines. The energy range for γ rays is generally considered to start at about 0,1 MeV. Because γ rays are electrically neutral and have no mass, they do not interact with matter as readily as α or β particles and thus have a greater range of penetration in Earth materials. This makes them the principal form of radiation detected in geophysical surveys.

γ rays have a range of ~ 30 cm in rock and ~ 60 cm in soil but are completely stopped by ~ 1,5 m of water. Hence γ ray surveys only tell us about a very thin layer close to the surface of the Earth. However, 100 m of air will only absorb about half of the γ ray flux, so atmospheric absorption can generally be ignored in ground surveys (Milsom, 1989).

5.2.2 Natural gamma rays

All rocks and soils are radioactive to varying degrees. The three major sources of gamma rays are potassium (K), uranium (U) and thorium (Th). The γ emitted from K decay is measured directly, whilst U and Th are identified by the γ emission from one of their respective daughter products, assuming that all the radioactive daughters in the series have built up to a constant number (i.e. secular equilibrium) and that the system has not been disturbed. Table 5.1 shows the radioactive decay series of these isotopes.

Table 5.1 The radioactive series of uranium, thorium and potassium (after Milsom, 1989).

Parent	Mode	Daughter	Half-life	γ energy (MeV) and % yield[1]
^{238}U	α	^{234}Th	4.5×10^{9}yr	0.09(15) 0.6(7) 0.3(7)
^{234}Th	β	^{234}Pa	24.1 day	1.01(2) 0.77(1) 0.04(3)
^{234}Pa	β	^{234}U	1.18 min	0.05(28)
^{234}U	α	^{230}Th	2.6×10^{5}yr	
^{230}Th	α	^{226}Ra	8×10^{4}yr	
^{226}Ra	α	^{222}Rn	1600 yr	0.19(4)
^{222}Rn	α	^{218}Po	3.82 day	
^{218}Po	α	^{214}Pb	3.05 min	
^{214}Pb	β	^{214}Bi	26.8 min	0.35(44) 0.24(11) 0.29(24) 0.05(2)
^{214}Bi	β	^{214}Po	17.9 min	2.43(2) 2.20(6) 1.76(19) 1.38(7) 1.24(7)*
^{214}Po	α	^{210}Pb	1.6×10^{-4} sec	
^{210}Pb	β	^{210}Bi	19.4 yr	
^{210}Bi	β	^{210}Po	5.0 day	0.04(4)
^{210}Po	α	^{206}Pb	138.4 day	
^{232}Th	α	^{228}Ra	1.4×10^{10} yr	0.06(24)
^{228}Ra	β	^{228}Ac	6.7 yr	
^{228}Ac	β	^{228}Th	6.1 hr	1.64(13) 1.59(12) 0.99(25) 0.97(18) 0.34(11)*
^{228}Th	α	^{224}Ra	1.9 yr	
^{224}Ra	α	^{220}Rn	3.64 day	
^{220}Rn	α	^{216}Po	54.5 sec	
^{216}Po	α	^{212}Pb	0.16 sec	
^{212}Pb	β	^{212}Bi	10.6 hr	0.30(5) 0.24(82) 0.18(1) 0.12(2)*
^{212}Bi	β(66%)	^{212}Po	40 min	1.18(1) 0.83(8) 0.73(10)
	α(34%)	^{208}Tl	97.3 min	
^{212}Po	α	^{208}Pb	0.3×10^{-6} sec	2.62(100) 0.86(14) 0.58(83)
^{208}Tl	β		3.1 min	0.51(25)*
^{40}K	β(89%)	^{40}Ca	1.45×10^{9} yr	
	K(11%)	^{40}Ar	1.17×10^{10} yr	1.46(11)

Notes: 1. Percent yields (shown in parentheses) indicate number, out of each 100 decays, producing photons of energy specified. Some single decay events produce more than one photon.

2. Decay branches which involve less than 10% of a parent element are not shown.

3. Photons of numerous other energies emitted in events marked *.

The abundance of the major radioisotopes are as follows:

Series	abundance
^{238}U	99,3 % of U
^{232}Th	100 % of Th
^{40}K	0,012 % of K

5.2.3 Gamma ray spectrum

The natural gamma ray spectrum (Fig. 5.1) contains several, discrete peaks for each of the U and Th daughters. ^{214}Bi with a γ ray energy, $E_\gamma = 1,76$ MeV and ^{208}Tl with $E_\gamma = 2,61$ MeV are chosen for the U and Th elements respectively.

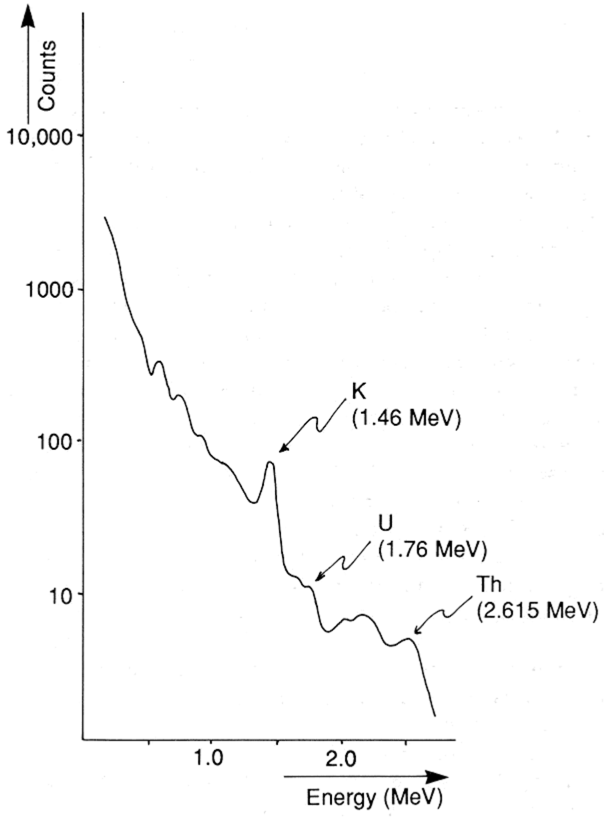

Fig. 5.1 Natural gamma ray spectrum (Milsom, 1989).

The physics of the spectrometer's photomultiplier and detector assembly inhibits ideal discrimination of discrete photopeaks within the spectrum, so energy windows are used to best represent abundances (Table 5.2).

Table 5.2 Energy window widths used by a typical γ ray spectrometer.

Element analysed	Isotope	E_γ [MeV]	Energy window [MeV]
K	^{40}K	1,46	1,36 – 1,56
U	^{214}Bi	1,76	1,66 – 1,86
Th	^{208}Tl	2,62	0,41 – 2,81
Total count (TC)			0,41 – 2,81

Gamma rays are scattered by the photoelectric effect, Compton scattering and pair production. The photoelectric effect is dominant from ~ 0,01 MeV to 0,5 MeV, the Compton effect from 0,1 MeV to ~ 10 MeV and pair production ≥ 1,02 MeV. The dominant Compton effect is due to an incident gamma photon ejecting a bound electron producing an ionised atom and a deflected γ ray of lower energy.

5.2.4 Radioactive content of rocks

U, Th and K are present in varying amounts in all rocks. K is particularly important to geological mapping as it is very widespread. Table 5.3 shows the ranges of the rock classes and major rocks.

Table 5.3 Radioactive concentrations in rocks (adapted from Morse, 1977 and Telford et al., 1990).

Rock	K (%)	U (ppm)	Th (ppm)
Acidic	0,1 – 8	0,1 – 30	0,1 – 250
Basic	0,02 – 3	0,01 – 6	0,03 – 15
Ultrabasic	0 – 1	0 – 1,6	0 – 8
Sedimentary	0,01 – 10	0,1 – 80	0,2 – 350
Metamorphic	0,01 – 6	0,1 – 150	0,1 – 100
Granite	3,5	15	4
Basalts	0,9	2	0,6

The high K content in granites and pegmatites produces a high background which may make it difficult to locate U and Th ores.

5.2.5 Errors in radioactive counting

Radioactive decay is statistical and a series of counts is Poisson distributed. Let *n* denote counts and $\bar{n}$ its mean. If n is large then the Poisson distribution approximates to the Gaussian normal, *G(n)*.

By definition, standard deviation, $\sigma = \left[\frac{\sum d^2}{N-1}\right]^{1/2}$ ………………………. (5.1)

where $d = n - \bar{n}$ and N is the total number of readings.

The probability density function, $\sigma^2 = \int_{-\infty}^{\infty} (\bar{n} - n)^2 G(n) dn$ ……………..…. (5.2)

$$= \int_{-\infty}^{\infty} \frac{e^{-(\bar{n}-n)^2/2\bar{n}}}{(2\pi\bar{n})^{1/2}} (\bar{n} - n)^2 dn \quad \text{………..} \quad (5.3)$$

which by using standard definite integrals leads to

$$\sigma = \sqrt{\bar{n}} \quad \text{………………………………} \quad (5.4)$$

A single sample count n is recorded as $n \pm \sqrt{n}$ giving it a 68 % measure of reliability of lying in the quoted range. The fractional uncertainty of a reading is $\pm 1/\sqrt{n}$, so the higher the counts the better.

Whilst the spectrometer is processing a reading for a given sample time, it cannot make any measurements. This brief time of inactivity is called the *dead time,* τ*,* and the readings have to be corrected to obtain the true count rate, R, calculated from

$$R = \frac{c}{1 - c\tau} \quad \text{...} \quad (5.5)$$

where c is the observed count rate. The dead time is of the order of 5 to 15 μs.

5.2.6 Spectrum or channel interference

Contamination of the lower energy channels by the more energetic gamma rays requires that we 'strip out' these contributions by the use of stripping constants derived from knowing the instrument's calibration factors. The U channel is affected by Compton scattered gamma rays from the Th window and the K channel is affected by Compton scattered gamma rays from the U and Th windows. The Th channel is not affected. Since the instrument's calibration factors were not known, only the Th channel is useful in interpretation together with the total counts if stripping is to be avoided.

5.3 Field Procedures

5.3.1 Instrumentation

The field instrument used was the Geometrics Portable Gamma Ray Spectrometer model DISA – 400A (Fig. 5.2).

Fig. 5.2 The DISA-400 Geometrics spectrometer.

The DISA – 400A transforms incident gamma ray radiation into a visual readout of radioactive intensity from the geology. A sodium iodide crystal (doped with thallium) of diameter 3 inch × 3 inch thick converts gamma rays into flashes of light whose brilliance is proportional to the energy level of the gamma radiation measured. The light flashes are detected by a high gain photomultiplier tube as electrical pulses amplified and fed to pulse height analysers. The analysers will accept pulses between two threshold settings (windows). The accepted pulses are counted and the number stored until presented numerically on a digital display on the instrument front panel (Geometrics operating manual, undated).

5.3.2 Radiometric survey

Before the start of each survey line, a battery check must be done by switching the appropriate switch on the instrument. The spectrometer was then ready for calibration using the supplied ^{137}Cs source and following the simple procedure detailed in the operating manual. Calibration was done daily at the beginning of each line to set the peak readings of the different isotopes to the centre of the window. This was necessary due to the instrument drift caused by voltage supply changes owing to temperature changes. A background count was performed at each line using a thick folded bedding mat but this proved to be a fruitless exercise as it failed to block radiation from the subsurface. The lines surveyed were Kup7 (545135E), Kup8 (546300E), Kup20 (547100E), Kup21 (545500E), Kup22 (545900E) and Kup23 (546700E) at a station spacing of 25 m. On the first line (Kup21) a test run was done at 30 s and 2 minutes sample times to see if the counts changed significantly to justify longer surveys. The longer count rate was chosen for the much higher counts and thus improved counting statistics. Because the terrain was largely flat, the optimum 2π lower halfspace geometry was achieved at almost all the stations except at river banks which could be corrected by the illustrations in Fig. 5.3.

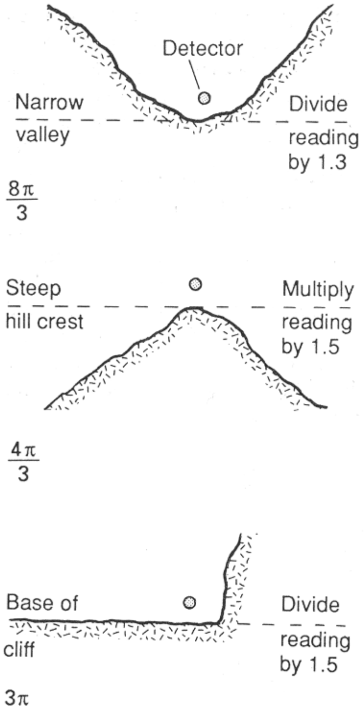

Fig. 5.3 Geometry corrections in radiometric surveys (after Milsom, 1989).

Anthill locations were noted to aid in the interpretation of anomalous values since ants bring up material from deeper down.

5.4 Presentation of results

Since the dead time of the instrument is very small (i.e. 6,14 μs (Mukodzani, 2001)), no dead time corrections were done. The counts over 2 minutes were changed to counts per second (cps). As explained in section 5.2.6, no stripping corrections were applied to the U and K channel data. The radiometric profiles have had their background values removed by subtracting the lowest reading for all the lines. The data is presented as profiles of the Th and total counts (TC) in Figs. 5.4 – 5.15 and as contour maps of the Th and TC in Figs. 5.16 and 5.17. The radiometric data is given in Appendix A.5.

5.4.1 Radiometric profiles

The Th profiles show a general trend of high radioactivity in the southern portions of the lines. However, Kup21 and Kup22 are the exceptions displaying anomalously high central regions (Figs. 5.7 and 5.8 respectively). The amplitudes are typically less than 1 cps giving a percentage error in the counts of 10 %. However in lines Kup21 and 23, the anomaly amplitudes reach 2,3 cps and 3,5 cps respectively, improving the accuracy of the counts. The TC profiles not only give a greater resolution of the anomalies but also give a better accuracy of the counts. Maximum amplitude of 108 cps was attained on Kup8 improving accuracies to less than 1 %. The anomaly shapes are generally a cluster of spikes; however, single peaks such as in line Kup7 and in the north in Kup8 are also observed. The correlation between these anomalies is given as contour maps in 5.4.2. Only three randomly selected lines are described below.

5.4.1.1 Line Kup8 (546300E)

The Th channel (Fig. 5.10) has an anomaly from the beginning of the line at 6850N to 7600N with a peak value attained of almost 1,8 cps. Beyond this anomaly going northwards, the radioactivity level is around 0,8 cps. The TC channel (Fig. 5.11) also shows the anomalous region in the south of the line with a peak value of 108 cps. A spike/single point anomaly exists further north at 8250N and attains just over 90 cps.

5.4.1.2 Line Kup21 (545500E)

A central anomaly is displayed in the Th counts profile (Fig. 5.6) spanning 525 m centred on 7575N. It reaches almost 2,3 cps. The same anomalous region is picked up in the TC profile (Fig. 5.7) with a peak of 100 cps. A secondary peak occurs at 8450N and reaches 87,5 cps.

5.4.1.3 Line Kup23 (546700E)

The Th anomaly occurs from the beginning of the line in the south, rising to almost 3,6 cps above a background of about 1,0 cps (Fig. 5.12). A similar trend is noticeable in the TC profile (Fig. 5.13) whose southern anomaly exceeds 90 cps. Another anomaly is seen towards the end of the line at 8550N and peaks at around 77 cps.

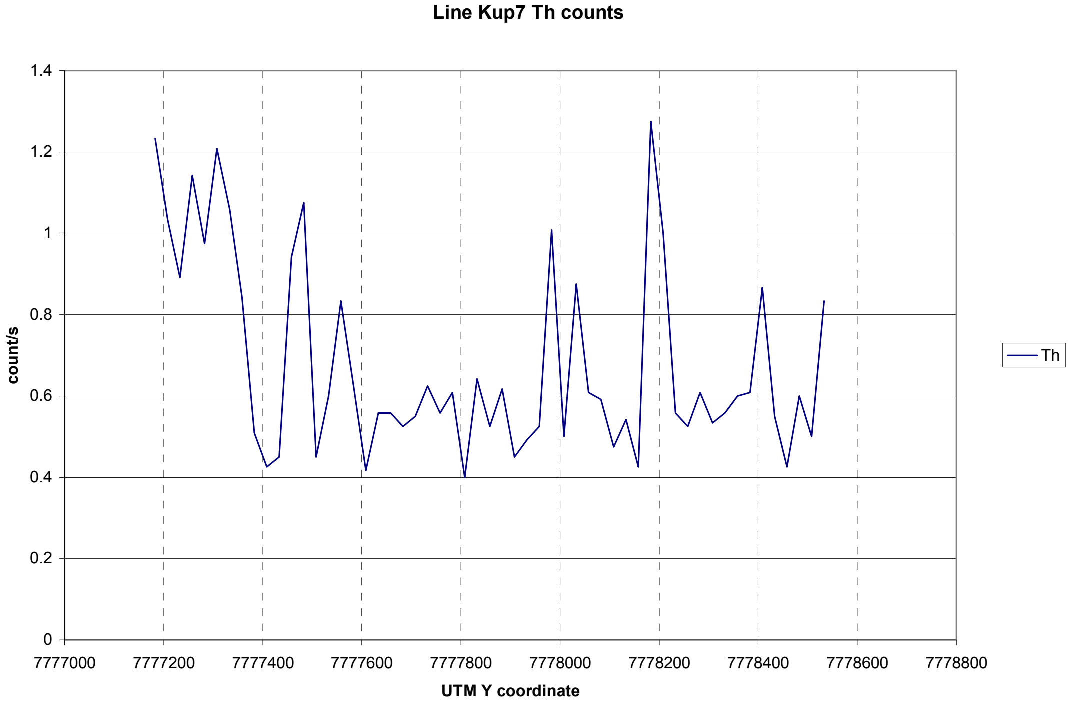

Fig. 5.4 Line Kup7 (545135E) Th channel radiometric profile.

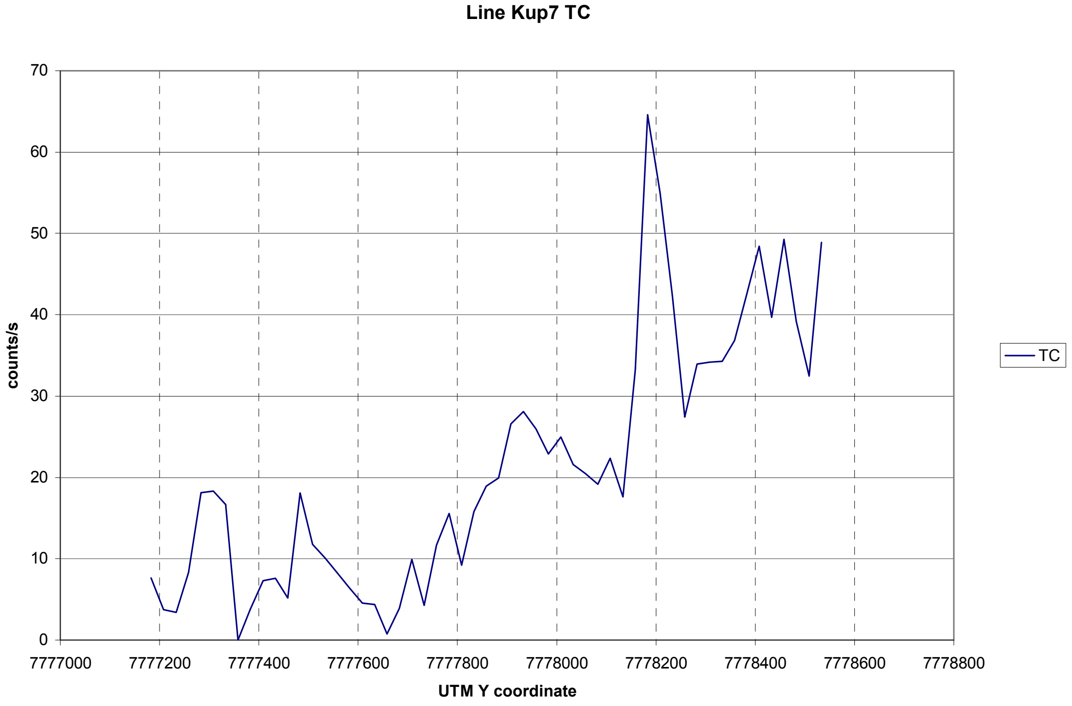

Fig. 5.5 Line Kup7 TC channel radiometric profile.

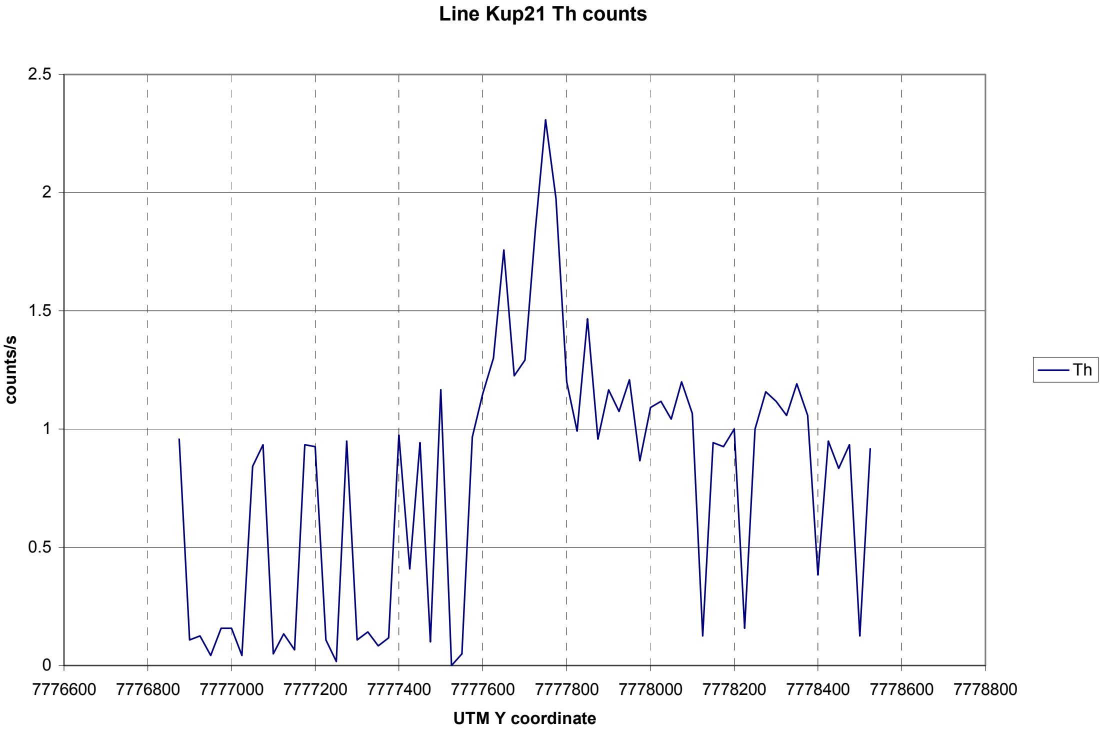

Fig. 5.6 Line Kup21 (545500E) Th channel radiometric profile.

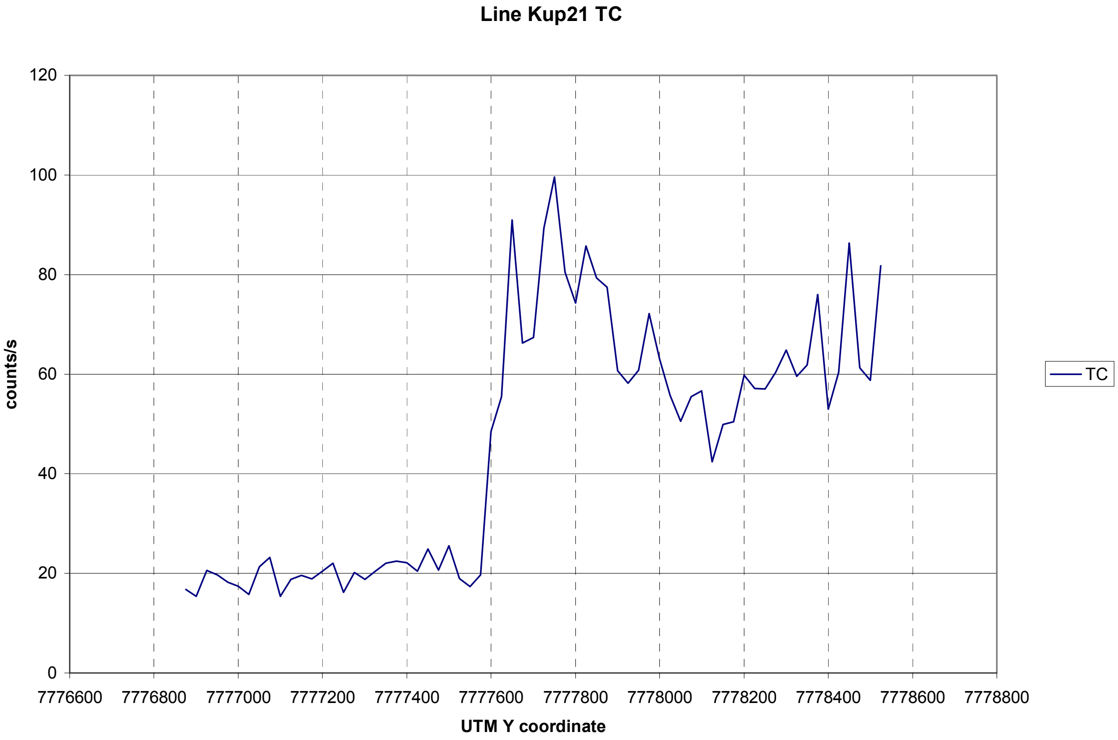

Fig. 5.7 Line Kup21 TC channel radiometric profile.

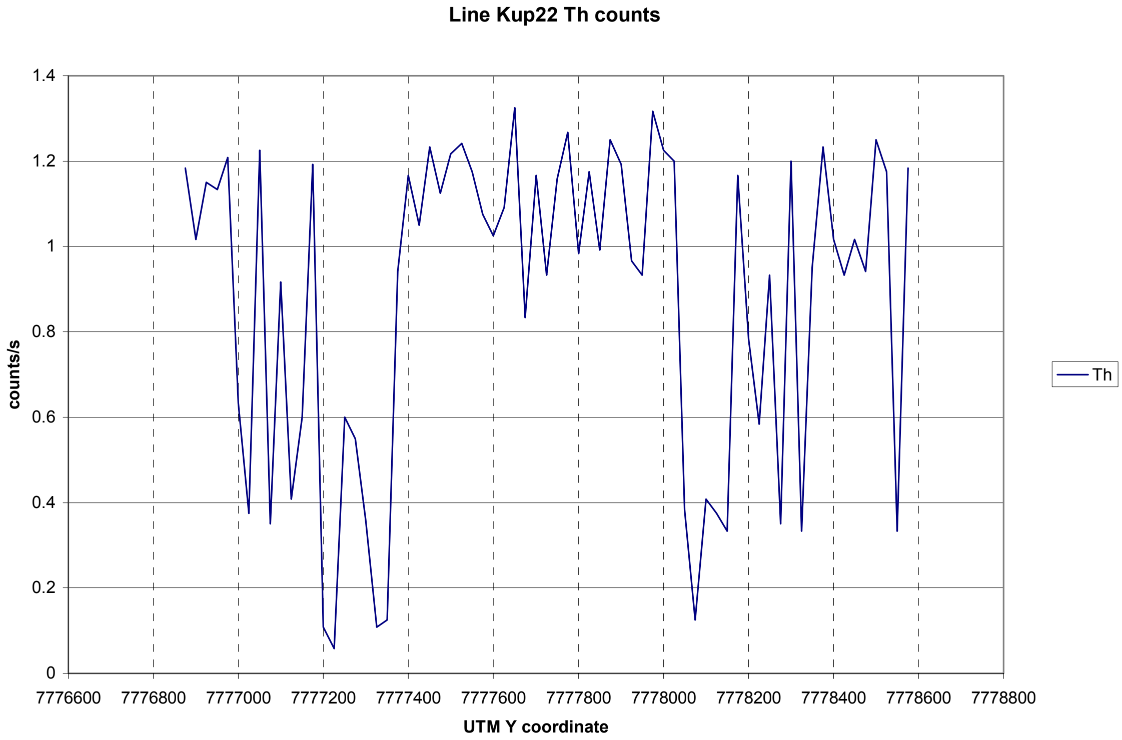

Fig. 5.8 Line Kup22 (545900E) Th channel radiometric profile.

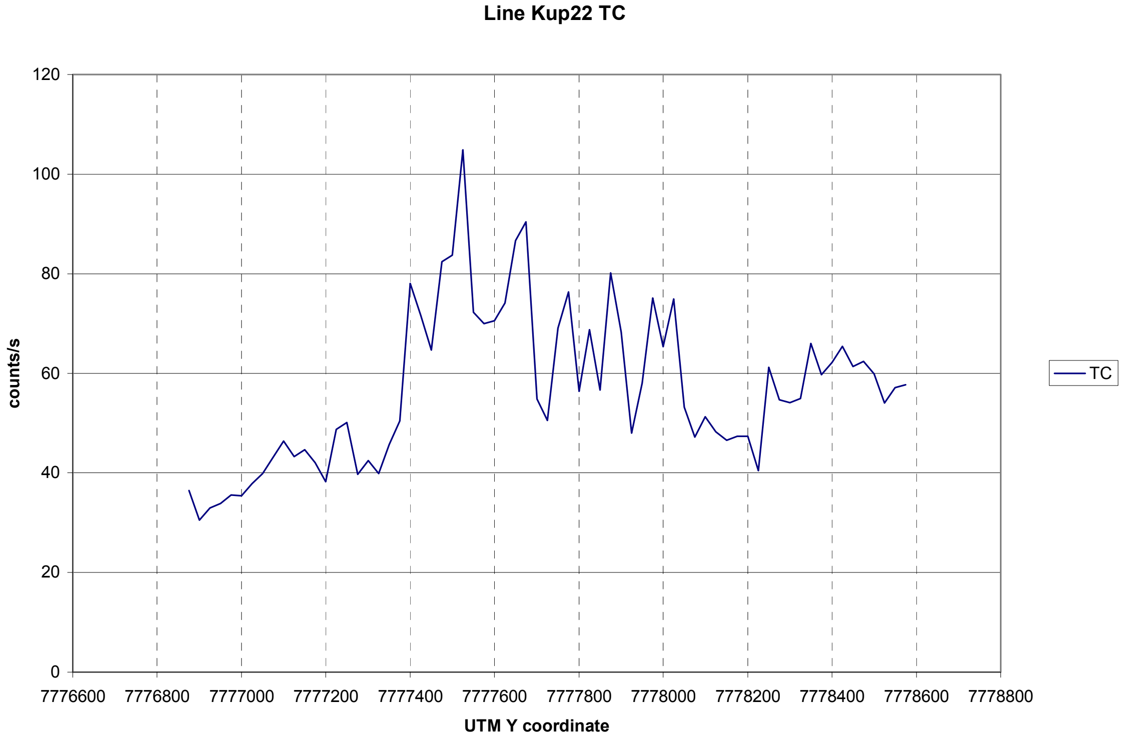

Fig. 5.9 Line Kup22 TC channel radiometric profile.

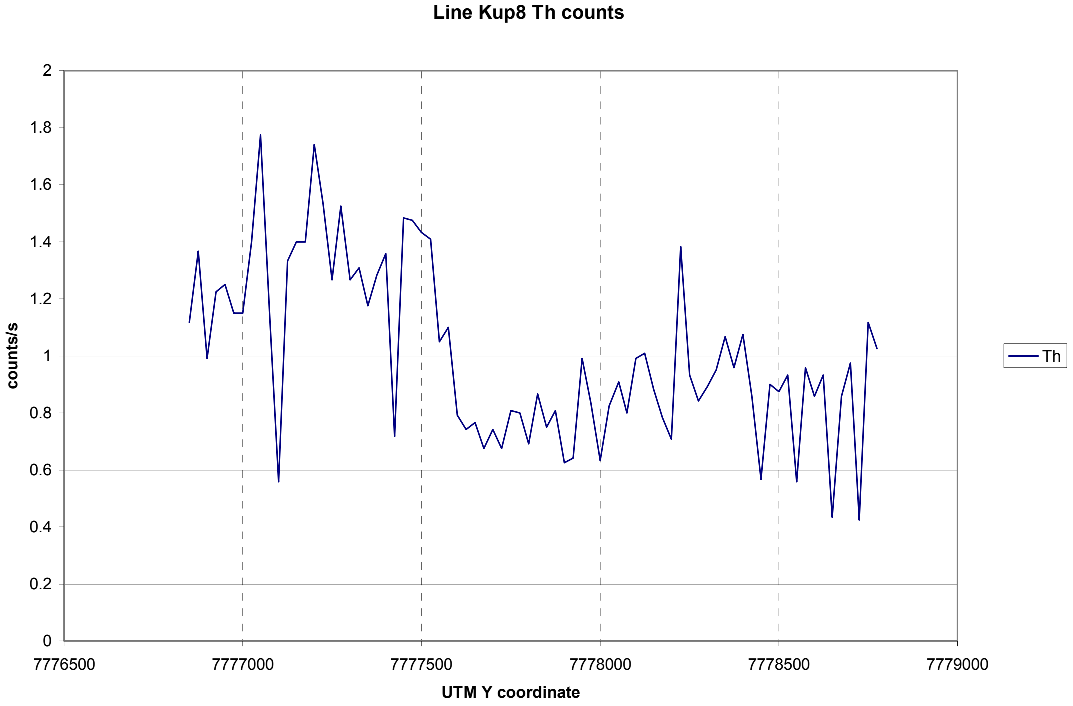

Fig. 5.10 Line Kup8 (546300E) Th channel radiometric profile.

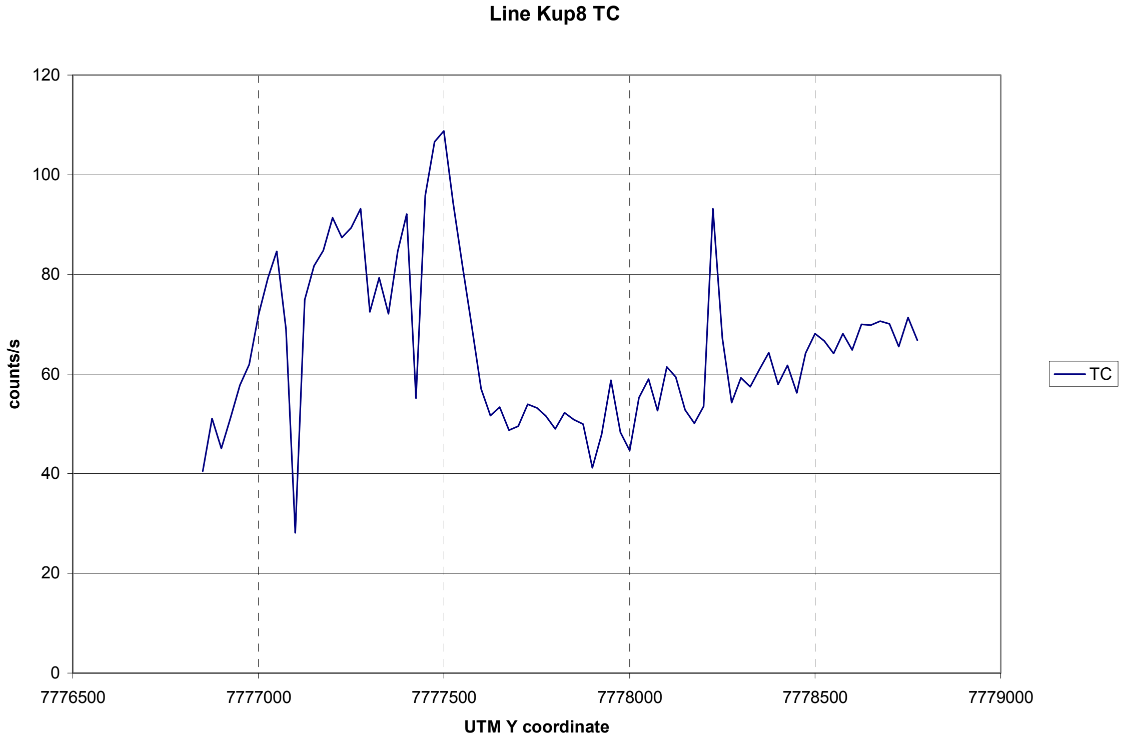

Fig. 5.11 Line Kup8 TC channel radiometric profile.

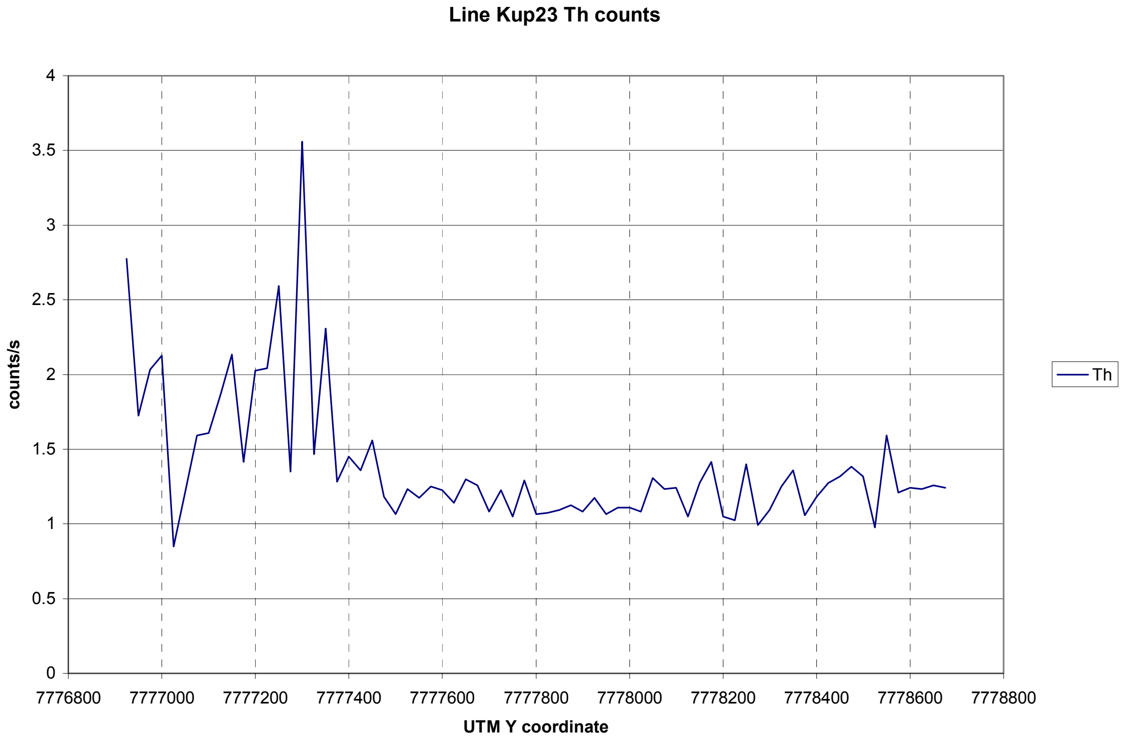

Fig. 5.12 Line Kup23 (546700E) Th channel radiometric profile.

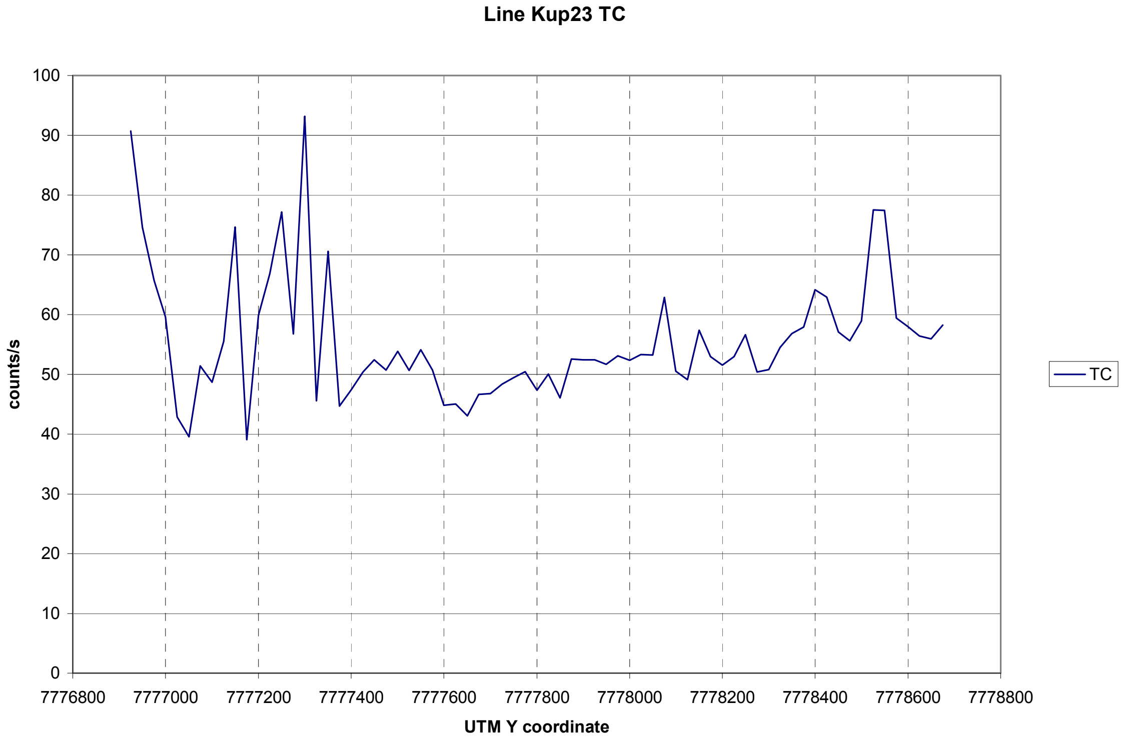

Fig. 5.13 Line Kup23 TC channel radiometric profile.

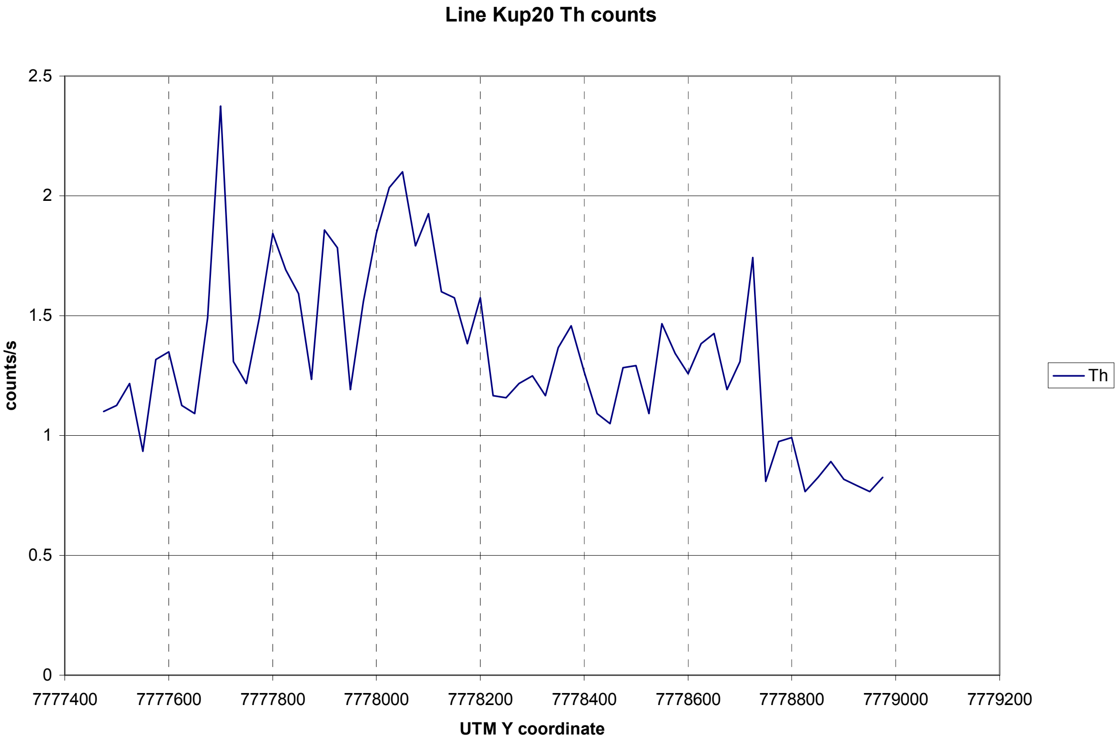

Fig. 5.14 Line Kup20 (547100E) Th channel radiometric profile.

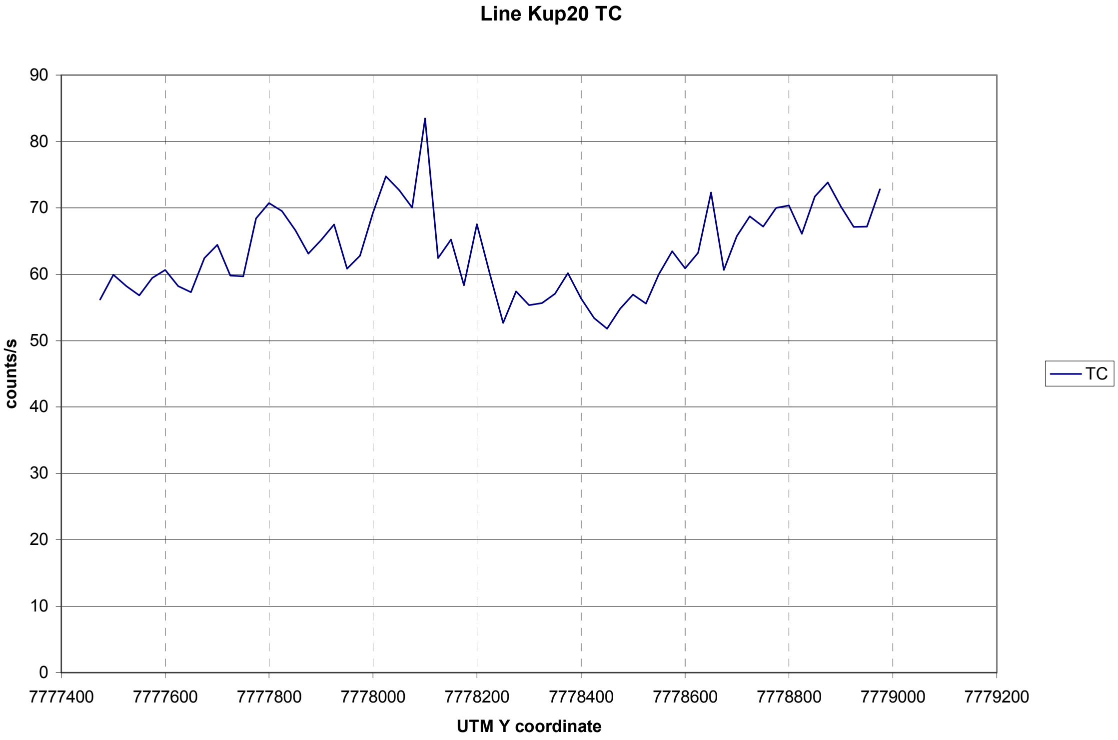

Fig. 5.15 Line Kup20 TC channel radiometric profile.

5.4.2 Contour maps

The Th contour map (Fig. 5.16) reveals an eastern ridge of high values running N – S between UTM eastings 546500E – 547200E (Kup15 – 19). From the SE corner of the map there is an E – W ridge linking the eastern radiometric highs with a central western portion. In the extreme south and north lie E – W striking anomalies.

The TC contour map (5.17) displays a prominent SE – NW trending anomaly flanked on the west by extreme lows forming the background region. In the east, the N – S trending anomaly meets a broad E – W trending anomaly spanning the northern regions of the map. See section 6.2 for a further discussion of the radiometric results.

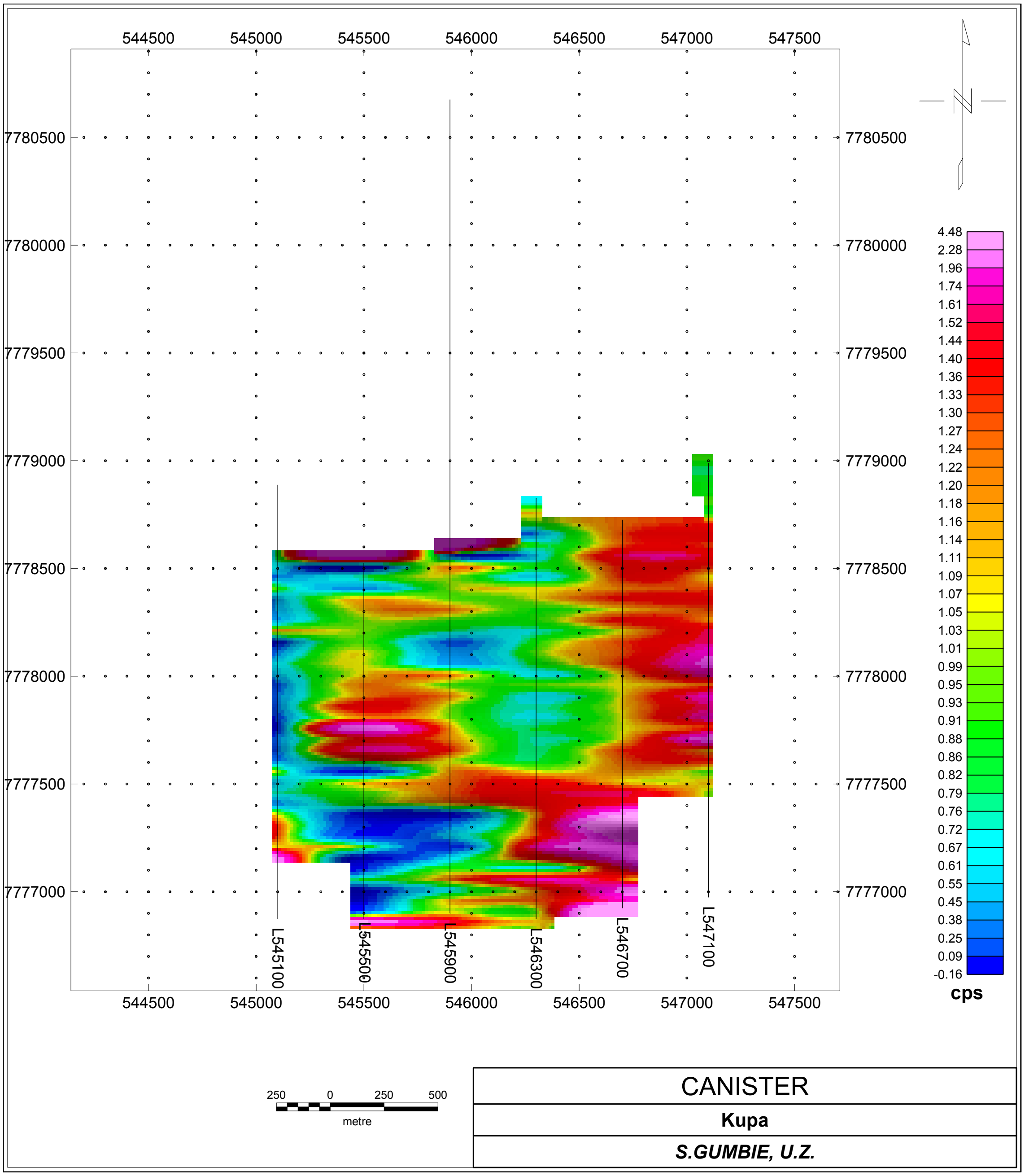

Fig. 5.16 Th counts contour map of the Kupa grid.

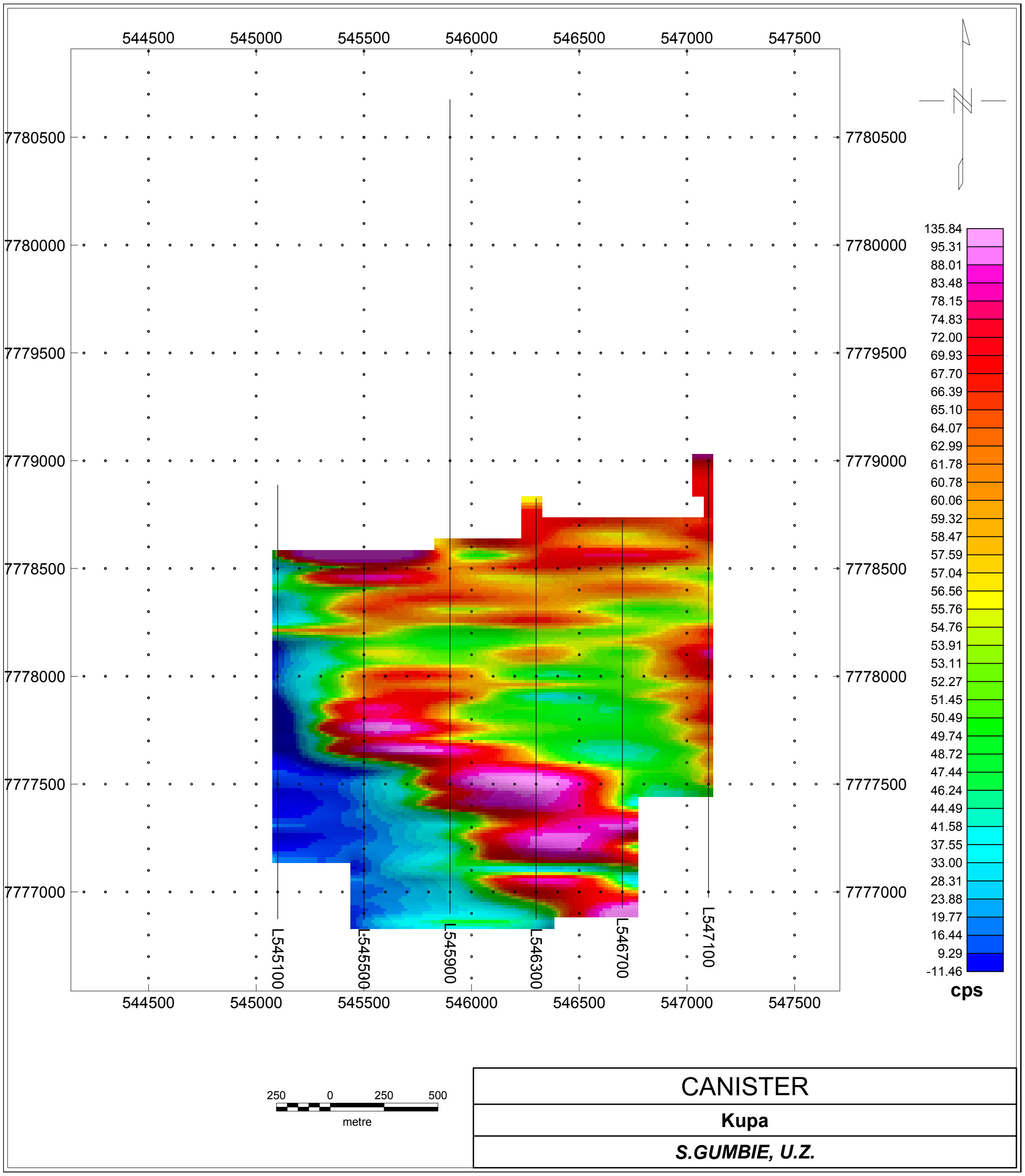

Fig. 5.17 TC contour map of the Kupa grid.

Chapter Six

Further Data Processing, Interpretation, Conclusions and Recommendations

6.1 General

Several other processing techniques can be applied to the data in order to enhance the anomaly shapes and distribution. The ones used in this chapter were obtained from the Geosoft Mapping and Processing System which is software designed to execute digital calculations on gridded earth science data. Only a few selected methods were utilised, chosen on their usefulness for the particular geophysical technique and on the value they added to the data presented in the previous chapters. Potential field modelling programs were also available but were not attempted due to time constraints.

For the interpretation of the anomalies, the rudimental geology map (Fig. 1.16) was used in addition to the regional geology described in Chapter One. Since drilling had just started with results not yet available, the interpretations presented here, should be checked against the drilling information once available.

6.2 Gravity results

The only further data enhancing technique used was removing a first order surface trend calculated using the data points from the grid edges. This is done by a Geosoft program that calculates a least squares surface fit to the values along the edge of the grid. However, a trade-off between choosing a low order surface regional as opposed to a higher order one had to be struck; low order surface trends lose some of the anomaly to the regional whilst higher order surfaces mix the anomaly with the surface fit (Telford et al., 1990). A first order regional surface was chosen on the basis of the linear regional that could be fitted on the long line (Kup13).

Compare Fig. 2.18 with Fig. 6.1. The dense feature runs through the central part of the grid in a NE – SW trend. It lies over the inferred greenstone and could suggest a refinement to the proposed geology by deducing that the mapped body has a similar trend to that of the gravity. From table 2.1 in section 2.7, the likely lithology is a diorite with an average density of 3 016 kg/m^3, however, metabasalts of average density 2 970 kg/ m^3 were seen outcropping in the area (see Fig. 1.10). This is likely to be against a granite country rock as granites have been mapped both in the north and south of this locality. The dense structure lies adjacent to the main magnetic anomaly but to its north and coincides with the weaker magnetic anomaly 'ridge' which would correlate well with the magnetic nature of basic rocks.

The longest profile, Kup13 which has a reasonable regional gravity defined, was used to estimate some parameters of the causative body, e.g. depth to top, dip and density contrast. A sloping regional was fitted by hand and removed to get the residual gravity values (see Fig. 6.2).

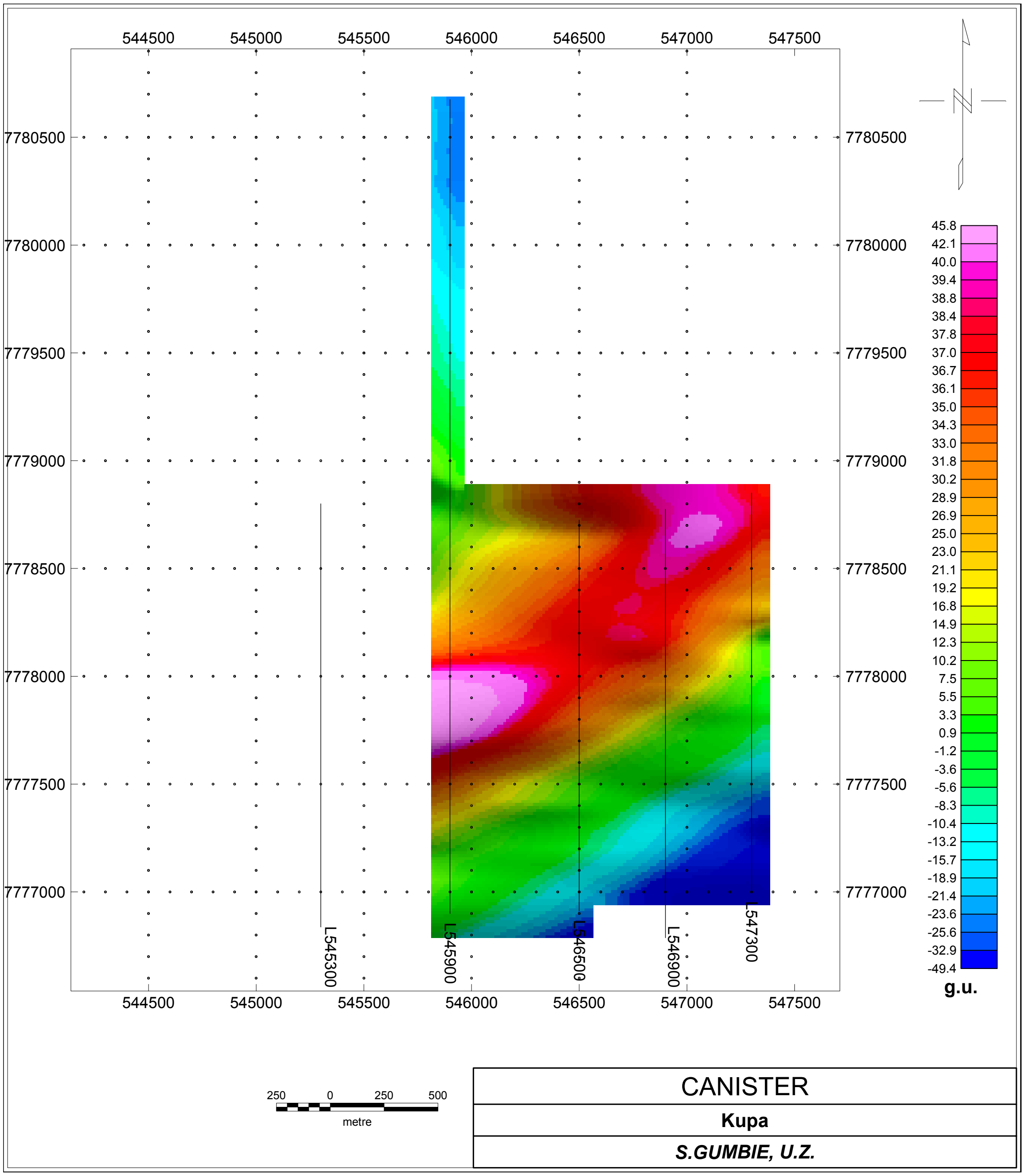

Fig. 6.1 First order trend removed gravity map.

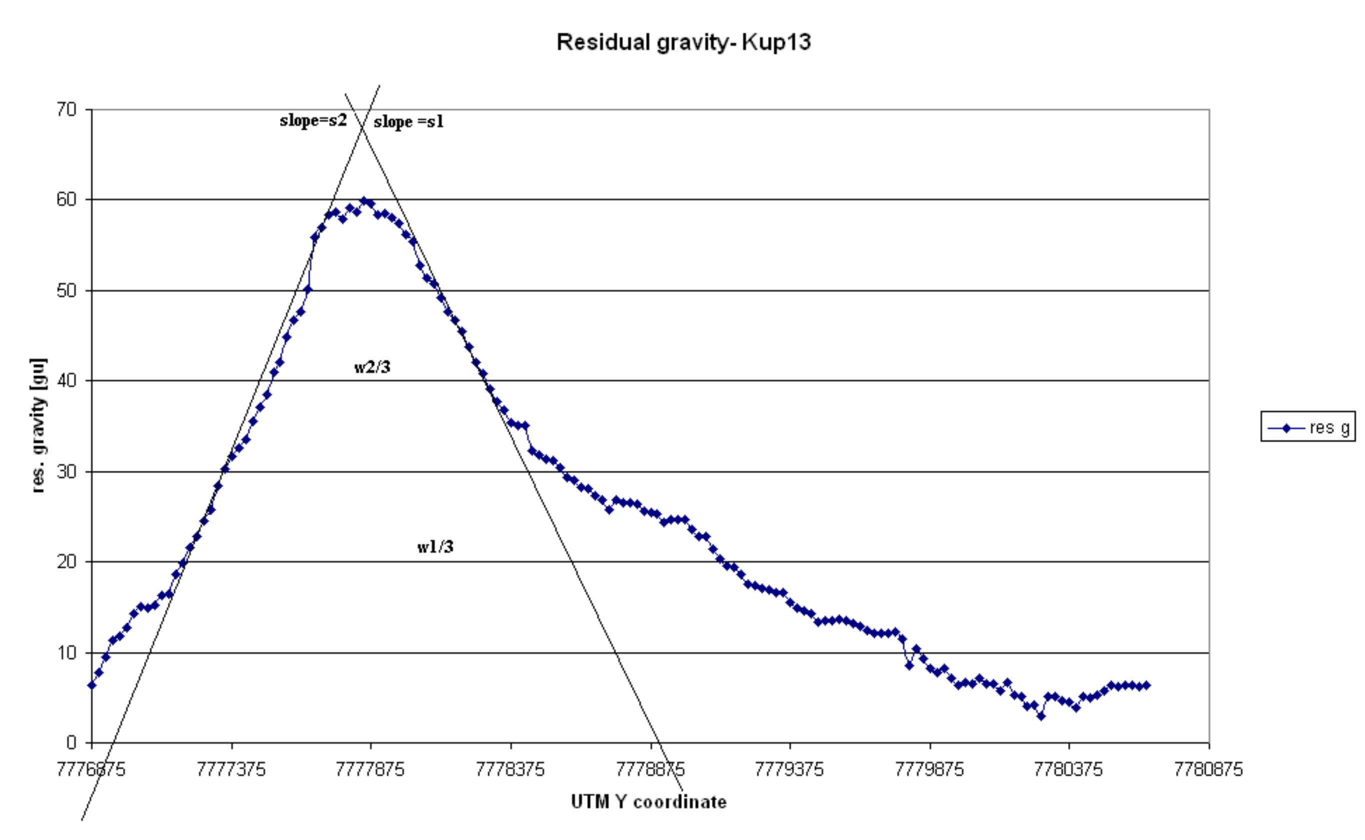

Fig. 6.2 The gravity anomaly of line Kup13 after the removal of a linear regional.

Using the ribbon model to represent a thin dyke of limited extent (Grant and West, 1965) and characteristic curves, the calculated depth to the top of the body is 246 m with a dip of 84º N. It has a strike length of 1 830 m, a down-dip width of 3 051 m and a density-thickness product of 3,09 x 10^5 kg/ m^2. The density-size ambiguity is fundamental to all inverse-potential solutions and so assuming a thickness of 100 m gives us a density contrast, $\Delta\rho$, of 3 090 kg m^{-3}. The information used to obtain these parameters is presented in Table 6.1 below.

Table 6.1 Parameters obtained in the graphical determination of depth, dip, strike, width and density-thickness product from the gravity anomaly.

Gravity anomaly	$\Delta g_{\max} =$ 59,8345 g.u.
Slopes	$s_1 =$ 0,07695 g.u./m $s_2 =$ -0,06492 g.u./m
Widths	$w_{2/3} =$ 776,9 m $w_{1/2} =$ 2 130,2 m (along strike) $w_{1/3} =$ 1 935,0 m
Depth to top	246,3 m
Dip	84,3° N
Width	3 050, 7 m
Strike	1 830,4 m
Density-thickness product	$\Delta\rho\, t = 3{,}09 \times 10^5$ kg/m^2

6.3 Magnetic Results

6.3.1 Further processing

The additional maps used to interpret the total magnetic field anomaly are the trend removed, analytical signal, reduction to the pole, first vertical derivative map and radially averaged power spectrum (Figs. 6.3 – 6.7). In some surveys, the IGRF is subtracted from the total field measurement by using maps of known variations of the parameters and extrapolating to the survey positions, however, this was not done for this project since the area is small.

6.3.1.1 Trend removed map

In section 3.6.1 linear regionals were used in describing the profiles and so a first order surface trend was removed from the total field data (Fig. 6.3). It is similar to the total field map (Fig. 3.29) described in section 3.6.2 but enhances the appearance of the anomalies particularly in the NE. However, it seems to reduce the anomaly in the west. A zone of magnetic highs is clearly visible striking WSW - ENE.

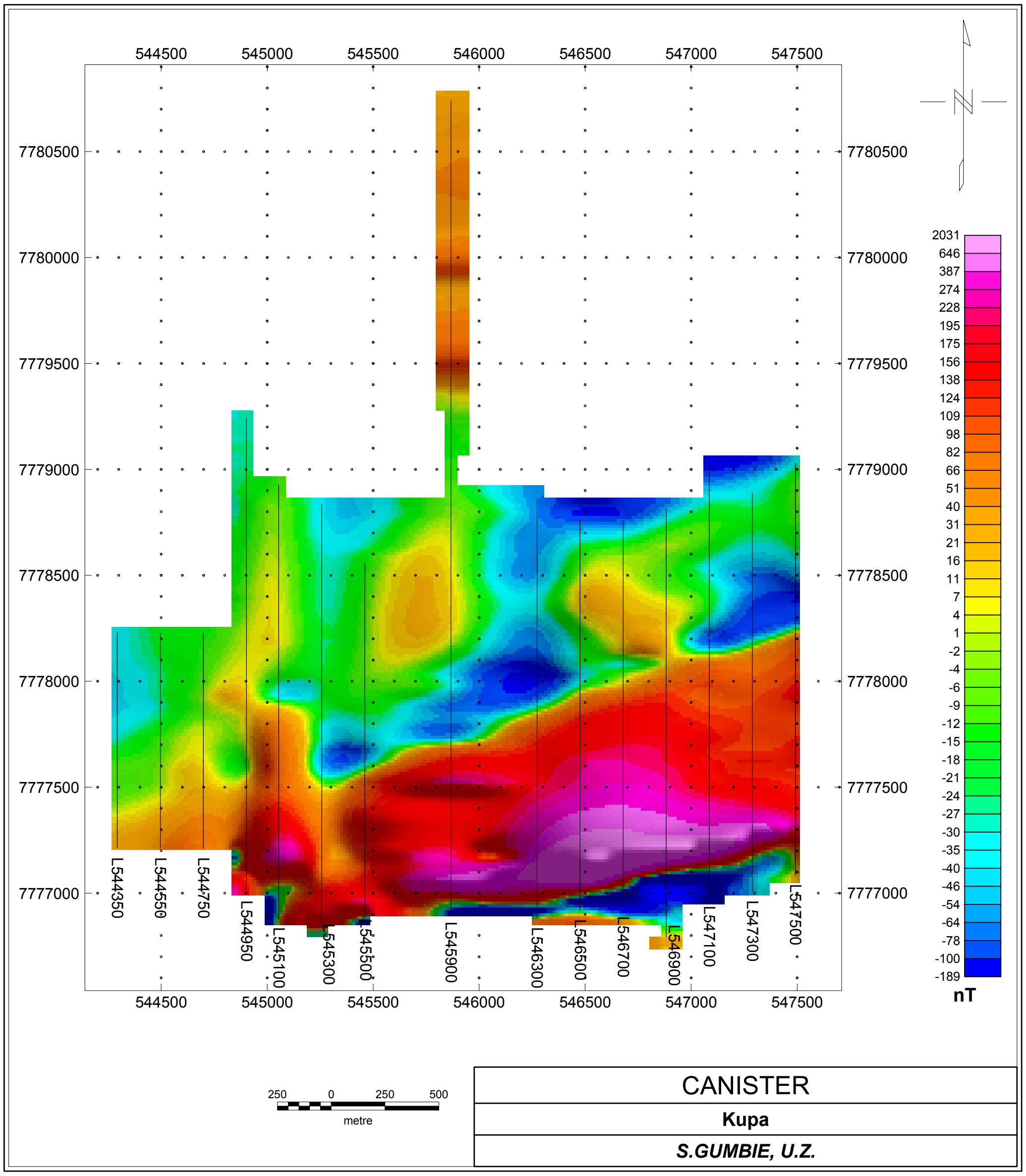

Fig. 6.3 First order surface trend removed total magnetic field map.

6.3.1.2 First vertical derivative

This technique amplifies short–wavelength information, i.e. shallow depth features. Fig. 6.4 elongates the main anomaly and brings out more medium magnetic 'reliefs'; two to the north and east of the grid are sub-parallel to the main magnetic high feature and two in the north and west run north – south.

6.3.1.3 Reduction to the pole

This operation changes the actual inclination to the vertical removing any asymmetries caused by a nonvertical geomagnetic regional field and simplifying the anomalies to interpret (Dobrin and Savit, 1988). This means that the causative body is placed at the magnetic pole where the field lines are vertical. Therefore, it also places the magnetic anomaly more central to the causative body allowing for easier comparison with gravity maps. Fig. 6.5 is similar to the total field map but is more resolved, showing an E – W magnetic high about 350 m wide on the southern edge of the map and two zones of weaker magnetic values sub-parallel to the magnetic high but further north. A prominent 'deep' magnetic low with the same trend as the high anomaly runs through the central regions of the map and is as much as 400 m wide and 2,5 km long.

6.3.1.4 Analytical signal map

The analytic signal is formed through a combination of the horizontal and vertical gradients of a magnetic field (Blakely, 1996). For the three dimensional case, the analytic signal is given by

$$A(x,y,z) = \sqrt{\left(\frac{\partial B}{\partial x}\right)^2 + \left(\frac{\partial B}{\partial y}\right)^2 + \left(\frac{\partial B}{\partial z}\right)^2} \quad \ldots\ldots\ldots\ldots\ldots \quad (6.1)$$

where $B(x,y,z)$ is the total magnetic field strength.

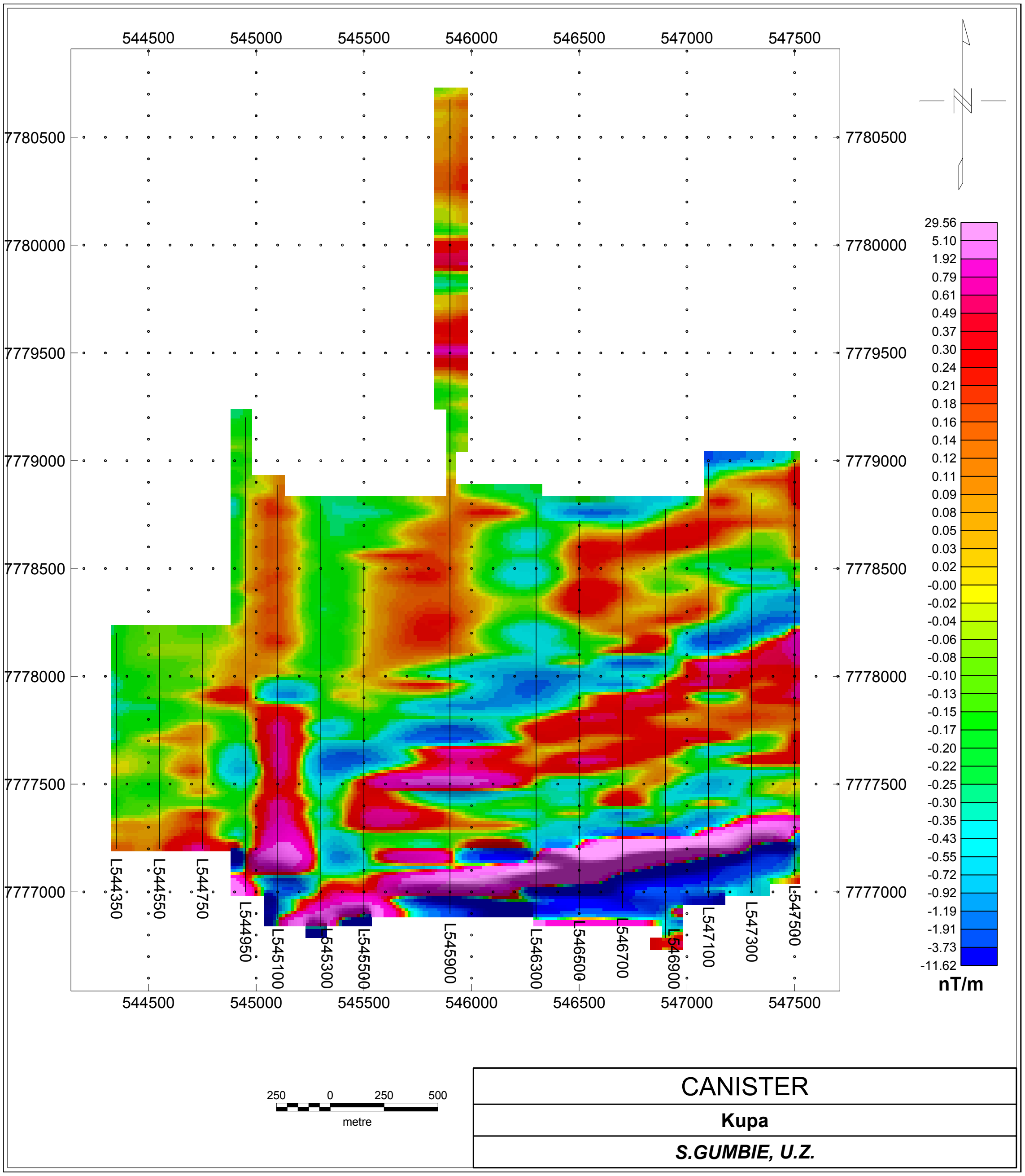

Fig. 6.4 First vertical derivative map.

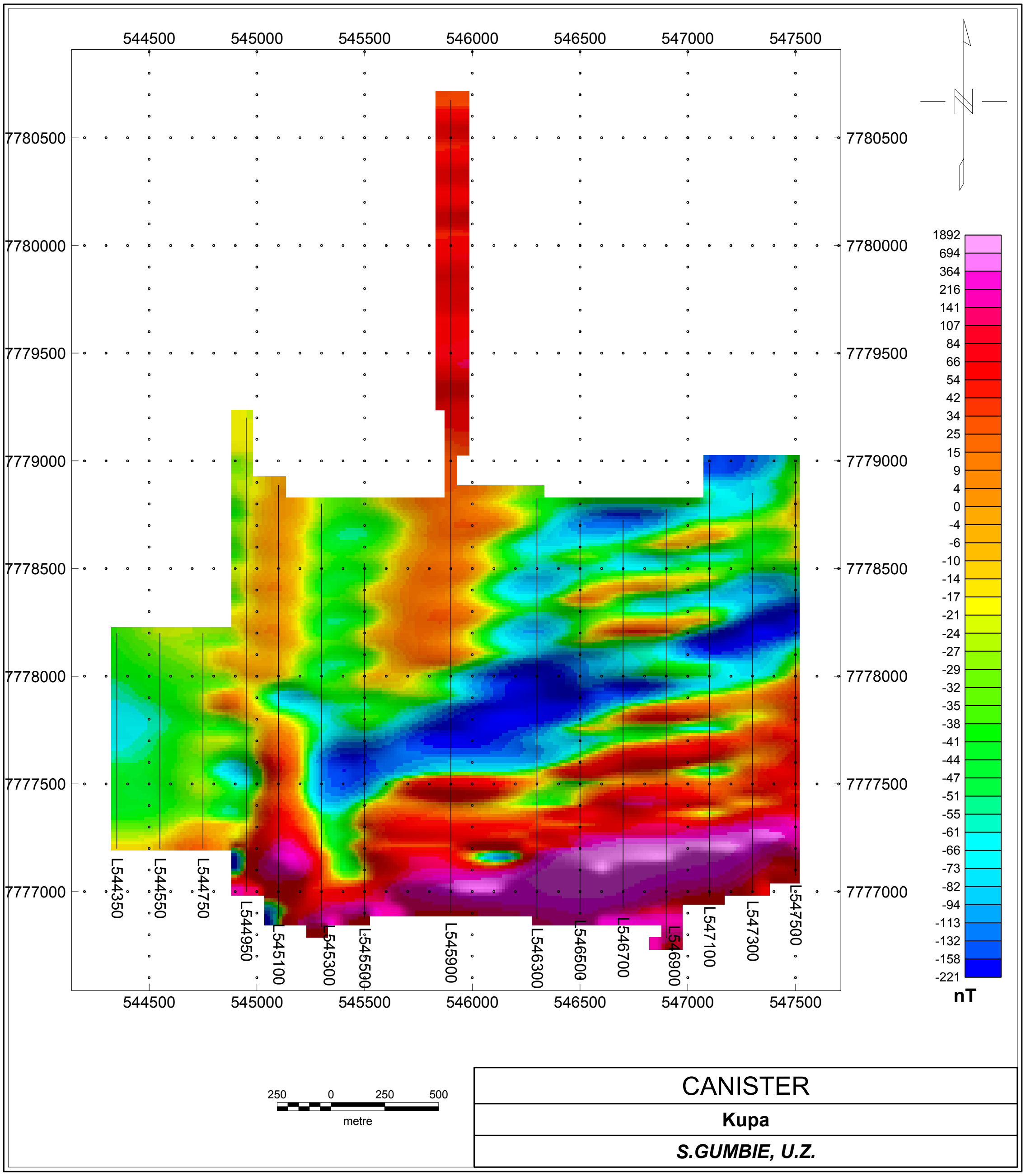

Fig. 6.5 Magnetic reduction to the pole map.

This is done digitally in the Geosoft software by performing a Fast Fourier Transform algorithm where the horizontal derivatives $\partial B / \partial x$ and $\partial B / \partial y$ are calculated as gradients of the gridded total field data. The first vertical derivative $\partial B / \partial z$ is computed by performing an upward continuation.

The analytic signal has a form over causative bodies that depends on the locations of the bodies and is independent of the direction of magnetisation. Fig. 6.6 shows the magnetic features to be better defined than on the total field map (Fig. 3.29). There is another anomaly trending sub-parallel and to the north of the main magnetic feature. In the north – eastern section of the map a shorter anomaly of similar trend to the southern anomalies is seen.

6.3.1.5 Radially averaged power spectrum

The magnetic map is a superposition of the response of several magnetic sources at different depths, each with a characteristic amplitude and wavelength (λ). The Fourier transform amplitudes, $A(\lambda)$, when squared give the energy or power (P). Thus a 2D Fourier analysis of the magnetic grid data can be represented graphically as a radially averaged plot of the power against the radial wavenumber (γ). The wavenumber is the inverse of the wavelength and is given by

$$\gamma = \sqrt{\alpha^2 + \beta^2}\,, \quad \ldots\ldots\ldots\ldots\ldots\ldots\ldots\ldots \quad (6.2)$$

where $$\alpha = \frac{1}{\lambda_x} \quad \ldots\ldots\ldots\ldots\ldots\ldots\ldots\ldots\ldots \quad (6.3)$$

and $$\beta = \frac{1}{\lambda_y}. \quad \ldots\ldots\ldots\ldots\ldots\ldots\ldots\ldots\ldots \quad (6.4)$$

α and β are horizontal wavenumbers whilst λ_x and λ_y are the wavelengths in the x and y directions respectively.

The Fourier amplitude spectra of magnetic (and gravity) anomalies due to geological bodies tend to be dominated by exponential terms of the form $e^{-2\pi\gamma z}$ where z is the depth to the top of the source. For example, a geologic province with two groups of sources at average depths $\overline{H}$ and $\overline{h}$, the power is given by

$$P = (A_1 + A_2)^2 = (Be^{-2\pi\overline{H}\gamma} + be^{-2\pi\overline{h}\gamma})^2 \quad \ldots\ldots \quad (6.5)$$

where $$A_1 = Be^{-2\pi\overline{H}\gamma} \quad \ldots\ldots\ldots\ldots\ldots\ldots\ldots\ldots\ldots\ldots\ldots \quad (6.6a)$$

and $$A_2 = be^{-2\pi\overline{h}\gamma} \quad \ldots\ldots\ldots\ldots\ldots\ldots\ldots\ldots\ldots\ldots\ldots \quad (6.6b)$$

A plot of log(P) versus wavenumber would give two straight line segments with the slopes s_1 and s_2 related to $\overline{H}$ and $\overline{h}$ as follows:

$$s_1 = -4\pi\overline{H} \quad \ldots\ldots\ldots\ldots\ldots\ldots\ldots\ldots \quad (6.7a)$$

$$s_2 = -4\pi\overline{h} \quad \ldots\ldots\ldots\ldots\ldots\ldots\ldots\ldots \quad (6.7b)$$ (Spector and Parker, 1979).

B and b are obtained from the intercepts of the log(P) versus γ graph.

This analysis decomposes the magnetic map data into groups of individual magnetic sources at similar depths and is particularly useful for the separation of anomalies due to shallow and deep sources.

The data was gridded at a 25 m cell size giving a Nyquist wavenumber of 20 km^{-1} as shown on Fig. 6.7. Three slopes were fitted on Fig. 6.7 suggesting the existence of 3 groups of magnetic sources. From calculations using equation (6.7(a) and (b)) the depths to the sources were found to be 24 m, 90 m and 247 m after subtracting the sensor height of 2 m (Fig. 3.9).

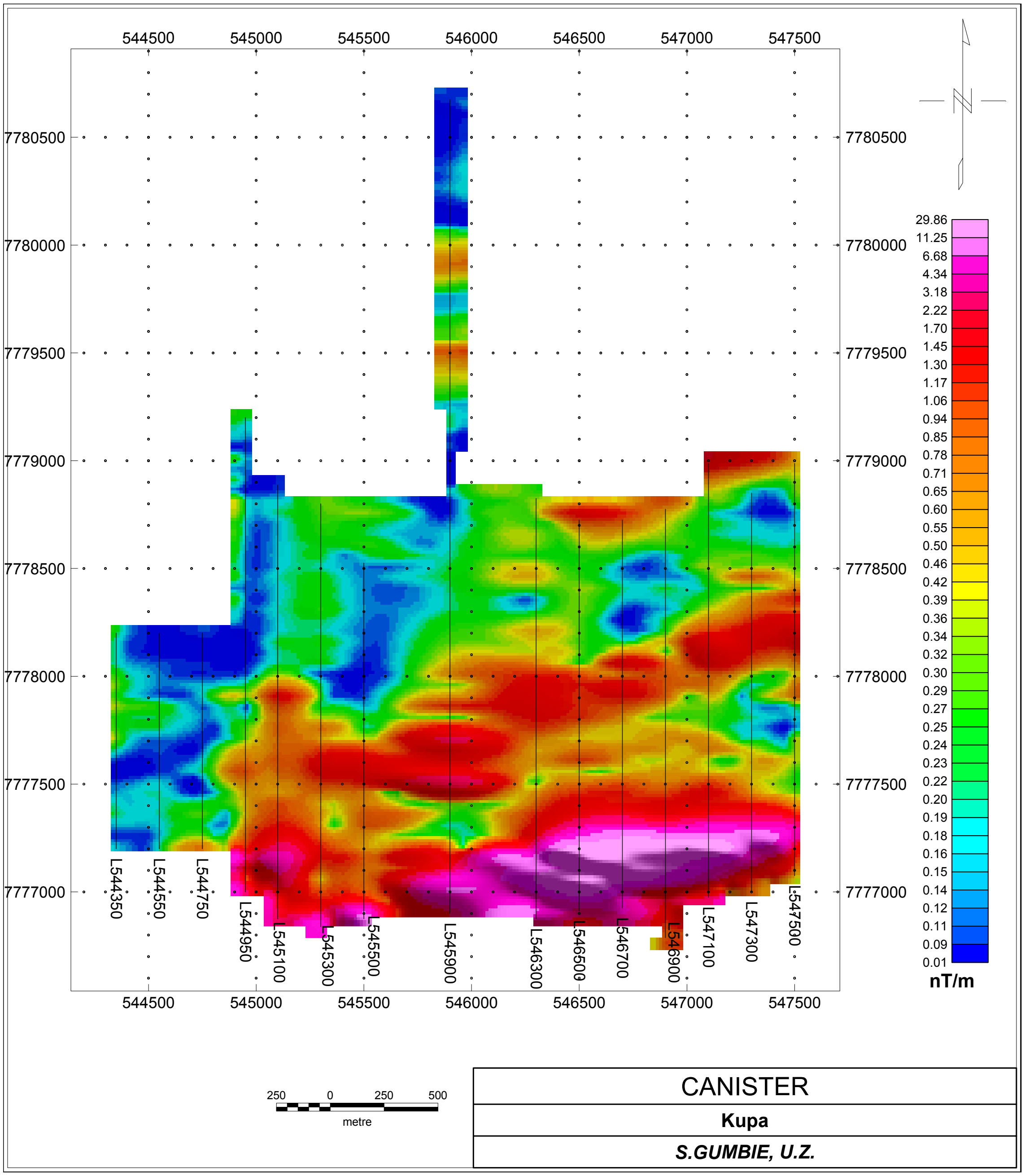

Fig. 6.6 Magnetic analytical signal map.

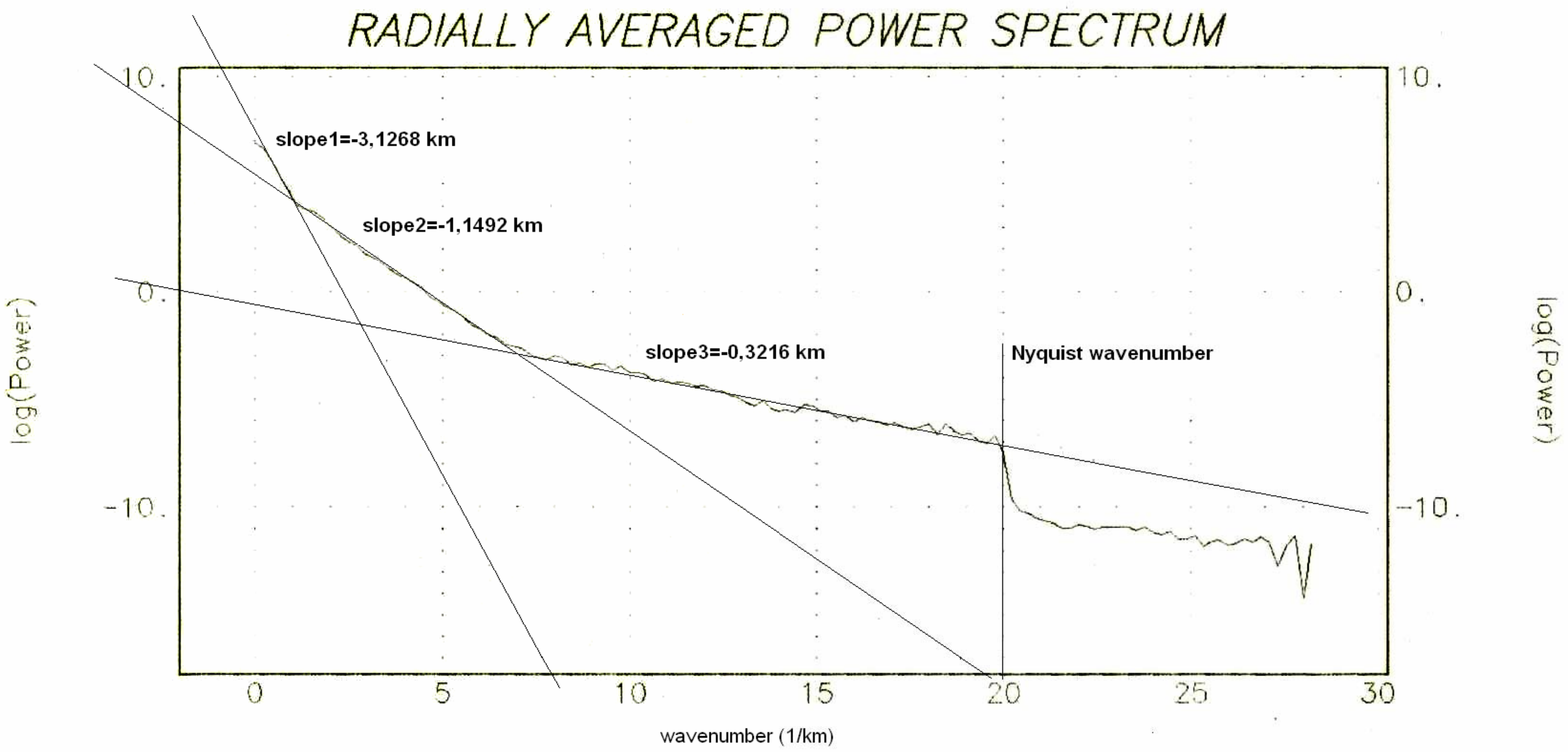

Fig. 6.7 Radially averaged power spectrum.

6.3.2 Interpretation

The E-W magnetic high anomaly lies over the southern part of the inferred buried greenstone body from the local geology map (Fig. 1.16). This could be interpreted as a massive sulphide body or a lenticular banded ironstone formation (BIF) forming the southern part of the greenstone belt but needs more geophysical information to further distinguish between the two. The analytical signal map supports the BIF interpretation by resolving another parallel feature suggesting a stratigraphic sequence, possibly a metasedimentary layer in the greenstone sequence. The first vertical derivative map further confirms the strike of the possible bedding shown in the analytic map and suggests that it is at shallow depth. Therefore, by the shallow magnetic depth estimate, the causative body lies at around 90 m below the surface.

6.4 IP results

Only pseudosections were produced for the IP survey (Figs. 4.9 - 4.14) though contoured maps for the various ‘depth slices’ n = 1 to 6 would have improved the presentation of the results for ease of interpretation. Edwards (1977) gives a median depth of investigation, $z_e = 0{,}519a$ for n = 1 and $z_e = 2{,}478a$ for n = 6. Since a = 50 m this translates to a depth of investigation of about 26 m for n = 1 and about 124 m for n = 6. These depths apply to Wenner, Schlumberger and pole - dipole arrays. A qualitative analysis shows that both high chargeabilities coinciding with high resistivities and high chargeabilities with low resistivities are present on the lines. High chargeability and high resistivity is an indicator of disseminated sulphides, however, these parameters can also be of halos around massive sulphide bodies which have a high chargeability, low resistivity signature (Milsom, 1989; Kearey and Brooks, 1988). Although clays and graphites may exhibit similar patterns, consideration of the other geophysical methods and the geochemistry suggest a metalliferous source.

The IP anomaly on line Kup21 (Fig. 4.9) lies within the greenstone belt depicted on Fig. 1.16. This chargeable, conductive feature occurs from surface to a relatively shallow depth (n = 3) but could just be the clay soils around the Chamata river. The ‘pants leg’ shape to this anomaly suggests a shallow horizontal surface feature. However, the southern anomaly seems to be coincident with the BIF (inferred from magnetic anomaly). Further to the east, on line Kup15 (Fig. 4.10), this pattern seems to be repeated whereby the southern anomaly picks up the BIF. On this line, the southern anomaly is more prominent and could be the massive sulphide body inferred from the ground magnetics, HLEM and geochemistry results. This pattern persists to the other lines to the east (Kup17 and 20) with varying degrees of clarity. It is generally noticed that the IP anomalies consistent with massive sulphides exist in the northern portions of the lines whereas in the southern portions a disseminated sulphide occurrence is dominant, with the notable exception being line Kup21.

6.5 Radiometric results

No further processing was done on the radiometric data presented in section 5.4. The interpretation of radiometric anomalies depends upon several factors that affect the transmission of natural gamma rays to the surface. These are the depth of unconsolidated cover, slope, soil moisture and vegetation. The surveys were done in near ideal conditions of low soil moisture, flat ground and clear field lines. So the anomalies correlate to soil types, depth to bedrock and possibly geological structure.

The TC contour map (Fig. 5.17) shows that the SE – NW trending anomaly ‘ridge’ coincides with the course of the Chamata river and the deep clay soils of its banks. Clay contains potassium minerals which are probably responsible for the high signature. The
E – W trending highs in the northern portion of the map could indicate a very shallow depth to a granite bedrock underneath the Kalahari sands as suggested on the local geology map. It was noted during the radiometric surveys that the northern portion of the map beyond the local river systems tended to have sandy soils high in silica content

which supports the idea of the underlying granite. Besides outcrops in the river beds, no other granite outcrops were seen and so this suggestion is debatable. The northern trending anomaly in the east correlates to a stream in the Chamata river braid as seen on Fig. 1.16.

6.6 Correlation of anomalies

The magnetic, gravity and IP methods all show similar trends which are generally consistent with the geological strike of the rock outcrops seen in the grid and inferred from the geophysical results (Fig. 6.8). The radiometric method seems to have just mapped the clay soils along the Chamata river system. However, the northern radioactive anomaly may have mapped the granite – greenstone boundary with the highs over the granites suggesting a thin overburden. The gravity anomaly is offset on average by about 500 m to the north of the magnetic anomaly whilst the IP anomalies coincide with the magnetic anomaly in the south and the southern edge of the gravity anomaly in the north. The main radiometric anomaly has the same trend and location as the Chamata river system (Fig. 6.9).

There is generally good agreement of the gravity and magnetic trends with most of the geochemistry results (Figs. 1.17 – 1.22). Though the high metal concentrations plot north of the magnetic anomaly, they generally lie over the gravity anomaly. Particularly good correlations are found with the cadmium and copper concentrations with notable deviations being the nickel and lead contours. The aeromagnetic maps (Figs. 1.23 and 1.24) reveal that the magnetic high is actually an elongate feature extending further south of the grid with a total length of about 8,8 km with a trend shown in the grid.

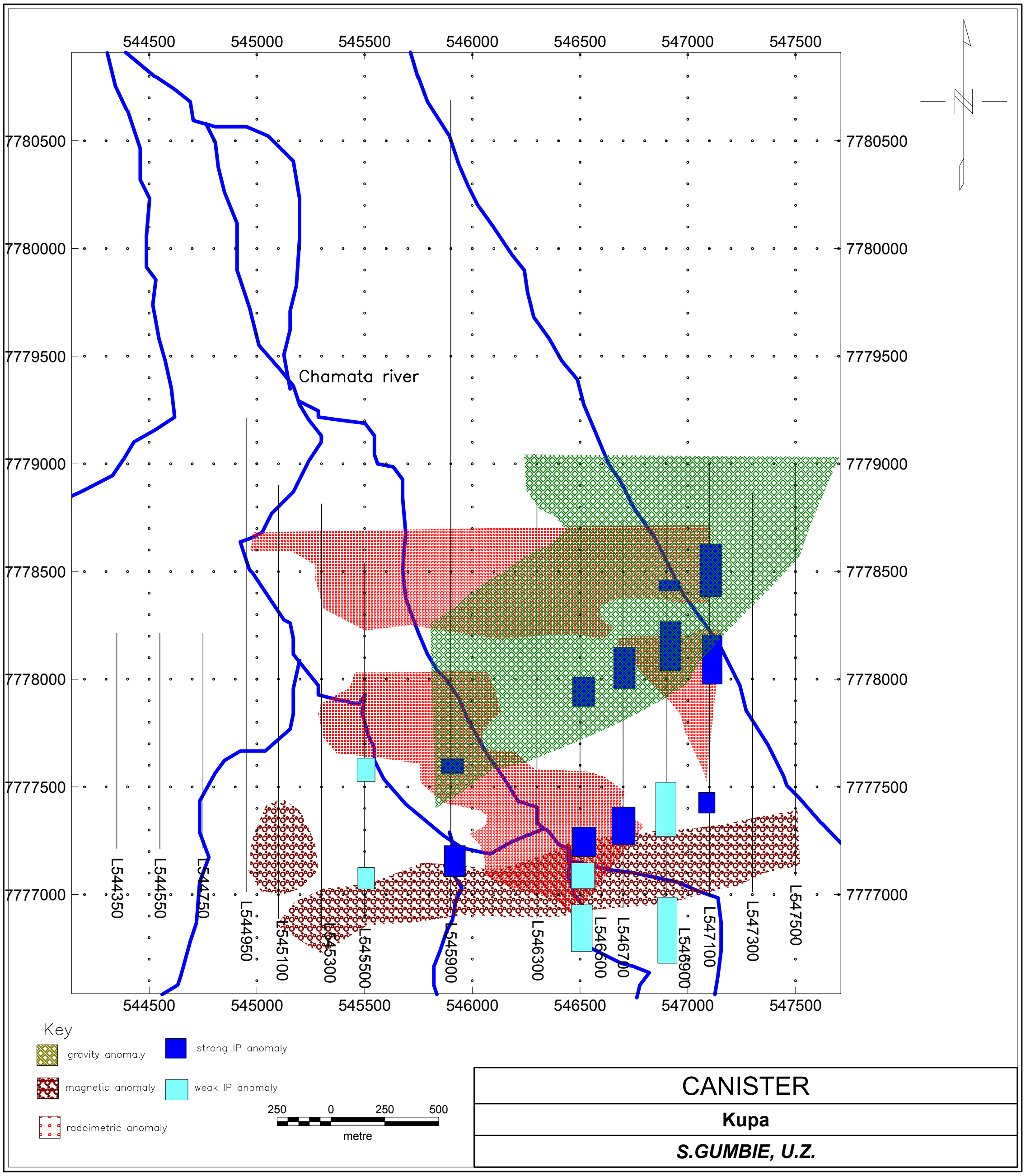

Fig. 6.8 Anomaly correlation map showing the adjacent, sub-parallel gravity and magnetic anomalies, TC anomalies, strong and weak IP anomalies. The Chamata river system is also shown and is coincident with the clay soils of the southern portions of the grid.

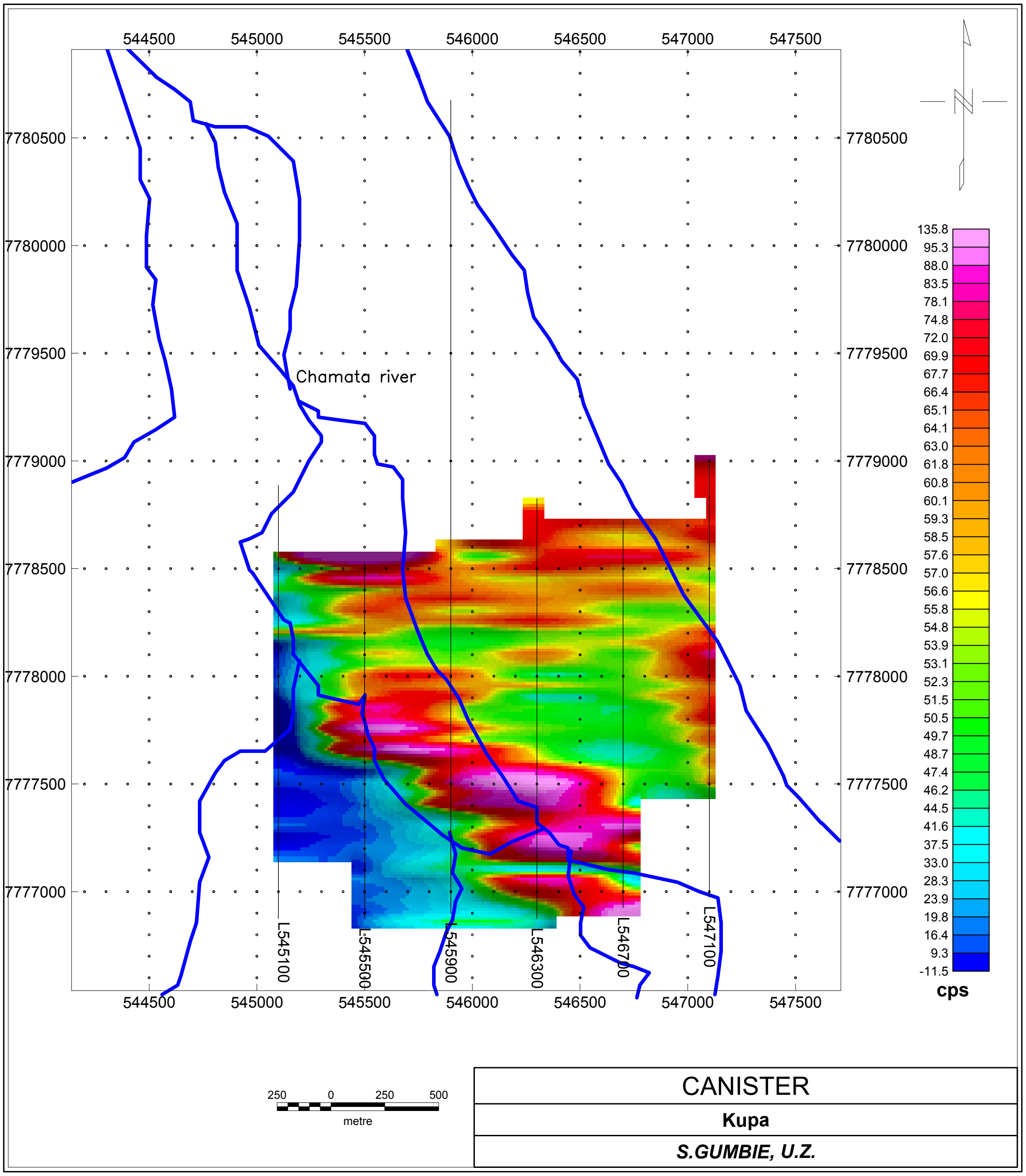

Fig. 6.9 River drainage and radiometric TC anomaly correlation map showing spatial relationship between total counts and river courses on the Chamata system.

6.7 Conclusions

The geophysical techniques employed were successful in the detection and definition of an anomalous body below the Kalahari sand cover. Ground magnetics reveals an ENE – WSW trending high magnetic feature in the southern edge of the map with sub-parallel but weaker highs at 500 m and 2,4 km to the north. These are relatively shallow bodies, with a 24 m and 90 m depth estimate. A deeper source depth of 247 m is also calculated but it is unlikely to be as significant as the shallower estimates due to the rapid fall-off of the magnetic field strength. The gravity method detected a gravity high, at least 600 m wide running NE – SW adjacent to the magnetic feature. This demonstrated that the causative body of the magnetic anomaly was not the dense structure of the gravity anomaly. A graphical estimate of the parameters from the gravity anomaly of the long line (Kup13) to define the regional gave a depth to top of 246 m with a dip of 84º N. The radiometric method was able to map radioactive isotope concentrations in the clays along the river system which had a general NW – SE trend and, presumably, shallow buried granites in the north with a general E – W trend. The IP anomalies showed a paired occurrence in the grid with a 400 m – 700 m separation which seemed to outline the inferred greenstone as having margins that are highly chargeable and of low resistivity. It is possible that these could be sulphide bodies in a layered steeply dipping volcano-sedimentary sequence.

This anomaly pattern, interpreted in conjunction with the geochemistry, supports the VMS model suggested by Canister geologists. The prominent magnetic anomaly is a BIF with the weaker sub-parallel anomalies being the signatures of the distinctly zoned metal sulphides embedded in a meta-sedimentary and volcanic suite of the greenstone belt. This is also corroborated by the regional geology discussed in section 1.2.1 where BIFs are reported to be widespread.

The main anomaly was especially clear with the ground magnetic method which provided a quick and reasonably cheap technique for probing beneath the sands. The further data processing techniques provided powerful methods for ease of interpretation. Comparison of Fig. 6.4 with Fig. 1.25 illustrates that the ground magnetic method has a greater resolution than the aeromagnetic method; therefore this survey added more value to the magnetic database. Radiometric surveying remains a cheap and useful method especially where granite plutons exist at shallow depths below overburden. However, this was not ascertained by this study. Interpretation of the IP results remained considerably qualitative but comparison with case studies of other metal sulphide discoveries using IP should be useful in locating such deposits. The ultimate test for the accuracy of the geophysics is drilling.

6.8 Recommendations

The anomaly at the extreme southern part of the grid may continue southwards and along its trend. It is recommended that all the geophysical techniques used in this study be repeated on a larger grid, extending at least another 1 km to the south of the current start of the lines and more lines to be put on the eastern side of the grid. It was also noted by the author that a shear zone lies in the granites near the SE corner of the grid (Figs. 1.12 and 1.16) and it would be advisable to include it in the survey area. The radiometric method could prove particularly useful here in delineating the shear zone and other bodies (e.g. pegmatites) with a potentially high radioactive signature. A dipole-dipole IP survey is recommended to produce symmetrical anomalies for better correlation with geology and the other methods. Reconsidering a turam survey would provide a test for another geophysical technique for resolving the subsurface geology, both spatially and with depth. The local geology map could be improved by using the results of these geophysical surveys.

Finally, a drilling pattern is recommended to probe the east – west trends, starting from the magnetic anomaly in the south in a grid pattern that spans both north and south of the anomaly in order to investigate both for any sulphide bodies and any mineralization in the shear zone.

REFERENCES

Amm, F.L., 1940. The Geology of the Country around Bulawayo. Southern Rhodesia Geological Survey Bulletin No. 35, reprinted 1965. 270 pp.

Blakely, R.J., 1996. Potential Theory in Gravity and Magnetic Applications. Cambridge University Press. 441 pp.

Breiner, S., 1973. Applications Manual for Portable Magnetometers. Geometrics, California, U.S.A. 58 pp.

Collinson, D.W., 1983. Methods in Rock Magnetism and Palaeomagnetism: Techniques and Instrumentation. Chapman and Hall. 503 pp.

Dobrin, M.B. and Savit, C.H., 1988. Geophysical Prospecting. Fourth Edition. McGraw-Hill International Edition. 867 pp.

Edwards, L.S., 1977. A Modified Pseudosection for Resistivity and Induced Polarization. *Geophysics*, **42**, pp. 1020 – 1036.

Grant, F.S. and West, G.F., 1965. Interpretation Theory in Applied Geophysics. McGraw–Hill. 584 pp.

Groves, D.I. (ed.), 1999. M.Sc. Key Short Courses in Exploration Geology. University of Zimbabwe.

Harpum, J.R., 1963. Petrographic classification of granite rocks in Tanganyika by partial chemical analyses. *Rec. geol. Surv. Tanganyika*, **10**.

Jacobs, J.A., 1987. The Earth's Core. Second Edition. Academic Press. 416 pp.

Kearey, P. and Brooks, M., 1988. An Introduction to Geophysical Exploration. English Language Book Society/Blackwell Scientific Publications. 296 pp.

Litherland, M., 1975. The Geology of the area around Maitengwe, Sebina and Tshesebe, Northeast and Central Districts, Botswana. District Memoir 2, Geological Survey Department, Republic of Botswana. 133 pp.

Lowrie, W., 1997. Fundamentals of Geophysics. Cambridge University Press.354 pp.

Merrill, R.T. and McElhinny, M.W., 1983. The Earth's Magnetic Field. Its History, Origin and Planetary Perspective. Academic Press. 401 pp.

Milsom, J., 1989. Field Geophysics–Geological Society of London Handbook. Open University Press. 182 pp

Morse, J.G. (ed.), 1977. Nuclear Methods in Mineral Exploration and Production. Elsevier Scientific Publishing Company. 280 pp.

Mukodzani, B., 2001. Geophysical Surveys over a Potential Gold Deposit, West of Kadoma, Zimbabwe. M.Sc. Thesis, University of Zimbabwe. 146 pp.

Nettleton, L.L., 1976. Gravity and Magnetics in Oil Prospecting. McGraw-Hill International Series in Earth and Planetary Sciences. 464 pp.

Parasnis, D.S., 1986. Principles of Applied Geophysics, Fourth Edition. Chapman and Hall. 402 pp.

Parker E.N., 1955. Hydromagnetic dynamo models. *Astrophys. J.* **122**.

Parkinson, W.D., 1983. Introduction to Geomagnetism. Scottish Academic Press. 433 pp.

Peddie, N.W., 1982. International Geomagnetic Reference Field: The Third Generation. *Journal of Geomagnetism and Geoelectricity*. **34**, pp. 309 - 326.

Podmore, F., 1985. A Gravity Study of the Great Dyke, Zimbabwe. Ph.D. Thesis, University of London. 439 pp.

Reynolds, J.M., 1997. An Introduction to Applied and Environmental Geophysics. John Wiley & Sons. 796 pp.

Robinson, E.S. and Coruh, C., 1988. Basic Exploration Geophysics. John Wiley & Sons. 562 pp.

Sayce, K. (ed.), 1987. Tabex Encyclopedia Zimbabwe. Quest Publishing (Pvt.) Ltd. 431 pp.

Spector, A. and Parker, W., 1979. Computer Compilation and Interpretation of Geophysical Data. In: **Hood, P.J. (ed.)**, Geophysics and Geochemistry in the Search for Metallic Ores. Geological Survey of Canada, Economic Geology Report **31**, pp. 527 - 544.

Sumner, J.S., 1976. Principles of Induced Polarization for Geophysical Exploration. Elsevier Scientific Publishing Company. 277 pp.

Telford, W.M., Geldart, L.P. and Sheriff, R.E., 1990. Applied Geophysics, Second Edition. Cambridge University Press. 770 pp.

Tennent, R.M., 1979. Science Data Book. Oliver and Boyd. 105 pp.